REPORT DOCUMENTATION PAGE

AFRL-SR-BL-TR-00-

0818

1. AGENCY USE ONLY *(Leave blank)*	2. REPORT DATE	3. REPORT TYPE AND DATES COVERED
	12 Dec 00	Final Report: 01 Jun 97 TO 31 May 00

4. TITLE AND SUBTITLE

Micromechanism Based Modeling Of Metal Matrix Composites

5. FUNDING NUMBERS

F49620-97-1-0338

6. AUTHOR(S)

Dr. David H. Allen

7. PERFORMING ORGANIZATION NAME(S) AND ADDRESS(ES)

Texas A&M University
Aerospace Engineering Department
3141 TAMU
College Station, TX 77843

8. PERFORMING ORGANIZATION REPORT NUMBER

9. SPONSORING/MONITORING AGENCY NAME(S) AND ADDRESS(ES)

AFOSR
801 N. Randolph St.
Arlington VA 22203

10. SPONSORING/MONITORING AGENCY REPORT NUMBER

11. SUPPLEMENTARY NOTES

12a. DISTRIBUTION AVAILABILITY STATEMENT

Approved for public release: Distribution is unlimited

12b. DISTRIBUTION CODE

13. ABSTRACT *(Maximum 200 words)*

The purpose of this study is to experimentally quantify the multi-dimensional growth characteristics of the oxide scale formed on commercially pure titanium at 700°C in a flowing air environment. The geometries considered herein had characteristic dimensions that were appropriately sized to match the thickness of the oxide scale and were fabricated into shapes of solid and hollow cylinders and external and internal wedges. Scanning electron microscopy (SEM) image analysis was used to measure the oxide layer thickness and the Pilling-Bedworth ratio (PBR) as a function of time. An effective diffusion coefficient was determined from one-dimensional planar oxide thickness data and experimentally obtained PBR values served as the necessary input to a solid state diffusion model, which was modified to account for the volumetric expansion of the oxide.

14. SUBJECT TERMS

Micromechanism Based Modeling Of Metal Matrix Composites

15. NUMBER OF PAGES

16. PRICE CODE

17. SECURITY CLASSIFICATION OF REPORT	18. SECURITY CLASSIFICATION OF THIS PAGE	19. SECURITY CLASSIFICATION OF ABSTRACT	20. LIMITATION OF ABSTRACT
UNCLASSIFIED	UNCLASSIFIED	UNCLASSIFIED	UL

Submitted to: *Oxidation of Metals*
December 23, 1999
M.S. 1360, Resubmitted September 23, 2000
D.L Douglass
Arizonal Materials laboratories
Univ. Arizona, Tucson, AZ 85712
modified 9/23/2000

The Morphological Evolution of TiO_2 Scale Formed on Various 1-D and 2-D Geometries of Titanium

P.K. Imbrie and D.C. Lagoudas

Center for Mechanics of Composites
Department of Aerospace Engineering
Texas A&M University
College Station, TX 77843-3141

Abstract

The purpose of this study is to experimentally quantify the multi-dimensional growth characteristics of the oxide scale formed on commercially pure titanium at 700°C in a flowing air environment. The geometries considered herein had characteristic dimensions that were appropriately sized to match the thickness of the oxide scale and were fabricated into shapes of solid and hollow cylinders and external and internal wedges. Scanning electron microscopy (SEM) image analysis was used to measure the oxide layer thickness and the Pilling-Bedworth ratio (PBR) as a function of time. An effective diffusion coefficient was determined from one-dimensional planar oxide thickness data and experimentally obtained PBR values served as the necessary input to a solid state diffusion model, which was modified to account for the volumetric expansion of the oxide.

The model results demonstrate the competing influences of oxide expansion and curvature effects. In addition, the predictive capability of the model, for the case of a solid cylinder, was shown to under predict experimental results, whereas, scale growth on the inner surface of a hollow cylinder was over predicted. The differences are primarily attributed to an effective diffusion coefficient that varies the scale morphology. An oxide

layer grown on an outside surface of a solid cylinder or an external wedge was found to have a structure similar to one-dimensional planar oxide growth. On the contrary, scale developed on the inside surface of a hollow cylinder or an internal wedge was observed to be more compact.

Keywords: Image Analysis; Scanning Electron Microscopy (SEM); Titanium; Oxidation; Diffusion

1. Introduction

There continues to be widespread use of titanium and its alloys in the aerospace, petrochemical, gas/steam turbine, and automotive industries for a variety of structural applications. These materials are considered technically superior and cost-effective primarily because of their high strength-to-weight ratio, strength at moderate temperatures, and good resistance to creep and fatigue[1]. However, while they have excellent corrosion properties in gaseous oxygen and air at temperatures up to 600°C, at higher temperatures they exhibit poor long-term oxidation resistance due to scale formation and oxygen embrittlement. Since these materials are used to fabricate engineered components that generally involve some complex shape, understanding how oxidation will effect their useful life is important. Unfortunately, research to date has primarily been focused on one-dimensional planar oxidation behavior and its direct applicability to multidimensional case has not been considered.

In order to understand the general behavior of titanium oxidation, conclusions regarding its one-dimensional planar characteristics can be made from some of the

pioneering work of Gulbransen and Andrew[2], Davies and Birchnall[3], Morton and Baldwin[4], Jenkins[5-7], Kofstad, *et al.*[8-10], and Stringer[11,12], to name just a few. One primary observation by all these authors is the complex nature of oxidation kinetics in titanium. Kofstad, *et al.*[10] asserted that from a thermodynamic standpoint one could reason the formation of various oxides including: TiO; TiO_2; Ti_2O_3; and Ti_3O_5. However, he concluded only the rutile modification of TiO_2 has generally been observed for oxidation in oxygen below 1000°C.

Because the oxidation mechanisms of titanium change both with time and temperature, different reaction rates, and corresponding rate equations, are needed to describe its oxidation behavior[8]. Oxidation of titanium between 600°C and 1000°C, is typically initially described by a parabolic rate law. This parabolic time dependence represents two distinct processes: oxygen dissolution and oxide scale formation. The rate law is valid throughout the entire temperature range even though titanium undergoes an allotropic transformation from *h.c.p.* (α-Ti) to *b.c.c.* (β-Ti) at 882°C. Kofstad, *et al.*[8] suggests that the phase change has little effect on the oxidation mechanisms, except during the initial stages of the oxidation reaction.

The early stages of oxidation of titanium have been investigated by Vaquilla *et al.*[29] and Mizuno *et al.*[30], while the specific oxidation mechanisms for long-term parabolic oxidation have been extensively studied by a number of investigators[5,6,8-14,28]. There is general agreement that the process is dominated by the diffusion of oxygen in both the scale and the metal core and that scale growth is dependent upon the oxygen concentration gradient in the metal[5]. During the initial stage of oxidation, oxygen is absorbed on the surface of the metal by physisorption. The oxygen molecules dissociate

creating oxygen anions through a chemisorption process until a monolayer of oxide is formed[8]. Depending upon the oxygen concentration gradient in the metal, oxygen ions either pass through the thin film and are dissolved into the hexagonal titanium lattice at octahedral interstitial locations or produce fresh oxide. Continued growth of the oxide film is restricted by the need for the chemical potential of oxygen in the oxide film and the reacting titanium to be in equilibrium. If a non-equilibrium condition exists, the rate of oxygen dissolution becomes the prevailing mechanism. However, once the titanium at the metal/oxide interface becomes saturated with oxygen, the rate determining reaction is diffusion of oxygen ions through the oxide scale[5,6]. The TiO_2 scale has been characterized as an n-type semiconductor having an oxygen deficient structure that produces oxygen ion vacancies rather than interstitial titanium ions. Thus, there is an inward passage of oxygen produced by anion-vacancy diffusion through the rutile lattice[3,5-10,15]. It has also been shown that the activation energy for titanium ion diffusion is much greater than that of oxygen ion diffusion in TiO_2[5,8]. Therefore, for temperatures below 1000°C, it is generally believed that diffusion of titanium ions outward through the oxide layer is negligible. This was substantiated by Déchamps *et al.*[13] when they performed a study on the various diffusion mechanisms associated with titanium oxidation and concluded that solid state diffusion of titanium would be difficult because the monocrystalline rutile contains micropores, grain boundaries, and is stratified, all of which act as solid state diffusion barriers.

While a parabolic rate law describes the initial oxidation kinetics of titanium for this temperature range, the period for which it is valid is governed by the formation and growth of an initial coherent scale layer that grows to a critical thickness[6]. Once the

critical thickness is obtained, stresses in the scale and the metal at the metal-oxide interface become large enough to cause it to fail, resulting in the growth of fresh oxide. The critical thickness is associated with a steady-state oxygen concentration profile in the outer surface of the metal at the metal-oxide interface. At this point, there is a change from parabolic to linear oxidation. The transition to linear oxidation has been correlated to the oxygen concentration in the metal lattice at the interface. Andersson, *et al.*[16] showed oxygen concentrations reaching a value that corresponds to a composition of $TiO_{0.35}$ leads to structural changes in the solid solution. The expansion of the lattice leads to large compressive stresses that result in the detachment of a layer of $TiO_{0.35}$ followed by rapid oxidation of that layer[7,9,16]. Thus, heavy oxide formation begins to take place and the oxidation follows a linear rate[7,9]. While some researchers have observed a linear oxidation rate following an initial parabolic period, Lopes-Gomes and Huntz[15] and Bertrand[17] have reported that the linear behavior is really a series of successive parabolic steps. During each parabolic step, a new sub-layer is formed by the same mechanisms as described above.

A number of researchers, such as Jenkins[5], Kofstad, *et al.*[9], Stringer[11], Lopes-Gomes and Huntz[15] and Bertrand[17], have reported the TiO_2 oxide scale has a morphology that consists of two observable phases. The first phase is a comparatively compact zone that extends inward from the gas-oxide interface to a second phase of oxide that has a porous-laminar structure and extends to the metal-oxide interface. The various strata in the second phase vary in thickness, as well as number, depending upon the time and temperature of the exposed surface. Bertrand[17] observed a third oxide zone that was referred to as a non-stratified course grained crystallized structure appearing between the

second phase and the metal-oxide interface. In addition, Lopes-Gomes and Huntz[15] reported the individual layers were separated by cracks that extended over short distances which became visible only after the cooling of the specimen.

The aforementioned discussion summarizes observations regarding the characterization of one-dimensional planar titanium oxidation behavior. However, there are many engineering applications where understanding multi-dimensional oxidation behavior is important, such as at a crack tip or along a delaminating titanium-based metal matrix composite[18-20], and the direct applicability of one-dimensional planar observations to the multidimensional case have not been established. Therefore, the purpose of this investigation is to experimentally quantify the multi-dimensional growth characteristics of titanium oxide scale. Since adding alloying elements to titanium can affect its oxidation behavior in a variety of different ways[6], the case involving the simplest form will be considered herein using commercially pure titanium. The experiments will be conducted at 700°C in a flowing air environment for oxidation times up to 240 hours. While typical engineering applications of titanium find use at temperatures between 500 and 600°C, 700°C is chosen because the same parabolic oxidation mechanisms can still be observed and the time to grow a sufficiently thick oxide layer is significantly shorter. In addition, most of the literature on titanium oxidation is limited to relatively short oxidation periods, i.e. hours or tens of hours. Therefore, a long-term exposure is desired in order to investigate the effects on the oxide morphology.

The geometries considered herein-included solid and hollow cylinders, as well as external and internal wedges and were chosen due to their importance in representing a wide range of useful shapes, especially in metal matrix composites. The measured

quantities were weight gain and oxide layer thickness for a specified exposure. In addition, optical microscopy and scanning electron microscopy (SEM) are used to evaluate the morphological evolution of the oxide scale. In addition, 1D oxidation data are obtained in order to compute constants for a multi-dimensional solid state diffusion model that is based upon Fick's 1st Law which has been modified by Entchev, *et al.*[21] to account for the volumetric expansion of the oxide scale. The constants, along with the results of the multi-dimensional experiments, are then used to verify the predictive capabilities of the model.

In the sections that follow, the experimental procedures used in this investigation are described. This is followed by a discussion of the experimental results, which includes both an evaluation of the measured data, as well as observations regarding the scale morphology for the various multi-dimensional geometries. Finally, a brief overview the oxidation model is presented along with the methods used to evaluate the necessary input data. Model results are then compared to experimental data for the oxidation of an internal wedge.

2. Experimental Procedures

2.1 Material.

The materials selected for this research were obtained in sheet and wire forms. The sheet stock was commercially pure (CP), ASTM grade 1, unalloyed titanium manufactured by Timet, Inc., Morgantown, PA, under the product name of Timetal® 35A. The material was produced from titanium sponge using an Electron Beam (EB) cold hearth furnace process where the resulting remelt electrodes were formed into ingots

by a Vacuum Arc Reduction furnace (VAR). The VAR ingots were then forged into slabs and subsequently milled, through a series of hot and cold rolling stages, to final average thickness of 0.65 mm. The nominal chemical analysis of the Timetal® 35A material, in maximum allowable weight percent, was 0.006 N, 0.005 C, 0.030 Fe, and 0.040 O with the balance being Ti.

The wire stock was unalloyed titanium manufactured by Goodfellow Corp, Berwyn, PA, to a specified purity and diameter. The wire was fabricated using a cold draw process which eventually reduce the ingot material to nominal diameters of 0.25 mm, 0.125 mm, and 0.05 mm, with each wire diameter having a titanium purity of 99.6%, 99.6% and 99.8%, respectively. No energy dispersive X-ray spectroscopy (EDS) or electron microprobe (EM) characterization studies were performed on the as-received material in order to quantify the level of impurities. However, a typical chemical analysis suggested by the manufacturer, in weight percent, was 0.0005 Cu, 0.002 Ca, 0.005 Cr, 0.005 Ni, 0.006 H, 0.01 Mn, 0.015 N, 0.02 Sn, 0.03 Al, 0.03 C, 0.03 Si, 0.15 Fe, and 0.2 O with remainder being Ti for the material considered 99.6% pure. Similarly, the chemical composition for the 99.8% pure titanium was typically suggested to be 0.0001 Al, 0.001 Cu, 0.001 Mg, 0.002 Ni, 0.003 Cr, 0.003 Si, 0.005 Ni, 0.005 V, 0.008 H, 0.009 Fe, 0.04 Mn, and 0.04 O with the remainder being Ti.

2.2 *Specimen fabrication and preparation.*

The specimen geometries used for this investigation included: 1)flat specimens; 2)solid and hollow cylinder specimens; and 3)internal and external wedge specimens as shown schematically in Fig. 1. The specimens were fabricated from either sheet or wire

stock material and are shown in their finished state via SEM images in Fig. 2. The nominal target dimensions for the various specimen configurations depicted in Fig 1 and 2, are shown in Table 1. This table provides details as to the approximate size and shape of the various specimens. However, it should be noted that nominal dimensions provided for comparison purposes only. Where appropriate, the actual measurements for each individual specimen were used for subsequent data analysis.

All samples made from sheet stock were fabricated from the same stock of bulk material. Individual samples were sectioned to their respective length and width with a diamond cutoff saw. A hole was mechanically drilled through the thickness at one end of each sample in order to suspend the specimen during testing. In order to eliminate variances in the specimen-to-specimen initial surface texture, the specimens were wet ground to a uniform surface finish using silicon carbide paper through 2000 ANSI grit. All samples prepared from wire stock were simply cut to length and oxidized with the "as-received" surface finish.

Additional machining operations were used to fabricate the specific cylindrical and wedge specimen geometries shown in Fig. 1 and 2. These included: 1) mechanically drilling the holes to produce the hollow cylinder samples; 2) milling the included angle on the edge of the outside wedge specimens; and 3) broaching the V groove into the surface of the inside wedge samples. No subsequent grinding procedure was preformed to refine the "as-machined" surface finish.

After fabrication, the samples were first cleaned in acetone, then chemically etched in a solution of 4.2% HF + 12.5% HNO_3 + 83.3% H_2O for 60 seconds, and then rinsed in isopropyl alcohol in order to remove any residual enchant. The specimens were

then annealed for 24 hours at 800°C in a vacuum better than 5 x 10^{-6} torr. This was done to obtain a reference microstructure, as well as ensure that the grain size would not change during the oxidation. However, during the annealing step, the 0.05mm diameter solid cylinder samples became to brittle to handle, and were tested using the "as received" microstructure. In addition, the 30° internal wedge samples became blunted during the heat treatment. The blunting of the wedge tip is assumed to be the result of stress-relief from stresses developed during the fabrication process. Since no other micro-machining methods were available, the 30° internal wedge geometry was abandon. The remaining vacuum annealed samples were then acid-cleaned in the solution described above for 10 seconds, ultrasonically rinsed in isopropyl alcohol, and then stored in isopropyl alcohol for subsequent measurement and testing.

The type of initial measurements made on each specimen were a function of the intended experiment. For the weight gain study, the dimensions of the finished samples were measured to the nearest 0.00025 cm and had a repeatability standard deviation of 0.0064. In addition, each sample was initially weighed in air, as well as in H_2O on a Mettler AB 204 analytical balance. The balance had an absolute accuracy of ±1 mg with a repeatability of ±0.1 mg. Individual weight measurements were performed on each sample, since a thermogravimetric analysis unit (TGA) was not used.

Samples used to obtain oxide layer behavior as a function of time, were quantified by obtaining a reference configuration via scanning electron microscopy (SEM). The length scales of the unoxidized specimens were established by using micro laytex spheres (1.072 μm or 10.568 μm diameter) on the surface of each specimen.

2.3 *Oxidation Experiments.*

Oxidation tests were performed in a Ney 2-160 muffle-type furnace that had a heated volume of 1845 cm^3. The experiments were conducted at 700°C (±1°C) in dry flowing laboratory air (7 l/m) for various oxidation times up to 240 hours as shown in Table 2. Initially, the flat specimens and the solid cylinders were subjected to a long-term oxidation exposure. However, since micrographs of these specimens did not reveal any significant morphological differences from the 72 hour oxide scale, the remaining experiments were only carried out to only 72 hours with an additional test point of 36 hours being added. Table 2 also indicates the number of specimens that were used as part of this test program. While only one specimen was oxidized for each of the 2D geometries, three different planar oxide thickness measurements were made in order to obtain an average value. Similarly, a total of 4 weight gain measurements were used to obtain an average value for the weight gain analysis.

The specimens were suspended in the center of the furnace chamber by Inconel® rods as shown in Fig. 3. The procedure for initiating the oxidation experiments was to first allow the furnace to reach a steady value at the test temperature for 12 hours. Then the furnace door was opened and the suspension rods (with the samples) were placed on their supports. No attempt was made to take into account the specimen temperature rise time other than to note that the furnace temperature recovered to 99% of its set point value in 45 seconds and was fully recovered in 300 seconds. At the designated exposure times, individual specimens were extracted from the furnace and stored in a vacuum for later processing.

2.4 *Oxide Growth Characterization.*

Oxidized specimens were evaluated by oxide thickness measurements and/or weight gain analysis as a function of time. For the weight gain analysis, both the change in mass and the reference surface area of each specimen were the measured quantities. The pre and post-test mass of a specimen were measured on the same analytical balance. Since an orthogonal specimen configuration was not guaranteed during fabrication, the reference surface area was estimated in the following manner. First, the density of the sample was determined by applying Archimedes Principal to the measured weight of a specimen that was obtained from an analytical balance in both air and distilled water. Then, the volume of the specimen was computed given its known density (ρ) and mass (m). Next, the surface area perpendicular to the thickness, S_A, (see Fig. 1) was obtained, assuming the specimen had a constant thickness (z) and using the relation $S_A = V / z$. Finally, the reference surface area, A, was computed by

$$A = 2(S_A) + (P + 2\pi r) \cdot z, \tag{1}$$

where P is the perimeter length around S_A and r is the radius of the specimen suspension hole.

The characterization of the titanium and oxide microstructure, as well as inspection of the scale morphology was performed by examining various cross-sectioned specimen configurations (after mounting) before and after oxidation using SEM. The samples were prepared for SEM evaluation by potting them in a cold mount thermal-set epoxy resin and then grinding and polishing them on a Struers Rotopol automated polishing system. Each sample was first wet-ground to a uniform surface finish using silicon carbide paper through 2000 ANSI grit and then polished. The polishing steps

included using a 3 μm diamond suspension on a satin woven acetate cloth for 3 minutes. This was followed by using a colloidal silica solution (45% colloidal Si + 45% H_20 + 9% H_2O_3 + 0.5% HNO_3 + 0.5% HF) on a medium hard neoprene cloth for 5 minutes.

Precise oxide thickness measurements were performed by establishing an accurate length scale using micro laytex spheres (1.072 μm or 10.568 μm diameter) on the surface of each epoxy mount. Oxide growth evolution was evaluated by comparing the before and after oxidation configurations of each specimen.

3. Experimental Results

3.1 Scale Morphology for Different Geometries.

3.1.1 Flat Specimens

The morphological evolution of the TiO_2 scale formed at 700°C was observed via optical microscopy, as well as SEM. A visual inspection (using a 5x optical microscope) of the exterior features of the oxide revealed that initially a thin slate-gray colored scale was formed on the titanium substrate. As time proceeded, its color changed from slate-gray to off-white pale yellow and finally to a light brown after 240 hours of exposure. The surface texture of the scale was, at first, smooth and one could easily discern preferential oxide growth corresponding to the pre-oxidized surface grain structure. However, as the oxide layer grew in thickness, it became noticeably more rough and its grain-like appearance diminished with time. After approximately 36 hours of exposure, surface cracks were observed forming along the edges of the specimen. These surface cracks grew with time and eventually opened wide enough to reveal other large fissures

within the multi-layered scale, as well as regions of oxide spalling at or near the corners of the specimen.

Figure 4 provides insight as to the one-dimensional planar development of the oxide scale as a function of time. After 10 hours of exposure, it can be seen that the oxide scale appears to be coherent and free of any observable defects, which is consistent with observations made by Jenkins[6]. However, as the exposure time increases, three different oxide structures can be observed (see Fig 4 after 20 hours of oxidation). The scale adjacent the air-oxide interface appears to be compact, while the interior scale has numerous voids and the scale at or near the metal-oxide interface is void-free but more granular than the scale at the air-oxide interface. It is presumed that the compact scale observed at the air-oxide interface after 20 hours has be displaced from the metal-oxide interface because of new oxide formation. As the oxidation process continues, the new-growth oxide is subjected to various stresses that in turn cause it to fail, creating a porous structure. Stringer[11] attributes void formation to the creation of scale blisters, which result in localized buckling of the oxide layer. Whereas Lopes-Gomes and Huntz[15] indicate that the voids are formed when stresses arising between the expanded α-solid solution and the more voluminous oxide induce partial cracking between the metal and the oxide scale at the metal-oxide interface. The voids, which are first observed after approximately 20 to 24 hours of oxidation, appear to have a long needle-like geometry with the axis of the needle running perpendicular to the metal-oxide interface. However, as the oxide scale grows, the same voids move away from the metal-oxide interface and gradually take on a larger more ellipsoidal shape after 48 hours. This suggests either the oxide is expanding, the stress state in the scale is changing, or some combination of both.

While no attempt was made to quantify the distribution of void sizes, there is a general trend for the voids to be smallest near the metal-oxide interface and grow in size as one moves away from the metal surface.

The micorgraphs in Fig. 4 also reveal that the interior scale has a layered-like structure with the layers growing parallel to the metal-oxide interface, as mentioned in the introduction. While it is believed that the layers exist for exposures as short as 20 hours, more direct evidence of their presence can be observed in the micrographs after 72 hours of oxidation. Stringer[11] reported that the interior layers of scale are actually porous to gaseous oxygen, which would imply the voids observed herein might be interconnected. However, the permeability of the oxide formed during these experiments to gaseous oxygen was not investigated. In addition, if each layer is accompanied by the formation of new voids, one would expect there to be uniformly distributed throughout the total scale thickness. However, this was not observed in these experiments. Instead, there appeared to be a greater concentration of voids away from the metal-oxide interface. This would suggest that the increased thickness of the scale reduced the propensity for a newly forming layer to buckle.

In addition to void development, cracks were also observed. In most cases, cracks were observed to develop at the interface between the porous layers. Once initiated, they would either continue growing in a direction parallel to the metal-oxide interface or they would change direction and propagate to the surface. The cracking phenomenon is consistent with observations by other investigators who have performed acoustic transmission studies during oxidation[22].

The aforementioned observations regarding the scale morphology suggest that diffusion of oxygen through the oxide scale cannot be adequately described by a single mechanism. As was previously stated, it is believed that during the formation of the compact scale, anion-vacancy diffusion is the oxygen transport mechanism. However, once the oxide begins to crack and/or localized blistering occurs, gaseous oxygen is then allowed to rapidly penetrate down to the reaction surface. The diffusion mechanism returns to ionic transport once a new compact oxide film/layer is formed and the process repeats itself.

3.2 2D Geometries.

Four different geometries were tested in order to investigate the formation of oxide scale on curved surfaces, as well as on intersecting planar surfaces. The geometries included hollow cylinders, solid cylinders, internal wedges, and external wedges. The sections that follow describe the morphological similarities and differences observed between the various geometries.

3.2.2 Hollow Cylinders.

The formation of oxide scale on the hollow cylinders showed no unique differences between the three initial diameters tested. Therefore, Fig. 5 serves as a representative example of the development of the oxide layer as a function of exposure time. The scale has several notable differences from the oxide scale formed on a flat specimen for the same oxidation time and temperature (for example see Fig. 4). These differences include: 1) there did not appear to be a tendency for the scale to detach from

the metal, regardless of the oxidation time; 2) the surface texture of the scale was smooth; and 3) there did not appear to be a substantive amount of void initiation and subsequent void expansion as was observed in the flat specimens. It is believed the lower level of void formation in the hollow cylinder specimen geometry is due to the stress-state in the oxide. The curved geometry most likely produces larger compressive stresses in the oxide scale, which in turn produces higher tensile hoop stresses in the metal. The larger hoop stresses in the metal then offset the compressive stresses being developed as a result of the dissolution of oxygen into the metal lattice.. Since deformation of the metal lattice eventually causes the oxide at the metal-oxide interface to fracture, any reduction in the local stress would reduce the number of cracks formed that serve as void initiation points. In addition, it is believed that the curvature of the hollow cylinder results in a higher buckling resistance for the TiO_2 scale, which reduces the blistering phenomena observed by others[11,15]. Lastly, while not easily seen in Fig. 5, a close inspection of scale reveals that it is composed of several layers that develop radially inward from the air-oxide interface.

3.2.2 Solid Cylinders.

Scale formation on the solid cylinders was similar to that developed on the flat specimens. For short oxidation times, the oxide scale appears to be compact, as well as firmly attached to the metal substrate, regardless of the amount of surface curvature. However, as the oxidation time increases, the compact layer moves away from the metal-oxide interface and is replaced by a porous-layered oxide structure (see Fig. 6).

Figure 6 also shows, for the cylinder diameters tested, there is a tendency for radial cracks to develop. However, it is not known whether these cracks are actually formed during the oxidation exposure or are a cool-down artifact resulting from a mismatch between the coefficients of thermal expansion of the two materials ($\alpha_{Ti} = 9.2 \times 10^{-6} / ^{\circ} C^{23}$ and $\alpha_{TiO_2} = 8.0 \times 10^{-6} / ^{\circ} C^{23}$). In addition, there appears to be very few cracks, if any, forming circumferentially around the specimen. This is inconsistent with crack development in the flat specimen oxide, where fracture parallel to the metal-oxide interface was generally observed. The circumferential cracks shown in Fig. 6 most likely formed during cool down, since no fresh oxide appears to have formed on the metal-oxide interface.

The micorgraphs shown in Fig. 6 also reveal a changing surface texture with exposure time and surface curvature. The scale appears to be relatively smooth for short oxidation exposures and becomes rougher with time, as well as cylinder radius. However, it is believed that the changing scale roughness is not necessarily a function of the geometry, but rather is simply an artifact of the initial surface roughness of the specimen.

The oxide scale was observed to be similar to that developed on the flat specimens, that is, the outer scale appears to by compact, while the interior scale has a porous layered-like structure. In addition, as new layers of the oxide form, the initial pores become more evident, suggesting that the preceding layers continue to expand. This expansion is accompanied by a corresponding expansion of the individual pores previously created. Therefore, it is conjectured that the volumetric expansion of the scale results in a distribution of pore sizes, starting from small at the metal-oxide interface to

large near the air-oxide interface. However, unlike the flat specimens, the initial pores formed tended to have a major axis tangential to the curved metal surface.

3.2.3 Internal Wedges.

Figure 7 shows the oxide evolution for internal wedges as a function of time and wedge angle. It can be seen that the scale formed on the internal wedges, at the wedge tip, has a morphology similar to the scale developed on the hollow cylinders. However, the oxide structure away from the wedge tip region resembles one-dimensional planar oxidation. From Fig. 7 it can also be seen that the oxide, at or near the wedge tip, shows no tendency to develop cracks, regardless of the oxidation time or wedge angle. In addition, there does not appear to be a substantive amount of void initiation and subsequent void expansion. These observations suggest the stress state in the oxide is similar to the case of a hollow cylinder. Furthermore, it can be seen that the tip of the wedge becomes increasingly more blunt as oxidation progresses. Finally, there are no oxide scale morphological features that appear to be a function of the internal wedge angle.

3.2.4 External Wedges.

The external wedge scale was found similar to the flat and solid cylinder specimens at the wedge tip. As can be seen in Fig. 8, the scale morphology is seen to have a rough surface texture that becomes rougher with time and is most likely due to the initial surface texture. The external wedges also have a layered, porous like structure, with the total void area increasing with time. In addition, independent of the wedge

angle, a crack originating at the origin of the wedge tip generally emanates outward. However, it is not know whether the fracture develops during oxidation or after the specimen is removed from the furnace. Further more, the wedge tip does not appear to become blunted, as was observed during oxidation of the internal wedge case. In addition, cracks can be seen to form on the planar surface parallel to the metal-oxide interface and are believed to be the result of cool down, as was observed in the solid cylinders. Finally, there are no oxide scale morphological features that appear to be a function of the external wedge angle.

3.3.1 Oxygen Weight-Gain Measurements (for flat specimens only).

Figure 9 shows a total oxygen weight-gain per unit surface area of the unoxidized specimen geometry after a 700°C exposure, plotted as a function of time. The total weight gain includes the oxygen weight-gain for both the oxide and the metal. These data were experimentally determined by normalizing the difference in measured weights of the unoxidized and oxidized specimens by the original specimen surface area. The points on the curve represent a simple arithmetic average of three experimental observations, with the error bars at each data point indicating the range of scatter for each measurement. These data were then used to determine the most appropriate oxidation constant for a parabolic rate law or a parabolic-to-linear transition rate equation.

Figure 9 shows three different Least Square curve fits of the experimental data. One curve is a parabolic fit of all observations. It is clear that while this fit captures the general trend of the data, it fails to accurately characterize the weight-gain at any specific time. Therefore, using the apriori assumption that oxidation behavior transitions from a parabolic to a linear response at some point during the oxidation exposure, the data were

further analyzed. To validate this assumption, rate constants were evaluated using the same Least Squares procedure, but only included data up to 24, 48, or 72 hours of oxidation, respectively. This evaluation yielded rate constants that were nearly identical for all three cases. Figure 9 shows the parabolic function based upon using experimental data through 48 hours and then extrapolated to 240 hours. While this rate coefficient can be seen to better describe the initial weight-gain, it produces unsatisfactory results when extrapolated out to 240 hours. This suggests that the oxidation process was initially parabolic, but then transitioned to a linear rate law at some time between 24 and 72 hours. The parabolic-to-linear (p/l) transition was accomplished by assuming a linear function having a slope equal to the slope of the parabolic function at the transition point. The transition point of 48 hours was selected by evaluating the rate constant for different parabolic fits that included data from 24 and 72 hours. Since the constant was nearly identical for all the cases, the transition point was assumed to lie somewhere between the two extreme points. Selecting the function that best represents the total oxygen weight gain was accomplished by comparing the Least Squares correlation coefficient, R, for each function ($R_{\text{all points}}$= 0.988, $R_{48\ \text{hrs}}$=0.953, and $R_{p/l}$=0.991). Since an R value of 1 implies a perfect fit of the data, the parabolic-to-linear transition function appears to be the better of the three curve fits.

A number of researchers (Jenkins[5,6], Wallwork and Jenkins[7], Kofstad, *et al.*[9], Stringer[11,12]), have reported that the parabolic rate will transition to a linear rate once a critical oxygen concentration is reached at the metal-oxide interface and a constant oxygen gradient is maintained in the metal. In this investigation, no oxygen concentration measurements were made at the metal-oxide interface. However, one

could assume that a critical concentration was obtained between 24 and 72 hours into oxidation, as evidenced by the void formation in the oxide (as shown in Fig. 4), as well as from the weight-gain data. The time to reach the transitions is longer than has been previously reported in the literature. However, it is believed that the additional time may be the result of the initial heat treatment of material.

3.3.2 Oxide thickness Measurements.

3.3.2.1 Flat Specimens:

Figure 10 presents oxide thickness measurements for the one-dimensional planar specimens, as a function of time. The points on the curve represent a simple arithmetic average of four experimental observations with the error bars at each data point indicating the range of scatter for each measurement. The figure also shows the one-dimensional planar thickness plotted using two different parabolic fits, as well as a parabolic-to-linear fit. Using the same analysis procedures, as were described in the weight-gain analysis for determining the best function to describe the oxide growth, a parabolic-to-linear transition function appears to be the better of the three curve fits ($R_{all\ points}$= 0.986, $R_{48\ hrs}$=0.960, and $R_{p/l}$=0.994).

3.3.2.2 Solid Cylinder Specimens:

Figures 11a-11c show the oxidation behavior for different diameter solid cylinders. Figure 11a indicates that oxidation behavior for the 50μm diameter solid cylinder. As previously described, three different functions were chosen to describe the oxide growth. For this diameter, the parabolic function obtained using all the data or

only data through 48 hours yielded identical R values ($R_{all\ points}$= 0.978, $R_{48\ hrs}$=0.978, and $R_{p/l}$=0.826). Therefore, this suggests that solid state diffusion mechanisms where most likely operative throughout the oxidation period. Since the 50μm diameter cylinder was not initially heat treated, as was the case of the other specimens, one could conclude that the initial oxygen concentration or grain size resulted in a delay of the metal-oxide interface reaching a critical oxygen concentration as previously described[7,9], even though the micrographs shown in Fig. 6 indicate the formation of numerous voids in the oxide beginning after 24 hours.

Figures 11b and 11c show the oxidation behavior of the larger diameter cylinders (125μm and 250μm). The same method for evaluating the best fit was used and yielded an unexpected result. The 125μm (shown in Fig. 11b) is best characterized by a parabolic-to-linear function ($R_{all\ points}$= 0.981, $R_{48\ hrs}$=0.951, and $R_{p/l}$=0.998), while the 250μm cylinder oxidation behavior is best represented by a parabolic function ($R_{all\ points}$= 0.994, $R_{48\ hrs}$=0.980, and $R_{p/l}$=0.972). The general trend of the data is consistent with other observations[18,24]; that is, the oxidation rate increases as the diameter of the cylindrical specimen decreases because of the reduced surface area as oxidation progresses. However, based upon earlier discussions the cylindrical specimens were expected to transition to linear oxidation in a shorter period of time than the flat specimens. Therefore, no precise reason can be offered to support why the oxidation of the 250μm cylinder follows a parabolic rate law out to 240 hours. The micrographs, shown in Fig. 6, indicate the scale morphology was consistent with that observed during linear oxidation of the one-dimensional planar specimens.

3.3.2.2 Hollow Cylinder Specimens:

Figure 12 shows the oxidation behavior of three different hollow cylinder geometries. The data indicate that parabolic oxidation mechanisms are most likely operative. As discussed in the previous section, the geometry dependent stress state in the oxide and adjoined metal are not conducive to void formation or exfoliation. This would account for the parabolic oxide growth through 72 hours. When comparing the effect of diameter, the results are just opposite of what was expected. That is, the 130μm diameter hollow cylinder was expected to show the slowest oxide growth due to the increasing reaction surface area as the oxidation progressed. However, this was not observed. Instead, the 343μm diameter hollow cylinder recorded the smallest oxide growth. One potential reason for the discrepancy is that the oxide thickness for all three cases is comparatively small and the relative differences between measurements, for any time, are less than 1μm. More conclusive evidence, which could be obtained after an extensive study involving many more samples than were used in this investigation, is needed in order to draw more specific conclusions. However, one observation can be made regarding curvature effects; that is, the overall oxide thickness is measurably smaller than that grown on the one-dimensional planar specimens or the solid cylinders. Therefore, the overall observation that oxide scale growth is faster on solid cylinders than on flat specimens; likewise, oxide growth is more rapid on flat specimens than on hollow cylinders, making it compatible with previous model predictions made by Lagoudas *et al.*[24].

4. Modeling Oxide Scale Growth Behavior

In this section, a Fickian diffusion based oxidation model is presented in order to investigate the scale-growth behavior on non-planar geometries. In addition, the procedures used to obtain the necessary input parameters for the model are shown. The parameters are evaluated using one-dimensional planar (flat) specimen experimental data of oxide thickness as a function of time for a specified temperature. The model has only a few adjustable parameters that need to be obtained from experiments. These include the diffusion coefficient of O_2 through TiO_2, $D_{(O_2,TiO_2)}$, the Pilling-Bedworth ratio, γ, and the oxygen concentration, c_0, at the oxide-air interface. For this investigation a value for c_0 was obtained from the available literature and was not measured. With all of the parameters evaluated from one-dimensional planar experiments, the model will subsequently be used to predict scale growth behavior on the surface of solid and hollow cylinders.

4.1 Model for Oxidation

This section describes three different oxidation problems – one-dimensional planar oxidation, oxidation on the outer surface of a solid cylinder, and oxidation on the inner surface of a hollow cylinder. The oxidation model used to solve these problems is based upon Fick's 1st law and accounts for solid state diffusion of oxygen through a substrate and volumetric expansion of the oxide[21]. The details of the model development have been omitted here, but the interested reader is referred to the work of Entchev, *et al.*[21] for a complete derivation.

Since the primary objective of the modeling effort was to investigate the effect volumetric expansion has on scale growth, several simplifying assumptions were made in

Submitted to: *Oxidation of Metals*
December 23, 1999
M.S. 1360, Resubmitted September 23, 2000
D.L Douglass
Arizonal Materials laboratories
Univ. Arizona, Tucson, AZ 85712
modified 9/23/2000

The Morphological Evolution of TiO_2 Scale Formed on Various 1-D and 2-D Geometries of Titanium

P.K. Imbrie and D.C. Lagoudas

Center for Mechanics of Composites
Department of Aerospace Engineering
Texas A&M University
College Station, TX 77843-3141

Abstract

The purpose of this study is to experimentally quantify the multi-dimensional growth characteristics of the oxide scale formed on commercially pure titanium at 700°C in a flowing air environment. The geometries considered herein had characteristic dimensions that were appropriately sized to match the thickness of the oxide scale and were fabricated into shapes of solid and hollow cylinders and external and internal wedges. Scanning electron microscopy (SEM) image analysis was used to measure the oxide layer thickness and the Pilling-Bedworth ratio (PBR) as a function of time. An effective diffusion coefficient was determined from one-dimensional planar oxide thickness data and experimentally obtained PBR values served as the necessary input to a solid state diffusion model, which was modified to account for the volumetric expansion of the oxide.

The model results demonstrate the competing influences of oxide expansion and curvature effects. In addition, the predictive capability of the model, for the case of a solid cylinder, was shown to under predict experimental results, whereas, scale growth on the inner surface of a hollow cylinder was over predicted. The differences are primarily attributed to an effective diffusion coefficient that varies the scale morphology. An oxide

layer grown on an outside surface of a solid cylinder or an external wedge was found to have a structure similar to one-dimensional planar oxide growth. On the contrary, scale developed on the inside surface of a hollow cylinder or an internal wedge was observed to be more compact.

Keywords: Image Analysis; Scanning Electron Microscopy (SEM); Titanium; Oxidation; Diffusion

1. Introduction

There continues to be widespread use of titanium and its alloys in the aerospace, petrochemical, gas/steam turbine, and automotive industries for a variety of structural applications. These materials are considered technically superior and cost-effective primarily because of their high strength-to-weight ratio, strength at moderate temperatures, and good resistance to creep and fatigue[1]. However, while they have excellent corrosion properties in gaseous oxygen and air at temperatures up to 600°C, at higher temperatures they exhibit poor long-term oxidation resistance due to scale formation and oxygen embrittlement. Since these materials are used to fabricate engineered components that generally involve some complex shape, understanding how oxidation will effect their useful life is important. Unfortunately, research to date has primarily been focused on one-dimensional planar oxidation behavior and its direct applicability to multidimensional case has not been considered.

In order to understand the general behavior of titanium oxidation, conclusions regarding its one-dimensional planar characteristics can be made from some of the

pioneering work of Gulbransen and Andrew[2], Davies and Birchnall[3], Morton and Baldwin[4], Jenkins[5-7], Kofstad, *et al.*[8-10], and Stringer[11,12], to name just a few. One primary observation by all these authors is the complex nature of oxidation kinetics in titanium. Kofstad, *et al.*[10] asserted that from a thermodynamic standpoint one could reason the formation of various oxides including: TiO; TiO_2; Ti_2O_3; and Ti_3O_5. However, he concluded only the rutile modification of TiO_2 has generally been observed for oxidation in oxygen below 1000°C.

Because the oxidation mechanisms of titanium change both with time and temperature, different reaction rates, and corresponding rate equations, are needed to describe its oxidation behavior[8]. Oxidation of titanium between 600°C and 1000°C, is typically initially described by a parabolic rate law. This parabolic time dependence represents two distinct processes: oxygen dissolution and oxide scale formation. The rate law is valid throughout the entire temperature range even though titanium undergoes an allotropic transformation from *h.c.p.* (α-Ti) to *b.c.c.* (β-Ti) at 882°C. Kofstad, *et al.*[8] suggests that the phase change has little effect on the oxidation mechanisms, except during the initial stages of the oxidation reaction.

The early stages of oxidation of titanium have been investigated by Vaquilla *et al.*[29] and Mizuno *et al.*[30], while the specific oxidation mechanisms for long-term parabolic oxidation have been extensively studied by a number of investigators[5,6,8-14,28]. There is general agreement that the process is dominated by the diffusion of oxygen in both the scale and the metal core and that scale growth is dependent upon the oxygen concentration gradient in the metal[5]. During the initial stage of oxidation, oxygen is absorbed on the surface of the metal by physisorption. The oxygen molecules dissociate

creating oxygen anions through a chemisorption process until a monolayer of oxide is formed[8]. Depending upon the oxygen concentration gradient in the metal, oxygen ions either pass through the thin film and are dissolved into the hexagonal titanium lattice at octahedral interstitial locations or produce fresh oxide. Continued growth of the oxide film is restricted by the need for the chemical potential of oxygen in the oxide film and the reacting titanium to be in equilibrium. If a non-equilibrium condition exists, the rate of oxygen dissolution becomes the prevailing mechanism. However, once the titanium at the metal/oxide interface becomes saturated with oxygen, the rate determining reaction is diffusion of oxygen ions through the oxide scale[5,6]. The TiO_2 scale has been characterized as an n-type semiconductor having an oxygen deficient structure that produces oxygen ion vacancies rather than interstitial titanium ions. Thus, there is an inward passage of oxygen produced by anion-vacancy diffusion through the rutile lattice[3,5-10,15]. It has also been shown that the activation energy for titanium ion diffusion is much greater than that of oxygen ion diffusion in TiO_2[5,8]. Therefore, for temperatures below 1000°C, it is generally believed that diffusion of titanium ions outward through the oxide layer is negligible. This was substantiated by Déchamps *et al.*[13] when they performed a study on the various diffusion mechanisms associated with titanium oxidation and concluded that solid state diffusion of titanium would be difficult because the monocrystalline rutile contains micropores, grain boundaries, and is stratified, all of which act as solid state diffusion barriers.

While a parabolic rate law describes the initial oxidation kinetics of titanium for this temperature range, the period for which it is valid is governed by the formation and growth of an initial coherent scale layer that grows to a critical thickness[6]. Once the

critical thickness is obtained, stresses in the scale and the metal at the metal-oxide interface become large enough to cause it to fail, resulting in the growth of fresh oxide. The critical thickness is associated with a steady-state oxygen concentration profile in the outer surface of the metal at the metal-oxide interface. At this point, there is a change from parabolic to linear oxidation. The transition to linear oxidation has been correlated to the oxygen concentration in the metal lattice at the interface. Andersson, *et al.*[16] showed oxygen concentrations reaching a value that corresponds to a composition of $TiO_{0.35}$ leads to structural changes in the solid solution. The expansion of the lattice leads to large compressive stresses that result in the detachment of a layer of $TiO_{0.35}$ followed by rapid oxidation of that layer[7,9,16]. Thus, heavy oxide formation begins to take place and the oxidation follows a linear rate[7,9]. While some researchers have observed a linear oxidation rate following an initial parabolic period, Lopes-Gomes and Huntz[15] and Bertrand[17] have reported that the linear behavior is really a series of successive parabolic steps. During each parabolic step, a new sub-layer is formed by the same mechanisms as described above.

A number of researchers, such as Jenkins[5], Kofstad, *et al.*[9], Stringer[11], Lopes-Gomes and Huntz[15] and Bertrand[17], have reported the TiO_2 oxide scale has a morphology that consists of two observable phases. The first phase is a comparatively compact zone that extends inward from the gas-oxide interface to a second phase of oxide that has a porous-laminar structure and extends to the metal-oxide interface. The various strata in the second phase vary in thickness, as well as number, depending upon the time and temperature of the exposed surface. Bertrand[17] observed a third oxide zone that was referred to as a non-stratified course grained crystallized structure appearing between the

second phase and the metal-oxide interface. In addition, Lopes-Gomes and Huntz[15] reported the individual layers were separated by cracks that extended over short distances which became visible only after the cooling of the specimen.

The aforementioned discussion summarizes observations regarding the characterization of one-dimensional planar titanium oxidation behavior. However, there are many engineering applications where understanding multi-dimensional oxidation behavior is important, such as at a crack tip or along a delaminating titanium-based metal matrix composite[18-20], and the direct applicability of one-dimensional planar observations to the multidimensional case have not been established. Therefore, the purpose of this investigation is to experimentally quantify the multi-dimensional growth characteristics of titanium oxide scale. Since adding alloying elements to titanium can affect its oxidation behavior in a variety of different ways[6], the case involving the simplest form will be considered herein using commercially pure titanium. The experiments will be conducted at 700°C in a flowing air environment for oxidation times up to 240 hours. While typical engineering applications of titanium find use at temperatures between 500 and 600°C, 700°C is chosen because the same parabolic oxidation mechanisms can still be observed and the time to grow a sufficiently thick oxide layer is significantly shorter. In addition, most of the literature on titanium oxidation is limited to relatively short oxidation periods, i.e. hours or tens of hours. Therefore, a long-term exposure is desired in order to investigate the effects on the oxide morphology.

The geometries considered herein-included solid and hollow cylinders, as well as external and internal wedges and were chosen due to their importance in representing a wide range of useful shapes, especially in metal matrix composites. The measured

quantities were weight gain and oxide layer thickness for a specified exposure. In addition, optical microscopy and scanning electron microscopy (SEM) are used to evaluate the morphological evolution of the oxide scale. In addition, 1D oxidation data are obtained in order to compute constants for a multi-dimensional solid state diffusion model that is based upon Fick's 1st Law which has been modified by Entchev, *et al.*[21] to account for the volumetric expansion of the oxide scale. The constants, along with the results of the multi-dimensional experiments, are then used to verify the predictive capabilities of the model.

In the sections that follow, the experimental procedures used in this investigation are described. This is followed by a discussion of the experimental results, which includes both an evaluation of the measured data, as well as observations regarding the scale morphology for the various multi-dimensional geometries. Finally, a brief overview the oxidation model is presented along with the methods used to evaluate the necessary input data. Model results are then compared to experimental data for the oxidation of an internal wedge.

2. Experimental Procedures

2.1 Material.

The materials selected for this research were obtained in sheet and wire forms. The sheet stock was commercially pure (CP), ASTM grade 1, unalloyed titanium manufactured by Timet, Inc., Morgantown, PA, under the product name of Timetal® 35A. The material was produced from titanium sponge using an Electron Beam (EB) cold hearth furnace process where the resulting remelt electrodes were formed into ingots

by a Vacuum Arc Reduction furnace (VAR). The VAR ingots were then forged into slabs and subsequently milled, through a series of hot and cold rolling stages, to final average thickness of 0.65 mm. The nominal chemical analysis of the Timetal® 35A material, in maximum allowable weight percent, was 0.006 N, 0.005 C, 0.030 Fe, and 0.040 O with the balance being Ti.

The wire stock was unalloyed titanium manufactured by Goodfellow Corp, Berwyn, PA, to a specified purity and diameter. The wire was fabricated using a cold draw process which eventually reduce the ingot material to nominal diameters of 0.25 mm, 0.125 mm, and 0.05 mm, with each wire diameter having a titanium purity of 99.6%, 99.6% and 99.8%, respectively. No energy dispersive X-ray spectroscopy (EDS) or electron microprobe (EM) characterization studies were performed on the as-received material in order to quantify the level of impurities. However, a typical chemical analysis suggested by the manufacturer, in weight percent, was 0.0005 Cu, 0.002 Ca, 0.005 Cr, 0.005 Ni, 0.006 H, 0.01 Mn, 0.015 N, 0.02 Sn, 0.03 Al, 0.03 C, 0.03 Si, 0.15 Fe, and 0.2 O with remainder being Ti for the material considered 99.6% pure. Similarly, the chemical composition for the 99.8% pure titanium was typically suggested to be 0.0001 Al, 0.001 Cu, 0.001 Mg, 0.002 Ni, 0.003 Cr, 0.003 Si, 0.005 Ni, 0.005 V, 0.008 H, 0.009 Fe, 0.04 Mn, and 0.04 O with the remainder being Ti.

2.2 *Specimen fabrication and preparation.*

The specimen geometries used for this investigation included: 1)flat specimens; 2)solid and hollow cylinder specimens; and 3)internal and external wedge specimens as shown schematically in Fig. 1. The specimens were fabricated from either sheet or wire

stock material and are shown in their finished state via SEM images in Fig. 2. The nominal target dimensions for the various specimen configurations depicted in Fig 1 and 2, are shown in Table 1. This table provides details as to the approximate size and shape of the various specimens. However, it should be noted that nominal dimensions provided for comparison purposes only. Where appropriate, the actual measurements for each individual specimen were used for subsequent data analysis.

All samples made from sheet stock were fabricated from the same stock of bulk material. Individual samples were sectioned to their respective length and width with a diamond cutoff saw. A hole was mechanically drilled through the thickness at one end of each sample in order to suspend the specimen during testing. In order to eliminate variances in the specimen-to-specimen initial surface texture, the specimens were wet ground to a uniform surface finish using silicon carbide paper through 2000 ANSI grit. All samples prepared from wire stock were simply cut to length and oxidized with the "as-received" surface finish.

Additional machining operations were used to fabricate the specific cylindrical and wedge specimen geometries shown in Fig. 1 and 2. These included: 1) mechanically drilling the holes to produce the hollow cylinder samples; 2) milling the included angle on the edge of the outside wedge specimens; and 3) broaching the V groove into the surface of the inside wedge samples. No subsequent grinding procedure was preformed to refine the "as-machined" surface finish.

After fabrication, the samples were first cleaned in acetone, then chemically etched in a solution of 4.2% HF + 12.5% HNO_3 + 83.3% H_2O for 60 seconds, and then rinsed in isopropyl alcohol in order to remove any residual enchant. The specimens were

then annealed for 24 hours at 800°C in a vacuum better than 5 x 10^{-6} torr. This was done to obtain a reference microstructure, as well as ensure that the grain size would not change during the oxidation. However, during the annealing step, the 0.05mm diameter solid cylinder samples became to brittle to handle, and were tested using the "as received" microstructure. In addition, the 30° internal wedge samples became blunted during the heat treatment. The blunting of the wedge tip is assumed to be the result of stress-relief from stresses developed during the fabrication process. Since no other micro-machining methods were available, the 30° internal wedge geometry was abandon. The remaining vacuum annealed samples were then acid-cleaned in the solution described above for 10 seconds, ultrasonically rinsed in isopropyl alcohol, and then stored in isopropyl alcohol for subsequent measurement and testing.

The type of initial measurements made on each specimen were a function of the intended experiment. For the weight gain study, the dimensions of the finished samples were measured to the nearest 0.00025 cm and had a repeatability standard deviation of 0.0064. In addition, each sample was initially weighed in air, as well as in H_2O on a Mettler AB 204 analytical balance. The balance had an absolute accuracy of ±1 mg with a repeatability of ±0.1 mg. Individual weight measurements were performed on each sample, since a thermogravimetric analysis unit (TGA) was not used.

Samples used to obtain oxide layer behavior as a function of time, were quantified by obtaining a reference configuration via scanning electron microscopy (SEM). The length scales of the unoxidized specimens were established by using micro laytex spheres (1.072 μm or 10.568 μm diameter) on the surface of each specimen.

2.3 *Oxidation Experiments.*

Oxidation tests were performed in a Ney 2-160 muffle-type furnace that had a heated volume of 1845 cm^3. The experiments were conducted at 700°C (±1°C) in dry flowing laboratory air (7 l/m) for various oxidation times up to 240 hours as shown in Table 2. Initially, the flat specimens and the solid cylinders were subjected to a long-term oxidation exposure. However, since micrographs of these specimens did not reveal any significant morphological differences from the 72 hour oxide scale, the remaining experiments were only carried out to only 72 hours with an additional test point of 36 hours being added. Table 2 also indicates the number of specimens that were used as part of this test program. While only one specimen was oxidized for each of the 2D geometries, three different planar oxide thickness measurements were made in order to obtain an average value. Similarly, a total of 4 weight gain measurements were used to obtain an average value for the weight gain analysis.

The specimens were suspended in the center of the furnace chamber by Inconel® rods as shown in Fig. 3. The procedure for initiating the oxidation experiments was to first allow the furnace to reach a steady value at the test temperature for 12 hours. Then the furnace door was opened and the suspension rods (with the samples) were placed on their supports. No attempt was made to take into account the specimen temperature rise time other than to note that the furnace temperature recovered to 99% of its set point value in 45 seconds and was fully recovered in 300 seconds. At the designated exposure times, individual specimens were extracted from the furnace and stored in a vacuum for later processing.

2.4 *Oxide Growth Characterization.*

Oxidized specimens were evaluated by oxide thickness measurements and/or weight gain analysis as a function of time. For the weight gain analysis, both the change in mass and the reference surface area of each specimen were the measured quantities. The pre and post-test mass of a specimen were measured on the same analytical balance. Since an orthogonal specimen configuration was not guaranteed during fabrication, the reference surface area was estimated in the following manner. First, the density of the sample was determined by applying Archimedes Principal to the measured weight of a specimen that was obtained from an analytical balance in both air and distilled water. Then, the volume of the specimen was computed given its known density (ρ) and mass (m). Next, the surface area perpendicular to the thickness, S_A, (see Fig. 1) was obtained, assuming the specimen had a constant thickness (z) and using the relation $S_A = V / z$. Finally, the reference surface area, A, was computed by

$$A = 2(S_A) + (P + 2\pi r) \cdot z, \tag{1}$$

where P is the perimeter length around S_A and r is the radius of the specimen suspension hole.

The characterization of the titanium and oxide microstructure, as well as inspection of the scale morphology was performed by examining various cross-sectioned specimen configurations (after mounting) before and after oxidation using SEM. The samples were prepared for SEM evaluation by potting them in a cold mount thermal-set epoxy resin and then grinding and polishing them on a Struers Rotopol automated polishing system. Each sample was first wet-ground to a uniform surface finish using silicon carbide paper through 2000 ANSI grit and then polished. The polishing steps

included using a 3 μm diamond suspension on a satin woven acetate cloth for 3 minutes. This was followed by using a colloidal silica solution (45% colloidal Si + 45% H_20 + 9% H_2O_3 + 0.5% HNO_3 + 0.5% HF) on a medium hard neoprene cloth for 5 minutes.

Precise oxide thickness measurements were performed by establishing an accurate length scale using micro laytex spheres (1.072 μm or 10.568 μm diameter) on the surface of each epoxy mount. Oxide growth evolution was evaluated by comparing the before and after oxidation configurations of each specimen.

3. Experimental Results

3.1 Scale Morphology for Different Geometries.

3.1.1 Flat Specimens

The morphological evolution of the TiO_2 scale formed at 700°C was observed via optical microscopy, as well as SEM. A visual inspection (using a 5x optical microscope) of the exterior features of the oxide revealed that initially a thin slate-gray colored scale was formed on the titanium substrate. As time proceeded, its color changed from slate-gray to off-white pale yellow and finally to a light brown after 240 hours of exposure. The surface texture of the scale was, at first, smooth and one could easily discern preferential oxide growth corresponding to the pre-oxidized surface grain structure. However, as the oxide layer grew in thickness, it became noticeably more rough and its grain-like appearance diminished with time. After approximately 36 hours of exposure, surface cracks were observed forming along the edges of the specimen. These surface cracks grew with time and eventually opened wide enough to reveal other large fissures

within the multi-layered scale, as well as regions of oxide spalling at or near the corners of the specimen.

Figure 4 provides insight as to the one-dimensional planar development of the oxide scale as a function of time. After 10 hours of exposure, it can be seen that the oxide scale appears to be coherent and free of any observable defects, which is consistent with observations made by Jenkins[6]. However, as the exposure time increases, three different oxide structures can be observed (see Fig 4 after 20 hours of oxidation). The scale adjacent the air-oxide interface appears to be compact, while the interior scale has numerous voids and the scale at or near the metal-oxide interface is void-free but more granular than the scale at the air-oxide interface. It is presumed that the compact scale observed at the air-oxide interface after 20 hours has be displaced from the metal-oxide interface because of new oxide formation. As the oxidation process continues, the new-growth oxide is subjected to various stresses that in turn cause it to fail, creating a porous structure. Stringer[11] attributes void formation to the creation of scale blisters, which result in localized buckling of the oxide layer. Whereas Lopes-Gomes and Huntz[15] indicate that the voids are formed when stresses arising between the expanded α-solid solution and the more voluminous oxide induce partial cracking between the metal and the oxide scale at the metal-oxide interface. The voids, which are first observed after approximately 20 to 24 hours of oxidation, appear to have a long needle-like geometry with the axis of the needle running perpendicular to the metal-oxide interface. However, as the oxide scale grows, the same voids move away from the metal-oxide interface and gradually take on a larger more ellipsoidal shape after 48 hours. This suggests either the oxide is expanding, the stress state in the scale is changing, or some combination of both.

While no attempt was made to quantify the distribution of void sizes, there is a general trend for the voids to be smallest near the metal-oxide interface and grow in size as one moves away from the metal surface.

The micorgraphs in Fig. 4 also reveal that the interior scale has a layered-like structure with the layers growing parallel to the metal-oxide interface, as mentioned in the introduction. While it is believed that the layers exist for exposures as short as 20 hours, more direct evidence of their presence can be observed in the micrographs after 72 hours of oxidation. Stringer[11] reported that the interior layers of scale are actually porous to gaseous oxygen, which would imply the voids observed herein might be interconnected. However, the permeability of the oxide formed during these experiments to gaseous oxygen was not investigated. In addition, if each layer is accompanied by the formation of new voids, one would expect there to be uniformly distributed throughout the total scale thickness. However, this was not observed in these experiments. Instead, there appeared to be a greater concentration of voids away from the metal-oxide interface. This would suggest that the increased thickness of the scale reduced the propensity for a newly forming layer to buckle.

In addition to void development, cracks were also observed. In most cases, cracks were observed to develop at the interface between the porous layers. Once initiated, they would either continue growing in a direction parallel to the metal-oxide interface or they would change direction and propagate to the surface. The cracking phenomenon is consistent with observations by other investigators who have performed acoustic transmission studies during oxidation[22].

The aforementioned observations regarding the scale morphology suggest that diffusion of oxygen through the oxide scale cannot be adequately described by a single mechanism. As was previously stated, it is believed that during the formation of the compact scale, anion-vacancy diffusion is the oxygen transport mechanism. However, once the oxide begins to crack and/or localized blistering occurs, gaseous oxygen is then allowed to rapidly penetrate down to the reaction surface. The diffusion mechanism returns to ionic transport once a new compact oxide film/layer is formed and the process repeats itself.

3.2 2D Geometries.

Four different geometries were tested in order to investigate the formation of oxide scale on curved surfaces, as well as on intersecting planar surfaces. The geometries included hollow cylinders, solid cylinders, internal wedges, and external wedges. The sections that follow describe the morphological similarities and differences observed between the various geometries.

3.2.2 Hollow Cylinders.

The formation of oxide scale on the hollow cylinders showed no unique differences between the three initial diameters tested. Therefore, Fig. 5 serves as a representative example of the development of the oxide layer as a function of exposure time. The scale has several notable differences from the oxide scale formed on a flat specimen for the same oxidation time and temperature (for example see Fig. 4). These differences include: 1) there did not appear to be a tendency for the scale to detach from

the metal, regardless of the oxidation time; 2) the surface texture of the scale was smooth; and 3) there did not appear to be a substantive amount of void initiation and subsequent void expansion as was observed in the flat specimens. It is believed the lower level of void formation in the hollow cylinder specimen geometry is due to the stress-state in the oxide. The curved geometry most likely produces larger compressive stresses in the oxide scale, which in turn produces higher tensile hoop stresses in the metal. The larger hoop stresses in the metal then offset the compressive stresses being developed as a result of the dissolution of oxygen into the metal lattice. Since deformation of the metal lattice eventually causes the oxide at the metal-oxide interface to fracture, any reduction in the local stress would reduce the number of cracks formed that serve as void initiation points. In addition, it is believed that the curvature of the hollow cylinder results in a higher buckling resistance for the TiO_2 scale, which reduces the blistering phenomena observed by others[11,15]. Lastly, while not easily seen in Fig. 5, a close inspection of scale reveals that it is composed of several layers that develop radially inward from the air-oxide interface.

3.2.2 Solid Cylinders.

Scale formation on the solid cylinders was similar to that developed on the flat specimens. For short oxidation times, the oxide scale appears to be compact, as well as firmly attached to the metal substrate, regardless of the amount of surface curvature. However, as the oxidation time increases, the compact layer moves away from the metal-oxide interface and is replaced by a porous-layered oxide structure (see Fig. 6).

Figure 6 also shows, for the cylinder diameters tested, there is a tendency for radial cracks to develop. However, it is not known whether these cracks are actually formed during the oxidation exposure or are a cool-down artifact resulting from a mismatch between the coefficients of thermal expansion of the two materials ($\alpha_{Ti} = 9.2 \times 10^{-6} / ^{\circ} C^{23}$ and $\alpha_{TiO_2} = 8.0 \times 10^{-6} / ^{\circ} C^{23}$). In addition, there appears to be very few cracks, if any, forming circumferentially around the specimen. This is inconsistent with crack development in the flat specimen oxide, where fracture parallel to the metal-oxide interface was generally observed. The circumferential cracks shown in Fig. 6 most likely formed during cool down, since no fresh oxide appears to have formed on the metal-oxide interface.

The micorgraphs shown in Fig. 6 also reveal a changing surface texture with exposure time and surface curvature. The scale appears to be relatively smooth for short oxidation exposures and becomes rougher with time, as well as cylinder radius. However, it is believed that the changing scale roughness is not necessarily a function of the geometry, but rather is simply an artifact of the initial surface roughness of the specimen.

The oxide scale was observed to be similar to that developed on the flat specimens, that is, the outer scale appears to by compact, while the interior scale has a porous layered-like structure. In addition, as new layers of the oxide form, the initial pores become more evident, suggesting that the preceding layers continue to expand. This expansion is accompanied by a corresponding expansion of the individual pores previously created. Therefore, it is conjectured that the volumetric expansion of the scale results in a distribution of pore sizes, starting from small at the metal-oxide interface to

large near the air-oxide interface. However, unlike the flat specimens, the initial pores formed tended to have a major axis tangential to the curved metal surface.

3.2.3 Internal Wedges.

Figure 7 shows the oxide evolution for internal wedges as a function of time and wedge angle. It can be seen that the scale formed on the internal wedges, at the wedge tip, has a morphology similar to the scale developed on the hollow cylinders. However, the oxide structure away from the wedge tip region resembles one-dimensional planar oxidation. From Fig. 7 it can also be seen that the oxide, at or near the wedge tip, shows no tendency to develop cracks, regardless of the oxidation time or wedge angle. In addition, there does not appear to be a substantive amount of void initiation and subsequent void expansion. These observations suggest the stress state in the oxide is similar to the case of a hollow cylinder. Furthermore, it can be seen that the tip of the wedge becomes increasingly more blunt as oxidation progresses. Finally, there are no oxide scale morphological features that appear to be a function of the internal wedge angle.

3.2.4 External Wedges.

The external wedge scale was found similar to the flat and solid cylinder specimens at the wedge tip. As can be seen in Fig. 8, the scale morphology is seen to have a rough surface texture that becomes rougher with time and is most likely due to the initial surface texture. The external wedges also have a layered, porous like structure, with the total void area increasing with time. In addition, independent of the wedge

angle, a crack originating at the origin of the wedge tip generally emanates outward. However, it is not know whether the fracture develops during oxidation or after the specimen is removed from the furnace. Further more, the wedge tip does not appear to become blunted, as was observed during oxidation of the internal wedge case. In addition, cracks can be seen to form on the planar surface parallel to the metal-oxide interface and are believed to be the result of cool down, as was observed in the solid cylinders. Finally, there are no oxide scale morphological features that appear to be a function of the external wedge angle.

3.3.1 Oxygen Weight-Gain Measurements (for flat specimens only).

Figure 9 shows a total oxygen weight-gain per unit surface area of the unoxidized specimen geometry after a 700°C exposure, plotted as a function of time. The total weight gain includes the oxygen weight-gain for both the oxide and the metal. These data were experimentally determined by normalizing the difference in measured weights of the unoxidized and oxidized specimens by the original specimen surface area. The points on the curve represent a simple arithmetic average of three experimental observations, with the error bars at each data point indicating the range of scatter for each measurement. These data were then used to determine the most appropriate oxidation constant for a parabolic rate law or a parabolic-to-linear transition rate equation.

Figure 9 shows three different Least Square curve fits of the experimental data. One curve is a parabolic fit of all observations. It is clear that while this fit captures the general trend of the data, it fails to accurately characterize the weight-gain at any specific time. Therefore, using the apriori assumption that oxidation behavior transitions from a parabolic to a linear response at some point during the oxidation exposure, the data were

further analyzed. To validate this assumption, rate constants were evaluated using the same Least Squares procedure, but only included data up to 24, 48, or 72 hours of oxidation, respectively. This evaluation yielded rate constants that were nearly identical for all three cases. Figure 9 shows the parabolic function based upon using experimental data through 48 hours and then extrapolated to 240 hours. While this rate coefficient can be seen to better describe the initial weight-gain, it produces unsatisfactory results when extrapolated out to 240 hours. This suggests that the oxidation process was initially parabolic, but then transitioned to a linear rate law at some time between 24 and 72 hours. The parabolic-to-linear (p/l) transition was accomplished by assuming a linear function having a slope equal to the slope of the parabolic function at the transition point. The transition point of 48 hours was selected by evaluating the rate constant for different parabolic fits that included data from 24 and 72 hours. Since the constant was nearly identical for all the cases, the transition point was assumed to lie somewhere between the two extreme points. Selecting the function that best represents the total oxygen weight gain was accomplished by comparing the Least Squares correlation coefficient, R, for each function ($R_{\text{all points}}$= 0.988, $R_{48\ \text{hrs}}$=0.953, and $R_{p/l}$=0.991). Since an R value of 1 implies a perfect fit of the data, the parabolic-to-linear transition function appears to be the better of the three curve fits.

A number of researchers (Jenkins[5,6], Wallwork and Jenkins[7], Kofstad, *et al.*[9], Stringer[11,12]), have reported that the parabolic rate will transition to a linear rate once a critical oxygen concentration is reached at the metal-oxide interface and a constant oxygen gradient is maintained in the metal. In this investigation, no oxygen concentration measurements were made at the metal-oxide interface. However, one

could assume that a critical concentration was obtained between 24 and 72 hours into oxidation, as evidenced by the void formation in the oxide (as shown in Fig. 4), as well as from the weight-gain data. The time to reach the transitions is longer than has been previously reported in the literature. However, it is believed that the additional time may be the result of the initial heat treatment of material.

3.3.2 Oxide thickness Measurements.

3.3.2.1 Flat Specimens:

Figure 10 presents oxide thickness measurements for the one-dimensional planar specimens, as a function of time. The points on the curve represent a simple arithmetic average of four experimental observations with the error bars at each data point indicating the range of scatter for each measurement. The figure also shows the one-dimensional planar thickness plotted using two different parabolic fits, as well as a parabolic-to-linear fit. Using the same analysis procedures, as were described in the weight-gain analysis for determining the best function to describe the oxide growth, a parabolic-to-linear transition function appears to be the better of the three curve fits ($R_{all\ points}$= 0.986, $R_{48\ hrs}$=0.960, and $R_{p/l}$=0.994).

3.3.2.2 Solid Cylinder Specimens:

Figures 11a-11c show the oxidation behavior for different diameter solid cylinders. Figure 11a indicates that oxidation behavior for the 50μm diameter solid cylinder. As previously described, three different functions were chosen to describe the oxide growth. For this diameter, the parabolic function obtained using all the data or

only data through 48 hours yielded identical *R* values ($R_{all\ points}$= 0.978, $R_{48\ hrs}$=0.978, and $R_{p/l}$=0.826). Therefore, this suggests that solid state diffusion mechanisms where most likely operative throughout the oxidation period. Since the 50μm diameter cylinder was not initially heat treated, as was the case of the other specimens, one could conclude that the initial oxygen concentration or grain size resulted in a delay of the metal-oxide interface reaching a critical oxygen concentration as previously described[7,9], even though the micrographs shown in Fig. 6 indicate the formation of numerous voids in the oxide beginning after 24 hours.

Figures 11b and 11c show the oxidation behavior of the larger diameter cylinders (125μm and 250μm). The same method for evaluating the best fit was used and yielded an unexpected result. The 125μm (shown in Fig. 11b) is best characterized by a parabolic-to-linear function ($R_{all\ points}$= 0.981, $R_{48\ hrs}$=0.951, and $R_{p/l}$=0.998), while the 250μm cylinder oxidation behavior is best represented by a parabolic function ($R_{all\ points}$= 0.994, $R_{48\ hrs}$=0.980, and $R_{p/l}$=0.972). The general trend of the data is consistent with other observations[18,24]; that is, the oxidation rate increases as the diameter of the cylindrical specimen decreases because of the reduced surface area as oxidation progresses. However, based upon earlier discussions the cylindrical specimens were expected to transition to linear oxidation in a shorter period of time than the flat specimens. Therefore, no precise reason can be offered to support why the oxidation of the 250μm cylinder follows a parabolic rate law out to 240 hours. The micrographs, shown in Fig. 6, indicate the scale morphology was consistent with that observed during linear oxidation of the one-dimensional planar specimens.

3.3.2.2 Hollow Cylinder Specimens:

Figure 12 shows the oxidation behavior of three different hollow cylinder geometries. The data indicate that parabolic oxidation mechanisms are most likely operative. As discussed in the previous section, the geometry dependent stress state in the oxide and adjoined metal are not conducive to void formation or exfoliation. This would account for the parabolic oxide growth through 72 hours. When comparing the effect of diameter, the results are just opposite of what was expected. That is, the 130μm diameter hollow cylinder was expected to show the slowest oxide growth due to the increasing reaction surface area as the oxidation progressed. However, this was not observed. Instead, the 343μm diameter hollow cylinder recorded the smallest oxide growth. One potential reason for the discrepancy is that the oxide thickness for all three cases is comparatively small and the relative differences between measurements, for any time, are less than 1μm. More conclusive evidence, which could be obtained after an extensive study involving many more samples than were used in this investigation, is needed in order to draw more specific conclusions. However, one observation can be made regarding curvature effects; that is, the overall oxide thickness is measurably smaller than that grown on the one-dimensional planar specimens or the solid cylinders. Therefore, the overall observation that oxide scale growth is faster on solid cylinders than on flat specimens; likewise, oxide growth is more rapid on flat specimens than on hollow cylinders, making it compatible with previous model predictions made by Lagoudas *et al.*[24].

4. Modeling Oxide Scale Growth Behavior

In this section, a Fickian diffusion based oxidation model is presented in order to investigate the scale-growth behavior on non-planar geometries. In addition, the procedures used to obtain the necessary input parameters for the model are shown. The parameters are evaluated using one-dimensional planar (flat) specimen experimental data of oxide thickness as a function of time for a specified temperature. The model has only a few adjustable parameters that need to be obtained from experiments. These include the diffusion coefficient of O_2 through TiO_2, $D_{(O_2,TiO_2)}$, the Pilling-Bedworth ratio, γ, and the oxygen concentration, c_0, at the oxide-air interface. For this investigation a value for c_0 was obtained from the available literature and was not measured. With all of the parameters evaluated from one-dimensional planar experiments, the model will subsequently be used to predict scale growth behavior on the surface of solid and hollow cylinders.

4.1 Model for Oxidation

This section describes three different oxidation problems – one-dimensional planar oxidation, oxidation on the outer surface of a solid cylinder, and oxidation on the inner surface of a hollow cylinder. The oxidation model used to solve these problems is based upon Fick's 1st law and accounts for solid state diffusion of oxygen through a substrate and volumetric expansion of the oxide[21]. The details of the model development have been omitted here, but the interested reader is referred to the work of Entchev, *et al.*[21] for a complete derivation.

Since the primary objective of the modeling effort was to investigate the effect volumetric expansion has on scale growth, several simplifying assumptions were made in

order to facilitate the analysis. They included: 1) the reaction at the metal-oxide interface is instantaneous (forming TiO_2); 2) the solution of O_2 in TiO_2 is dilute; 3) equilibrium is established at the air-oxide interface and the metal region (Ti) is oxygen-free; and 4) the concentration of Ti, $c_{(Ti)}$ and TiO_2, $c_{(TiO_2)}$, is constant. In this work, the aforementioned concentrations are defined as the ratio of the density to molecular weight of the respective material. In addition, as originally developed, the model is based upon the diffusion of O_2 through the oxide instead of ionic vacancy diffusion, as was presented earlier. However, while this may create a conceptual inconsistency, the mathematics of the model, properly normalized lead to the same result. Therefore, the same notation used in[21] will be used herein for the sake of consistency. It is further noted that the first assumption stated above will preclude oxygen dissolution into the metal, as noted by many researchers, e.g., Kofstad [10]. However, since the primary objective of the modeling effort was to investigate the effect of the volumetric expansion on scale growth, oxygen dissolution, as well as other features of the oxidation process, like scale detachment, have not been explicitly accounted for. The influence of theses effects will be taken into account in the present model by the way the diffusion coefficient is evaluated from the experimental observations.

4.1.1 One-Dimensional Planar Oxidation.

By selecting a frame of reference with its origin at the air-oxide interface, the mass balance of O_2 in the oxide can be written as

$$\frac{\partial c_{(O_2)}}{\partial t} - D_{(O_2,TiO_2)} \frac{\partial^2 c_{(O_2)}}{\partial x^2} = 0, \tag{3}$$

where $c_{(O_2)}$ is the molecular concentration of oxygen in the oxide region. The boundary conditions are specified as

$$\left.\begin{aligned} c_{(O_2)}\big|_{x=0} &= c_0 \\ c_{(O_2)}\big|_{x=h(t)} &= 0 \end{aligned}\right\}, \tag{4}$$

where c_0 is the concentration of oxygen available to diffuse through the oxide and $h(t)$ represents the position of the metal-oxide interface (oxide thickness). It should be noted that the assumption of an instantaneous reaction rate and zero initial concentration of oxygen in the metal, results in zero oxygen concentration in the metal for all time. Thus, the velocity of the metal-oxide interface, w_x, can be obtained using the jump mass balance such that

$$w_x = -\frac{D_{(O_2,TiO_2)}}{c_{(TiO_2)}} \frac{\partial c_{(O_2)}}{\partial x}\bigg|_{x=h(t)}. \tag{5}$$

An analytical solution to one-dimensional problems in terms of error functions is presented in the work of Entchev, *et al.*[21]. The thickness of the oxide layer is given by a parabolic function

$$h(t) = \alpha\sqrt{t}\,. \tag{6}$$

The interface condition given by eq. (5) and the oxide thickness function given by eq. (6), along with substituting $\gamma \equiv c_{(Ti)} / c_{(TiO_2)}$, leads to the non-linear algebraic equation for the evaluation of the diffusion coefficient $D_{(O_2,TiO_2)}$[21]

$$\frac{\alpha}{\sqrt{4D_{(O_2,TiO_2)}}}\exp\left(\frac{\alpha^2}{4D_{(O_2,TiO_2)}}\right)\mathrm{erf}\left(\frac{\alpha}{\sqrt{4D_{(O_2,TiO_2)}}}\right)=\frac{1}{\sqrt{\pi}}\frac{\gamma c_0}{c_{(Ti)}}, \tag{7}$$

where α and γ are determined from one-dimensional planar oxidation experimental data of oxide thickness, as shown below.

4.1.2 Oxidation of a Solid Cylinder.

This section describes the procedure used to simulate scale growth behavior on the outer surface of a solid cylinder. Again, the reader is referred to work of Entchev, *et al.*[21] for the specific details of the model development.

By selecting a frame of reference in the center of the cylinder, as well as exploiting the symmetry of the problem (see Fig. 13), the governing equation, written in cylindrical coordinates, can be expressed as

$$\frac{\partial c_{(O_2)}}{\partial t}-D_{(O_2,TiO_2)}\frac{1}{r}\frac{\partial}{\partial r}\left(r\frac{\partial c_{(O_2)}}{\partial r}\right)-\frac{1}{r}\frac{(1-\gamma)R_i D_{(O_2,TiO_2)}}{c_{(Ti)}}\frac{\partial c_{(O_2)}}{\partial r}\bigg|_{r=R_i}\frac{\partial c_{(O_2)}}{\partial r}=0, \tag{8}$$

with boundary conditions

$$\begin{aligned} c_{(O_2)} &= c_0 \quad \text{at} \quad r=R_o \\ c_{(O_2)} &= 0 \quad \text{at} \quad r=R_i \end{aligned}, \tag{9}$$

and the expressions for the velocities of the air-oxide (a-o) and metal-oxide (m-o) interfaces are written as

$$w_r^{m-o}=-\frac{1}{c_{(Ti)}}D_{(O_2,TiO_2)}\frac{\partial c_{(O_2)}}{\partial r}\bigg|_{r=R_i}, \tag{10}$$

$$w_r^{a-o} = -\frac{R_i}{R_o}\frac{1}{c_{(\mathrm{Ti})}} D_{(\mathrm{O_2},\mathrm{TiO_2})} \left.\frac{\partial c_{(\mathrm{O_2})}}{\partial r}\right|_{r=R_i} (1-\gamma), \qquad (11)$$

where R_i and R_o are the positions of the metal-oxide and air-oxide interface, respectively. In addition, one should note that w_r^{a-o} and w_r^{m-o} represent the r component of their respective interface velocity component.

Since an analytical solution to this moving interface problem is not available, eq. (9) has been discretized both in time and position and the Finite Difference Method used to obtain a numerical solution[21]. The model parameters necessary to implement a solution to this problem are $D_{(\mathrm{O_2},\mathrm{TiO_2})}$ (which is obtain from eq. (7) knowing α), γ, c_0, $c_{(Ti)}$, and the initial outer radius of the solid cylinder.

4.1.3 Oxidation of a Hollow Cylinder.

This section describes the procedure used to simulate scale growth behavior on the inner surface of a hollow cylinder. By selecting a frame of reference in the center of the cylinder, as well as exploiting the symmetry of the problem (see Fig. 14), the governing equation, written in cylindrical coordinates, can be expressed as

$$\frac{\partial c_{(\mathrm{O_2})}}{\partial t} - D_{(\mathrm{O_2},\mathrm{TiO_2})}\frac{1}{r}\frac{\partial}{\partial r}\left(r\frac{\partial c_{(\mathrm{O_2})}}{\partial r}\right) - \frac{1}{r}\frac{(1-\gamma)R_o D_{(\mathrm{O_2},\mathrm{TiO_2})}}{c_{(\mathrm{Ti})}}\left.\frac{\partial c_{(\mathrm{O_2})}}{\partial r}\right|_{r=R_o}\frac{\partial c_{(\mathrm{O_2})}}{\partial r} = 0, \qquad (12)$$

with boundary conditions

$$\begin{aligned} c_{(O_2)} &= c_0 \quad \text{at} \quad r = R_i \\ c_{(O_2)} &= 0 \quad \text{at} \quad r = R_o \end{aligned}, \qquad (13)$$

and the expressions for the velocities of the air-oxide (a-o) and metal-oxide (m-o) interfaces are written as

$$w_r^{m-o} = -\frac{1}{c_{(\mathrm{Ti})}} D_{(\mathrm{O_2},\mathrm{TiO_2})} \left.\frac{\partial c_{(\mathrm{O_2})}}{\partial r}\right|_{r=R_o}, \tag{14}$$

$$w_r^{a-o} = -\frac{R_o}{R_i}\frac{1}{c_{(\mathrm{Ti})}} D_{(\mathrm{O_2},\mathrm{TiO_2})} \left.\frac{\partial c_{(\mathrm{O_2})}}{\partial r}\right|_{r=R_o} (1-\gamma), \tag{15}$$

where R_i and R_o are the positions of the air-oxide and metal-oxide interface, respectively. In addition, one should note that w_r^{a-o} and w_r^{m-o} represent the r component of their respective interface velocity component.

The same Finite Difference solution scheme used for the solid cylinder oxidation problem was used to obtain a numerical solution to eq. (12). As previously stated, the required model parameters are $D_{(\mathrm{O_2},\mathrm{TiO_2})}$, γ, c_0, $c_{(Ti)}$, as well as the initial inner radius of the hollow cylinder.

4.2 Evaluation of Material Parameters.

The methods used to obtain the required material parameters for the oxidation model described in section 4.1 are presented below. The oxidation rate constant, α, the diffusion coefficient of O_2 through TiO_2, $D_{(\mathrm{O_2},\mathrm{TiO_2})}$, and the Pilling-Bedworth ratio, γ, are evaluated for a specified temperature, using one-dimensional planar (flat) experimental data of oxide thickness as a function of time. In addition, an alternative approach is presented to compute α from weight-gain information.

4.2.1 Experimental Measurement of α

The parabolic rate constant, α, given in eq. (6) is directly estimated from experimentally obtained oxide thickness measurements. The approach used herein is an application of the Least Squares method. By substituting eq. (6) into the Least Squares residual equation and minimizing with respect to α leads to the expression

$$\alpha = \frac{\sum_{i=1}^{n} h_i \sqrt{t_i}}{\sum_{i=1}^{n} t_i}, \tag{16}$$

where n is the total number of data points used to calculate α and h_i are the measured values of the oxide layer thickness at time t_i.

As discussed earlier, the one-dimensional planar oxidation behavior was shown to transition from a parabolic rate law to linear growth at 48 hours. Since the oxidation model considered herein assumes parabolic scale growth, the remainder of the analysis is limited to the use of data up to and including 48 hours. Therefore, evaluating eq. (16) using the oxide thickness data given in Fig. 10 results in a value of α equal to $0.01949 \mu m / \sqrt{\sec}$ with R equal to 0.997. As may be seen in Fig. 15, this value of α provides a computed oxide thickness that correlates well with experimental observations.

An alternative approach for estimating α is to use weight-gain per unit area data. For this case, the parabolic rate law is written in terms of weight-gain information such that

$$\frac{\Delta m}{A} = \beta \sqrt{t}, \tag{17}$$

where Δm represents the mass of oxygen added to the specimen, which is exclusively used for oxide formation and A is the total surface area, as previously defined. Substituting eq. (17) into the Least Squares residual and minimizing with respect to β leads to an expression similar to eq. (16) for the evaluation of β.

Equation (17) requires that the mass of oxygen used to form the oxide scale be known. However, for this investigation, only the total weight-gain (*i.e.*, the difference in measured weights of an unoxidized and oxidized specimen) was measured. Since the total weight-gain represents both dissolution of oxygen into the metal and oxide formation, an estimate of the percentage distribution of oxygen between the metal core and the scale was made using the work of Jenkins[5]. In his investigation, it was shown that the percentage of oxygen going into the metal core and the oxide scale is a function of time. However, the largest variation occurs during the initial stages of oxidation (<10 hours at 900°C), after which the percentage going into dissolution slowly decreases with time while the percentage used for scale formation gradually increases with time. Since the present evaluation encompassed a relatively short oxidation period (< 48 hours), it was assumed that the percent of oxygen going into dissolution would remain constant. Jenkins[5], obtained the scale and metal oxygen weight-gain by first measuring the total weight-gain of a specimen and then removed the oxide scale and measured the oxygen weight-gain to the metal alone. Based upon his measurements at 700°C, it was estimated for this investigation that for any time less than 48 hours, 70% of the total weight-gain represents oxygen weight-gain for scale formation. Thus, using the appropriate weight-gain data shown in Fig. 9 and accounting for the oxygen dissolution yields a β value of $0.003185 mg/(cm^2\sqrt{\text{sec}})$.

To relate weight-gain data to oxide thickness, one can write $\alpha \propto K\beta$, where the proportionality constant, K, is simply

$$K = \frac{V_{TiO_2}}{\Delta m}. \tag{18}$$

If the oxide scale is assumed to be stoichiometric and Δm is the mass of O_2 added to form the oxide layer, then for a given volume of TiO_2, V_{TiO_2}, having constant density, ρ_{TiO_2}, Δm can be computed by

$$\Delta m = V_{TiO_2}\rho_{TiO_2}\frac{M_{O_2}}{M_{TiO_2}}, \tag{19}$$

where M_{O_2} and M_{TiO_2} represent the molecular weight of O_2 and TiO_2, respectively. Hence, eq. (18) can be rewritten as

$$K = \frac{V_{TiO_2}}{V_{TiO_2}\rho_{TiO_2}}\frac{M_{TiO_2}}{M_{O_2}} \tag{20}$$

and eq. (6) becomes

$$h(t) = \frac{1}{\rho_{TiO_2}}\frac{M_{TiO_2}}{M_{O_2}}\beta\sqrt{t}. \tag{21}$$

For this investigation, ρ_{TiO_2} was taken to be $4.24 g/cm^3$ [25] and the molecular weight of O_2 and TiO_2 is $31.9988 g/mole$ and $79.8788 g/mole$, respectively. Therefore, the value of $K\beta$ obtained from this evaluation is $0.01875 \mu m/\sqrt{\sec}$, which is 3.8% lower than the value of α computed directly from oxide thickness measurements. One potential reason for the small discrepancy is that the actual density of the TiO_2 formed during oxidation may be lower than is typically reported in handbooks because of its porosity.

For example, Jenkins[5] reported a measured density of TiO_2 formed during oxidation of C.P. titanium at 850°C that was 9.9% lower than is generally found in the literature. In addition, while using the stoichiometric oxide assumption is a reasonable approach to this problem, in the preceding discussion it was pointed out that the rutile formed is actually an oxygen deficit structure. Figure 15 compares the evaluation of the rate constants using both oxide thickness and weight gain data. Since both methods provide nearly identical results, one can conclude that either method is viable for estimating $D_{(O_2,TiO_2)}$.

4.2.2 Experimental Measurement of γ.

Pilling and Bedworth[26] stated that the volume of oxide formed during oxidation will generally be different from the volume of reactant material consumed. Defining the aforementioned statement in terms of mass properties leads to the Pilling-Bedworth ratio (γ^{Ref}), given as

$$\gamma^{Ref} \equiv \frac{M_{oxide}\rho_{metal}}{\rho_{oxide}M_{metal}}. \tag{22}$$

Of particular interest in this research is how the theoretical value given by eq. (22) compares to an experimentally obtained value for TiO_2 formed on flat and curved surfaces of C.P. titanium. If the experimentally obtained value is greater than that given by eq. (22), then one would expect the oxide scale to be porous. Conversely, if the measured value is less than or equal to the theoretical value, the oxide is expected to be compact.

Equation (22) may also be written as the ratio of the volume of oxide produced per volume of metal consumed in the reaction, such that

$$\gamma = \frac{V_{oxide}}{V_{metal\ consumed}}. \tag{23}$$

Therefore, planar SEM images of pre and post oxidized specimen configurations can be used to estimate values of γ. In this investigation, two different specimen geometries were employed to evaluate γ as a function of time.

For the one-dimensional planar specimen configuration, eq. (23) can be expressed as

$$\gamma = \frac{V_{oxide}}{V_{metal\ consumed}} = \frac{w \cdot d \cdot h_{oxide}(t_i)}{w \cdot d \cdot (h_{metal}(t_0) - h_{metal}(t_i))}, \tag{24}$$

where $(w \cdot d)$ is the surface area perpendicular to the plane of oxide growth, as shown in Fig. 16. If $(w \cdot d)$ is assumed constant for a given volume of material, then eq. (24) can be reduced to

$$\gamma = \frac{h_{oxide(t_i)}}{h_{metal(t_0)} - h_{metal(t_i)}}. \tag{25}$$

The difficulty encountered when using the flat specimen configuration was the positioning of the pre-oxidized geometry relative to the post-oxidized specimen in order to determine the amount of metal consumed during the reaction. The flat specimens used in this investigation were thick with respect to the oxide layer thickness. Therefore, a series of V-grooves were broached in each specimen that enabled one to uniquely locate the unoxidized surface relative to the oxidized surface (that is, place a material point on the specimen that would correctly position the pre and post oxidized micrographs.

The graphical procedure employed in this investigation was to determine the intersection point of the two lines formed by bisecting the corner angles as shown in Fig.

16. Since the geometry requires the intersection point to be at the same location before and after oxidation, once the point was known, one simply had to align the pre and post oxidized micrographs in order to determine the appropriate values of h.

For the solid cylinder specimen configuration, eq. (23) can be expressed as

$$\gamma = \frac{V_{oxide}}{V_{metal\ consumed}} = \frac{l \cdot A_{oxide}(t_i)}{l \cdot (A_{metal}(t_0) - A_{metal}(t_i))}, \tag{26}$$

where l is the length perpendicular to the plane of oxide growth, as shown in Fig. 17. If l is assumed constant for a given volume of material, then eq. (26) can be reduced to

$$\gamma = \frac{A_{oxide(t_i)}}{A_{metal(t_0)} - A_{metal(t_i)}}. \tag{27}$$

Unlike the flat specimen configuration, the cylindrical specimens required no special preparation in order to superimpose the pre and post oxidized geometries. By processing the respective SEM images, as shown in Fig. 17, one could directly measure the required areas.

The resulting γ calculations for one-dimensional planar specimens and cylindrical specimens are presented in Fig. 18. The values of γ for the one-dimensional planar specimens were obtained using eq. (25) and can be seen to slowly decrease with time. On the other hand, the cylindrical specimens produced values of γ (from eq. (27)) that increase with time as was expected due to the increasing void formation with time. As can also be seen, these values differ slightly from the theoretical value of 1.766 ($\rho_{Ti} = 4.51 g/cm^3$, $\rho_{TiO_2} = 4.24 g/cm^3$ and $M_{Ti} = 47.88 g/mole$, $M_{TiO_2} = 79.8788 g/mole$), which can be computed directly from eq. (22). The variation in γ, between the flat and cylindrical specimens, can be attributed to the influence of porosity and stress in the

oxide. The average value of γ was found to be 1.779. However, the average value is less than 1% larger than the value computed using standard reference densities. This appears to be in contradiction to the level of observed porosity in the oxide scale. This suggests that either oxide expansion is restricted by the stress state in the scale or the lattice parameters of the oxygen deficit rutile structure are slightly different from the lattice parameters associated with the reference material.

4.2.3 Evaluation of $D_{(O_2,TiO_2)}$

The diffusion coefficient $D_{(O_2,TiO_2)}$ was evaluated using eq. (7) with the value of α taken to be $0.01949 \mu m/\sqrt{\sec}$ and the average γ taken as 1.779. The titanium concentration, c_{Ti}, was computed as the ratio of the density of titanium (measured to be $4.67 g/cm^3$) to its molecular weight and was calculated to be $97.598 kmole/m^3$. Since c_0 was not a measured parameter for this investigation, a value was obtained from the available literature. TiO_2 has been reported to have a small oxygen solubility range. Hurlen[27] cited a number of other researchers who have measured the extent of nonstoichiometry to be in the range of $TiO_{2-0.100}$ on the low side to an upper limit of stoichiometric TiO_2. Converting this to appropriate units, a value of c_0 was computed to be $2.4232 kmole/m^3$. It should be noted, however, that the value of c_0 may be different for the different specimen geometries, especially the hollow cylinders, where it is possible that oxygen at the air-oxide interface may not be replenished fast enough to reach the level required by the selected value of c_0. These parameters led to a $D_{(O_2,TiO_2)}$ of $0.44 \times 10^{-2} \mu m^2/\sec$. This compares favorably with the value of $2.91 \times 10^{-2} \mu m^2/\sec$

obtain by Unnam, *et al.*[14]. However, unless the diffusion coefficient is independently measured, its value is only as accurate as c_0. Since c_0 was not measured in this investigation, one can simply regard the value of $D_{(O_2,TiO_2)}$ obtain herein to be an estimate.

4.3 Results and Discussion

Numerical results obtained for the different oxidation problems discussed herein are presented below using parameters obtained from one-dimensional planar experiments. Figure 19 compares the predicted oxide thickness and the experimentally measured values for all solid and hollow cylinder geometries oxidized at 700°C. The model predictions can initially be seen to be nearly identical and it is not until a substantial amount of oxidation has occurred that the solutions begin to diverge from one another. However, the works of Lagoudas, *et al.*[18,21,24] have shown that the curvature associated with a cylindrical geometry measurably influences the oxidation behavior in comparison to one-dimensional planar oxidation. More specifically, a solid cylinder oxidizes at a faster rate due to a shrinking reaction surface, compared to a flat geometry and conversely, a hollow cylinder oxidizes slower as a result of the increased reaction surface area. The apparent initial insensitivity of the model to geometry shown in Fig. 19 is the result of two competing effects, curvature and volumetric expansion of the oxide[21]. Therefore, the predictions shown in Fig. 19 suggest that accounting for the effect of volumetric expansion of the oxide counteracts the curvature effect. For long exposures (for example see 240 hours) the model yields smaller oxide thickness values than were experimentally observed for both the solid cylinder and planar specimens. This is

explained by the fact that the model is only capable of predicting parabolic oxide growth and as discussed earlier, the oxidation behavior was shown to transition from parabolic to linear oxidation at or near 48 hours.

Figure 20 compares experimental data and model results for an oxidation exposure that coincides with the observed parabolic behavior (i.e., < 48 hours). As previously stated, the initial model simulation for planar oxidation and predictions for the cylindrical geometries coincide due to the competing influence of the oxide expansion and curvature effects. Given that data from one-dimensional planar oxidation have been used to calibrate the model, Fig. 20 shows that the model generally under predicts the solid cylinder oxide growth, while results for the hollow cylinders are generally over predicted. One possible explanation for the discrepancy between the model predictions and experimental results is that the effective diffusion coefficients for both the solid and hollow cylinders are distinctly different from the one-dimension planar case. In Section 3 it was shown that the oxide developed on the solid cylinders was substantially more porous then the scale found on the hollow cylinders, based upon a comparison of the total number of observable voids. Therefore, one would expect the effective diffusion coefficient for the solid cylinders to be higher than was actually determined for the planar oxidation case and lower for the hollow cylinder geometries. Furthermore, in addition to the presence of voids, the difference in diffusion coefficients may also be the result of stresses that have developed in the oxide and/or metal at the metal-oxide interface.

5. Summary/Conclusions

The purpose of this investigation was to experimentally characterize the morphological evolution of TiO_2 scale on various multi-dimensional geometries of titanium that included solid and hollow cylinders, as well as external and internal wedges. Specimens were successfully fabricated to a size such that the thickness of the oxide scale formed during oxidation was of the same order of magnitude as the characteristic dimension of the specimen geometry. It was observed that scale growth on the inside surface of a hollow cylinder does not proceed as rapidly as the oxide development on the outer surface of a solid cylinder This is in agreement with previously report research regarding the effect of curvature.

The morphological aspects of scale development were also shown to be geometry dependent. The oxidation associated with the external wedges and solid cylinders appears to produce an oxide scale similar to that grown on a flat specimen. The scale had two readily observable structures: 1) at the air-oxide interface, the oxide appeared to be compact and its thickness grew with time and 2) from the metal-oxide interface up to the compact scale, the oxide appeared to have of a porous-layered arrangement with the pore size being a function of distance from the metal-oxide interface. Conversely, the oxide scale growth observed on the internal wedges and hollow cylinders, while still layered, appeared to be much less porous and had less damage due to cracking and spalling.

An oxidation model was presented that accounts for solid state diffusion of oxygen through a substrate using Fick's law, as well as expansion of the oxide scale. Three special cases of the model were presented that included a closed form solution the one-dimensional planar case, oxidation on the outer surface of a solid cylinder, and oxide growth on the insider surface of a hollow cylinder. Since the modeling initiative was

aimed at studying the effect of volumetric expansion of the oxide layer, dissolution of oxygen into the metal, while significant, was not included.

A procedure was described that made use of one-dimensional planar oxidation data to compute the necessary input constants to the model, including an effective diffusion coefficient and Pilling-Bedworth ratio, γ. As part of the procedure, it was also shown that oxide thickness could accurately be estimated from weight-gain data. Furthermore, a method was described to experimentally measure γ as a function of time. To this end, the model demonstrated the competing influences of oxide expansion and curvature effects. In addition, the model under predicted the oxide layer thickness on a solid cylinder, while it over predicted the oxide growth on the inner surface of a hollow cylinder. The reason for the inaccuracy has been accounted for by the fact that the scale morphology was actually found to be different from the one-dimensional planar oxide in terms of porosity resulting in different effective diffusion coefficients for the various geometries.

Acknowledgments – The authors wish to express appreciation for the support provided by AFOSR Grant No. F49620-97-1-0338. The authors also acknowledge Pavlin Entchev for his contributions with respect to the model, as well as his comments and discussions.

References

1. M. Donachie, *Titanium and Titanium Alloys: Source Book* (American Society for Metals, Metals Park OH, 1982).
2. E. Gulbransen and K. Andrew, *Transactions of the American Institute of Mining and Metallurgical engineers* **185**, 741-751 (1949).
3. M. Davies and C. Birchenall, *Journal of Metals* **3**, 877-880 (1951).
4. P. Morton and W. Baldwin, *Transactions of the American Society of Metals* **44**, 1004-1004 (1952).
5. A. Jenkins, *Journal of the Institute of Metals* **82**, 213-221 (1953).
6. A. Jenkins, *Journal of the Institute of Metals* **84**, 1-9 (1955).

7. G. Wallwork and A. Jenkins, *Journal of the Electrochemical Society* **106**, 10-14 (1959).
8. P. Kofstad, K. Hauffe, and H. Kjöllesdal, *Acta Chemica Scandinavica* **12**, 239-266 (1958).
9. P. Kofstad, P. Anderson, and O. Krudtaa, *Journal of the Less-Common Metals* **3**, 89-97. (1961).
10. P. Kofstad, *High-Temperature Oxidation of Metals* (John Wiley & Sons Inc., New York, 1966).
11. J. Stringer, *Acta Metallurgica* **8**, 758-766 (1960).
12. J. Stringer, *Journal of the Less-Common Metals* **6**, 207-213 (1964).
13. M. Déchamps, R. Feldman, and P. Lehr, in *Titanium and Titanium Alloys*; *Vol. 2*, edited by J. Williams and A. Belov (Plenum Press, New York, 1976), 1045-1056.
14. J. Unnam, R. Shenoy, and R. Clark, *Oxidation of Metals* **26**, 231-252 (1986).
15. J. Lopes-Gomes and A. Huntz, *Oxidation of Metals* **14**, 249-261 (1980).
16. S. Andersson, B. Collén, U. Kuylenstierna, and A. Magnéli, *Acta Chemica Scandinavica* **11**, 1641-1652 (1957).
17. G. Bertrand, K. Jarraya, and J. Chaix, *Oxidation of Metals* **21**, 1-19 (1983).
18. D. Lagoudas and Z. Ding, *International Journal of Engineering Science* **36**, 367-381 (1998).
19. M. Castelli and J. Gayda, *Reliability Stress Analysis and Fatigue Prevention DE-55 ASME*, 213-221 (1993).
20. J. Gyda and T. Gabb, *International Journal of Fatigue*, 14-20 (1992).
21. P. Entchev, D. Lagoudas, and J. Slattery, *International Journal of Engineering Science (Submitted)* (1999).
22. C. Coddet, J. Chretien, and G. Bèranger, in *Titanium and Titanium Alloys*; *Vol. 2*, edited by J. Williams and A. Belov (Plenum Press, New York, 1976), 1097-1105.
23. H. Rode, D. Orlicki, and V. Hlavacek, *AIChE Journal* **41**, 1235-1250 (1995).
24. D. Lagoudas, X. Ma, D. Miller, and D. Allen, *International Journal of Engineering Science* **33**, 2327-2343 (1995).
25. G. Samsonov, *The Oxide Handbook*, 2nd ed. (Plenum Publishing Corp., New York, 1982).
26. N. Pilling and R. Bedworth, *The Journal of the Institute of Metals* **29**, 525-591 (1923).
27. T. Hurlen, *Acta Chemica Scandinavica* **13**, 365-376 (1959).
28. E.A. Garcia, *Met. Corros. Ind.* **638**, 319 (1978).
29. Vaquila, I., Passeggi Jr, M., and Ferrón, J., *Applied Surface Science*, vol. 93, 247, 1996.
30. Y. Mizuno, A. Tanaka, Y. Takakuwa, F. Ishida, K. Takahiro, H. Tonda, K. Ishikawa, T. Takano, T. Ikeuchi, T. Okada, S. Yamaguchi and T. Homma, *Materials at High Temperatures* **17**, 13-21 (2000).

List of Tables

List of Figures

Table 1.

	Length (cm)			Diameter (cm)			Angles		
	L	W	z	D_1	D_2	D_3	α_1	α_2	α_3
Flat	1.1	0.90	0.065						
Solid Cylinders	3.3			0.0050	0.0125	0.0250			
Hollow Cylinders	1.0	0.50	0.065	0.0130	0.0267	0.0343			
External Wedge	1.0	0.50	0.065				30°	60°	90°
Internal Wedge	1.0	0.50	0.065				30°	60°	90°

Table 2.

	Oxidation Time (hours)						
	6	12	24	36	48	72	240
Flat	4	4	4		4	4	4
Solid Cylinders							
50μm Diameter	1	1	1		1	1	1
125μm Diameter	1	1	1		1	1	1
250μm Diameter	1	1	1		1	1	1
Hollow Cylinders							
130μm Diameter	1	1	1	1	1	1	
267μm Diameter	1	1	1	1	1	1	
343μm Diameter	1	1	1	1	1	1	
External Wedge							
30°	1	1	1		1	1	1
60°	1	1	1		1	1	1
90°	1	1	1		1	1	1
Internal Wedge							
60°	1	1	1	1	1	1	
90°	1	1	1	1	1	1	

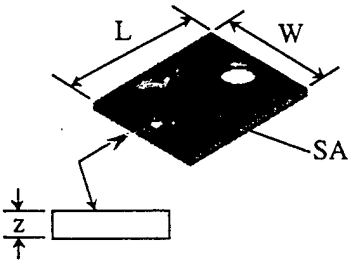

a) Flat specimen configuration

Cylinderical Specimens

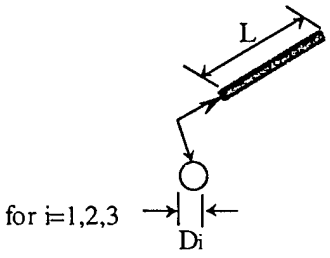

b) Solid cylinder specimen configuration

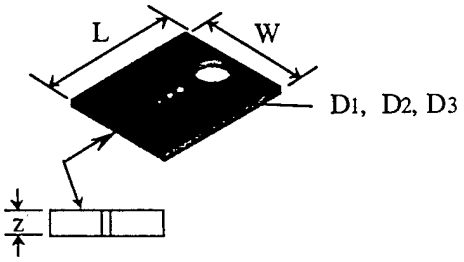

c) Hollow cylinder specimen configuration

Wedge Specimens

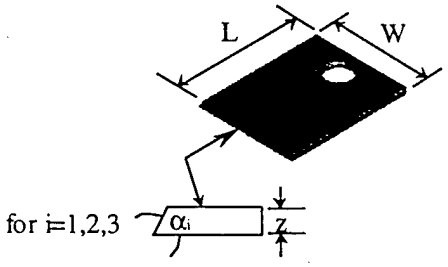

d) External wedge specimen configuration

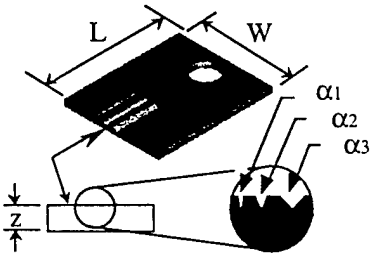

d) Internal wedge specimen configuration

Fig. 1.

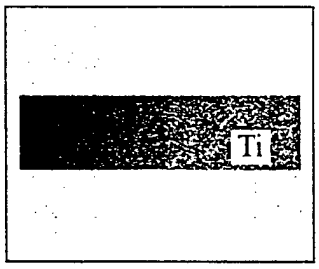

a) Flat specimen (approximate thickness is 6,500μm)

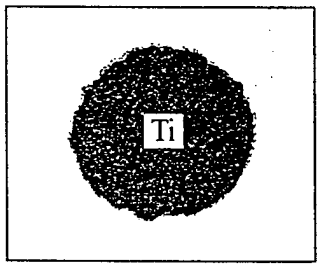

b) Solid cylinder specimen (50μm diameter)

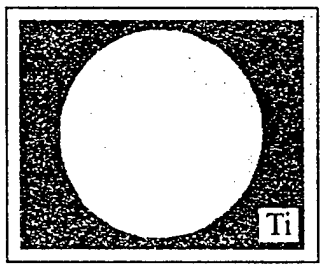

c) Hollow cylinder specimen (130mm diameter)

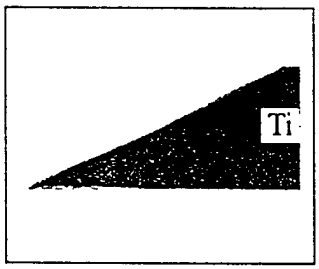

d) External wedge specimen (30 angle, height 6,500μm)

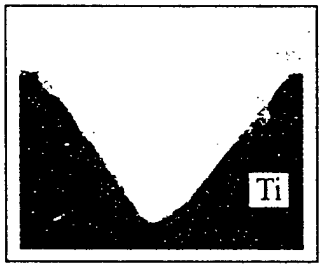

e) Internal wedge specimen (60 angle, height of 90μm)

Fig. 2.

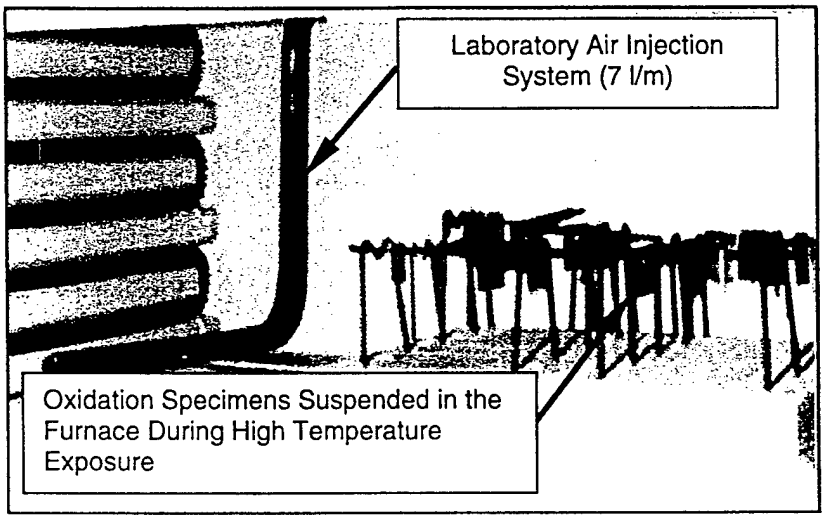
Laboratory Air Injection System (7 l/m)
Oxidation Specimens Suspended in the Furnace During High Temperature Exposure

Fig. 3.

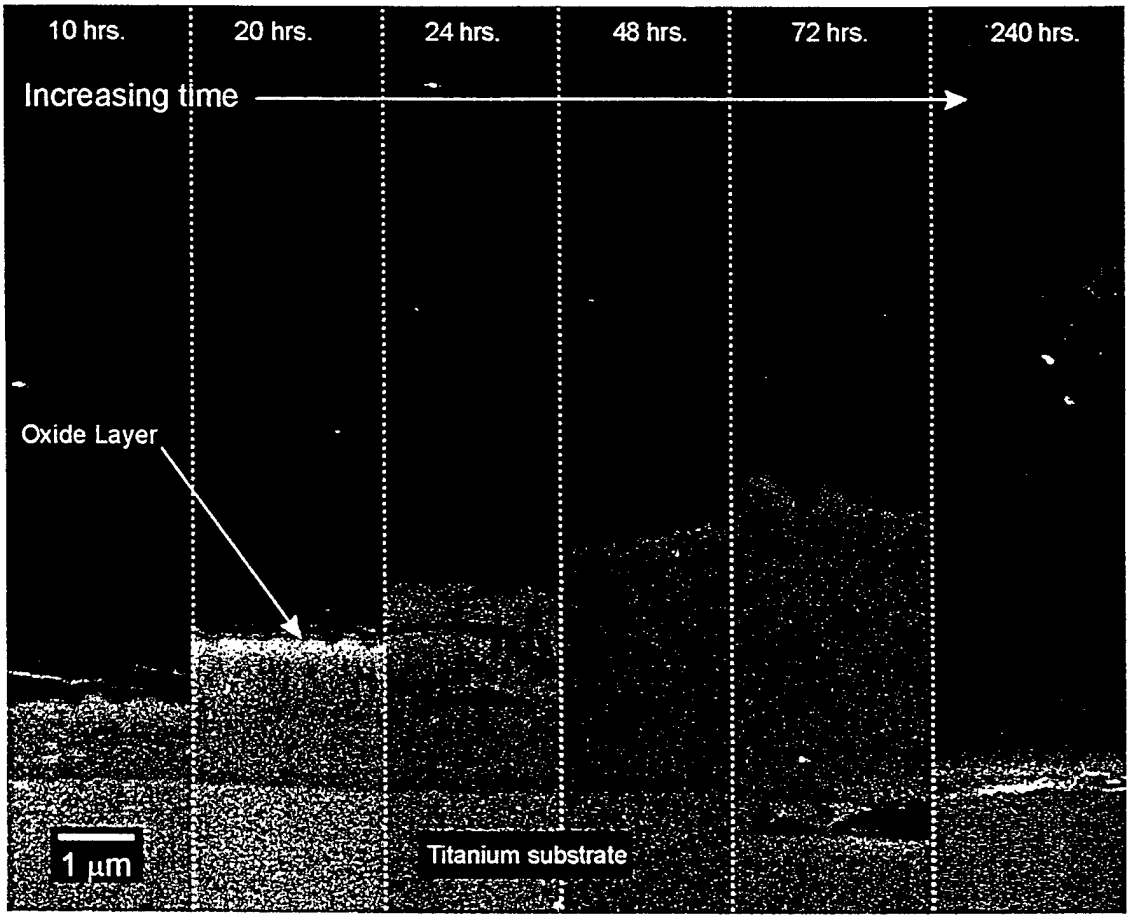
10 hrs.
20 hrs.
24 hrs.
48 hrs.
72 hrs.
240 hrs.
Increasing time
Oxide Layer
1 μm
Titanium substrate

Fig. 4.

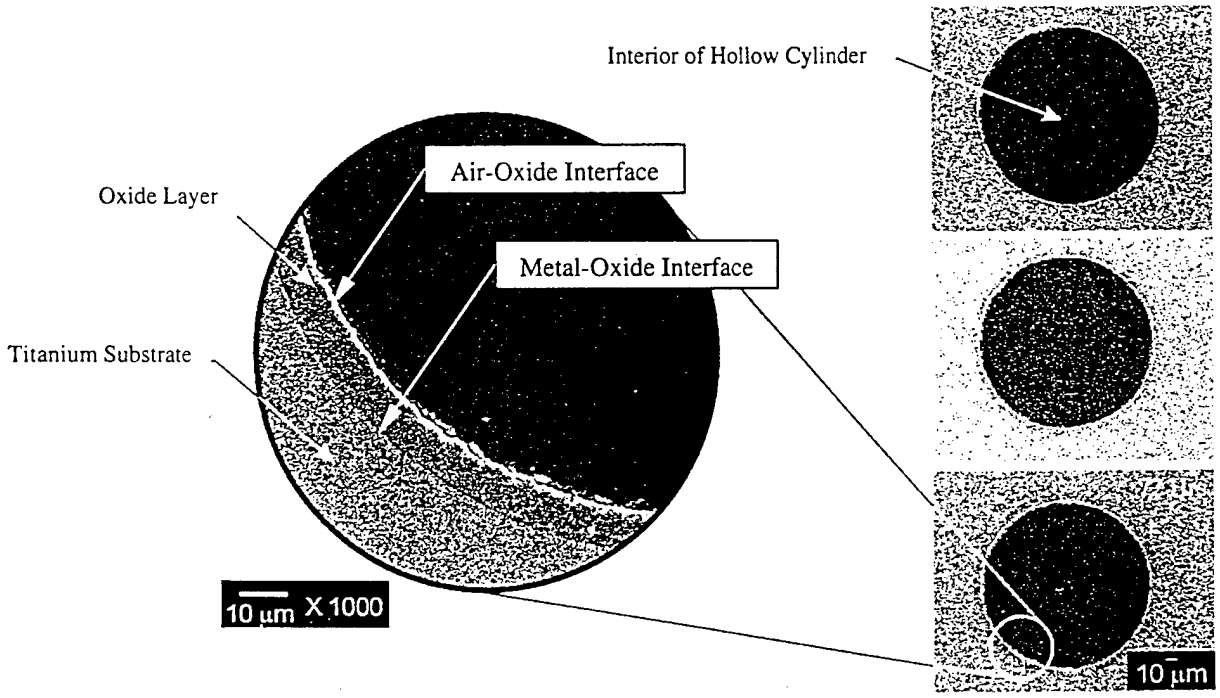
Interior of Hollow Cylinder
Air-Oxide Interface
Oxide Layer
Metal-Oxide Interface
Titanium Substrate
10 µm X 1000
10 µm

Fig. 5.

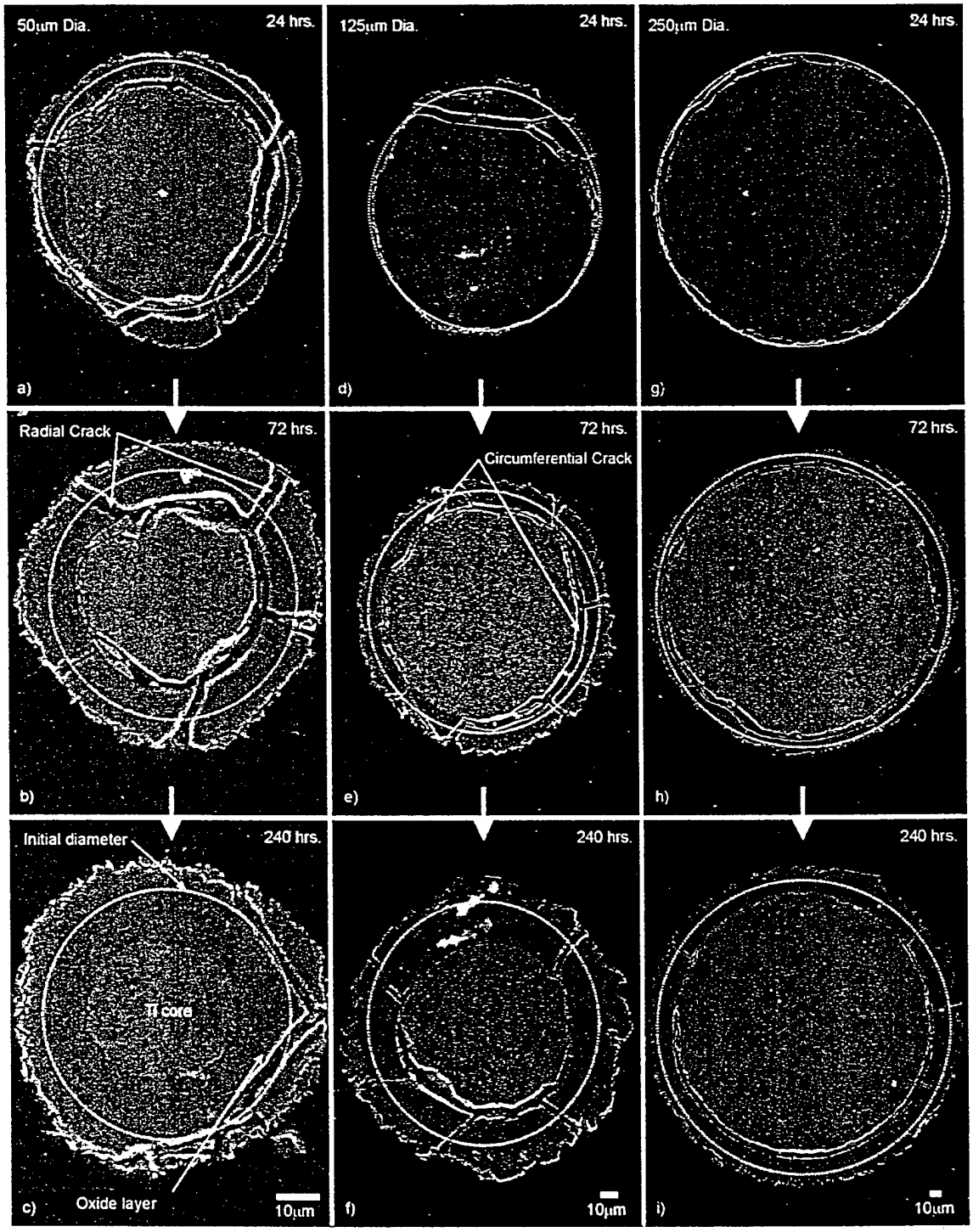
50μm Dia.
24 hrs.
125μm Dia.
24 hrs.
250μm Dia.
24 hrs.
a)
d)
g)
Radial Crack
72 hrs.
72 hrs.
Circumferential Crack
72 hrs.
b)
e)
h)
Initial diameter
240 hrs.
240 hrs.
240 hrs.
Ti core
c)
Oxide layer
10μm
f)
10μm
i)
10μm

Fig. 6.

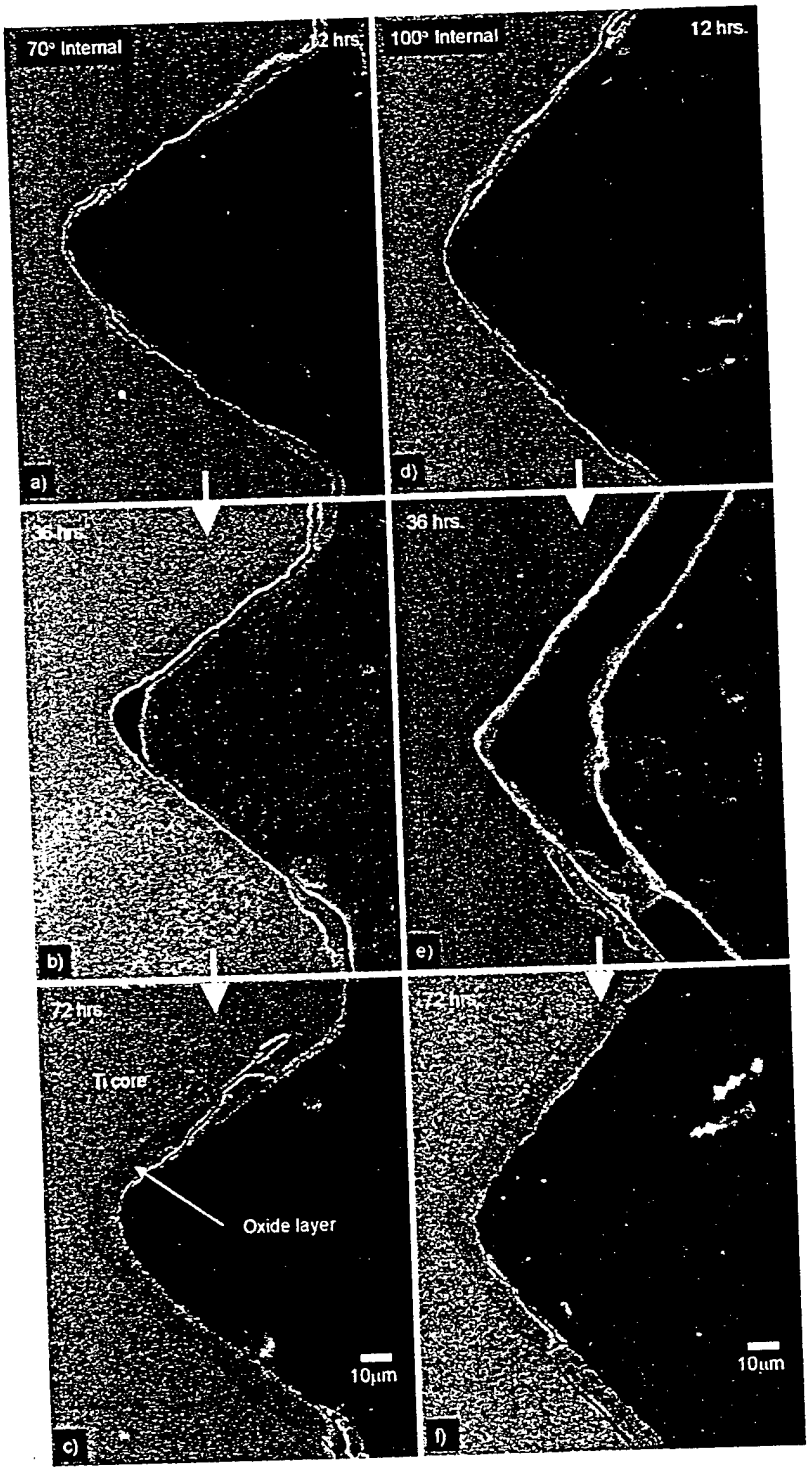
70° Internal
12 hrs.
100° Internal
12 hrs.
a)
d)
36 hrs.
b)
e)
72 hrs.
Ti core
Oxide layer
10μm
c)
10μm
f)

Fig. 7.

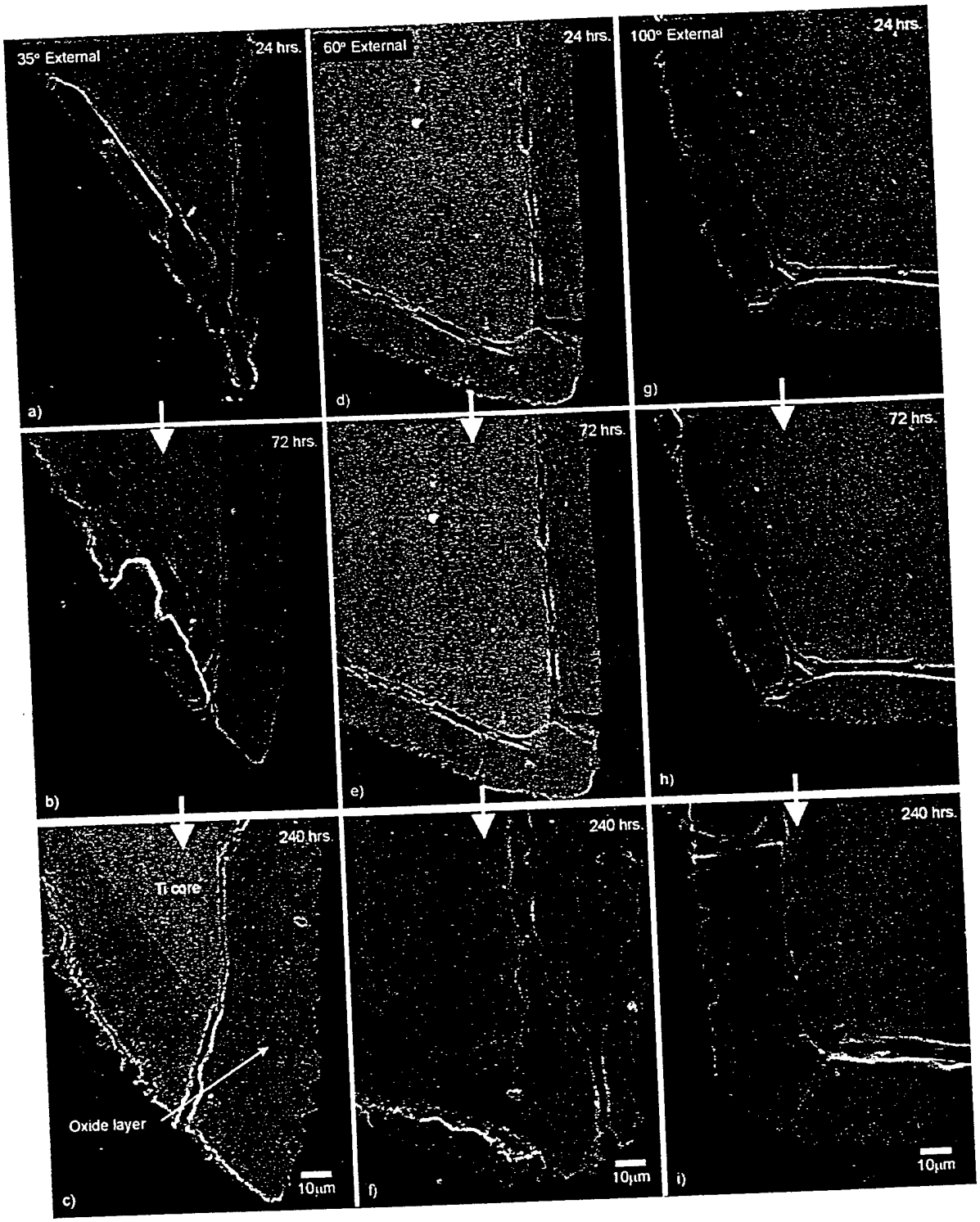
35° External
24 hrs.
60° External
24 hrs.
100° External
24 hrs.
a)
d)
g)
72 hrs.
72 hrs.
72 hrs.
b)
e)
h)
240 hrs.
240 hrs.
240 hrs.
Ti core
Oxide layer
10μm
10μm
10μm
c)
f)
i)

Fig. 8.

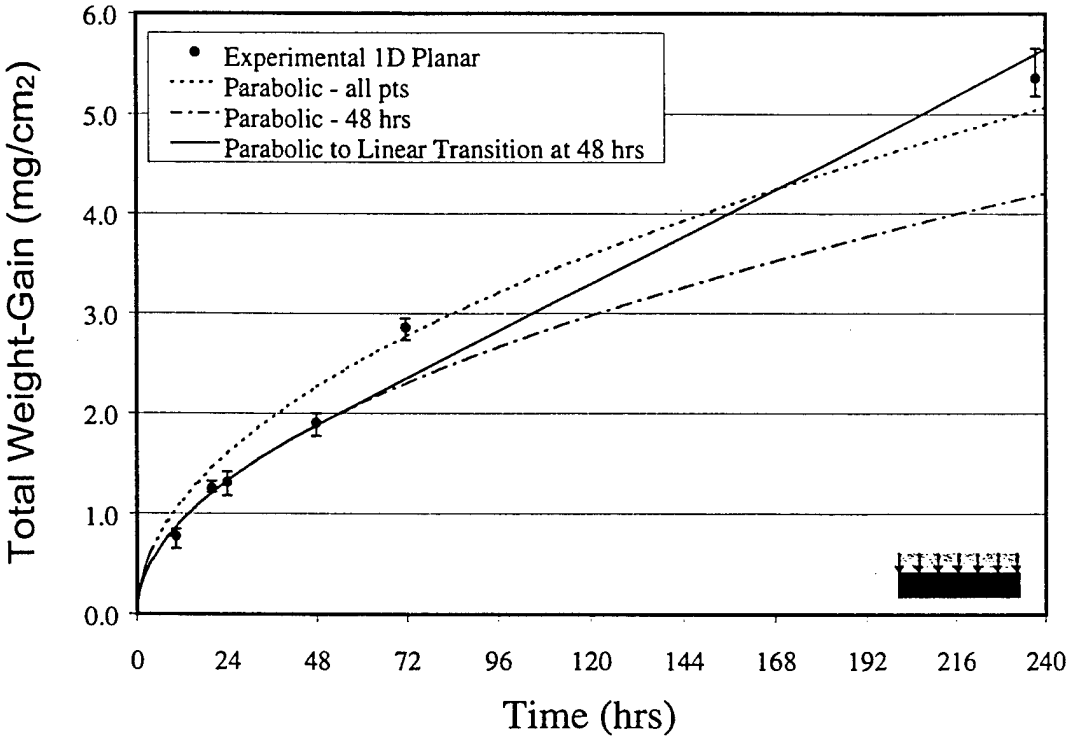
Experimental 1D Planar
Parabolic - all pts
Parabolic - 48 hrs
Parabolic to Linear Transition at 48 hrs
Total Weight-Gain (mg/cm2)
6.0
5.0
4.0
3.0
2.0
1.0
0.0
0
24
48
72
96
120
144
168
192
216
240
Time (hrs)

Fig. 9.

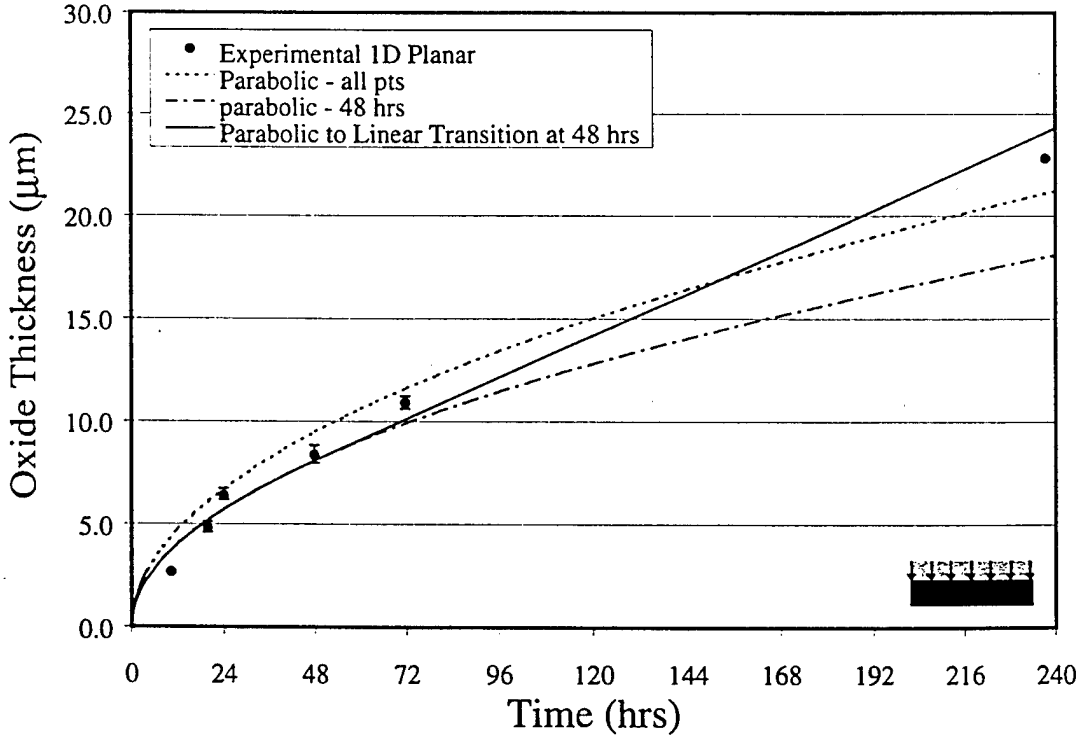
Experimental 1D Planar
Parabolic - all pts
parabolic - 48 hrs
Parabolic to Linear Transition at 48 hrs
Oxide Thickness (μm)
30.0
25.0
20.0
15.0
10.0
5.0
0.0
0
24
48
72
96
120
144
168
192
216
240
Time (hrs)

Fig. 10.

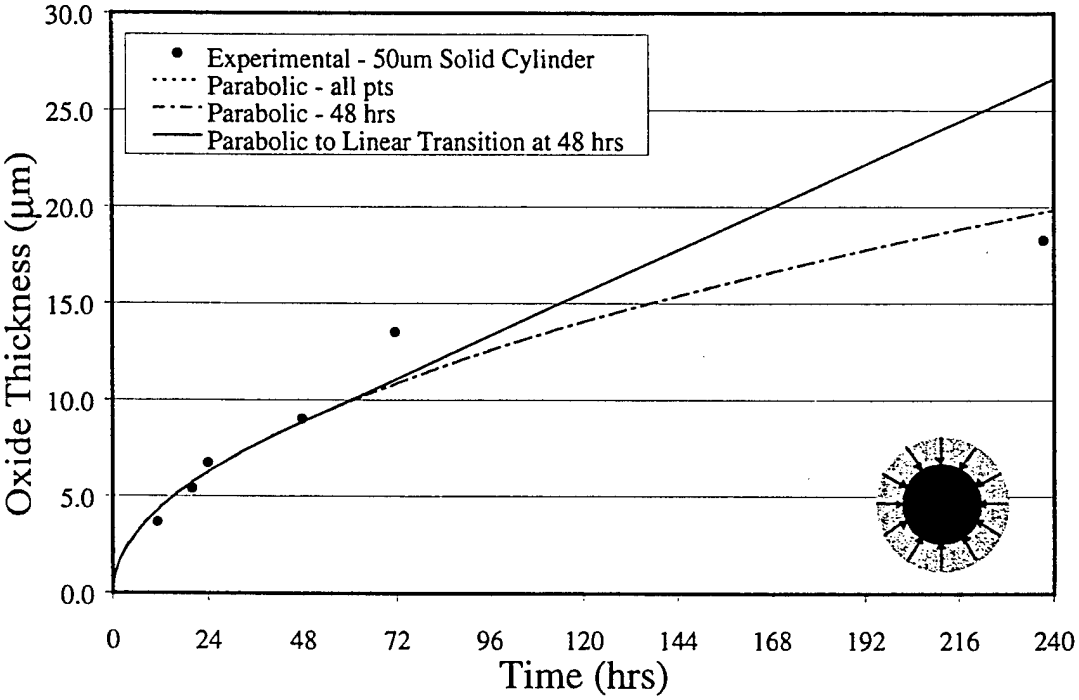

Fig. 11a.

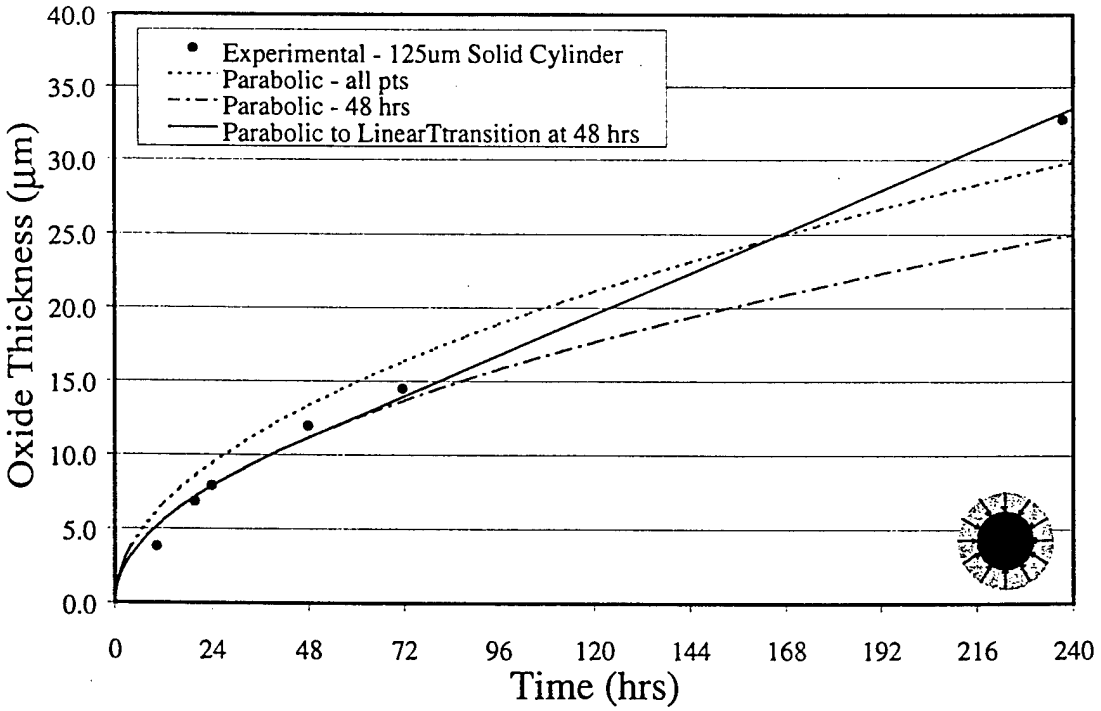

Fig. 11b.

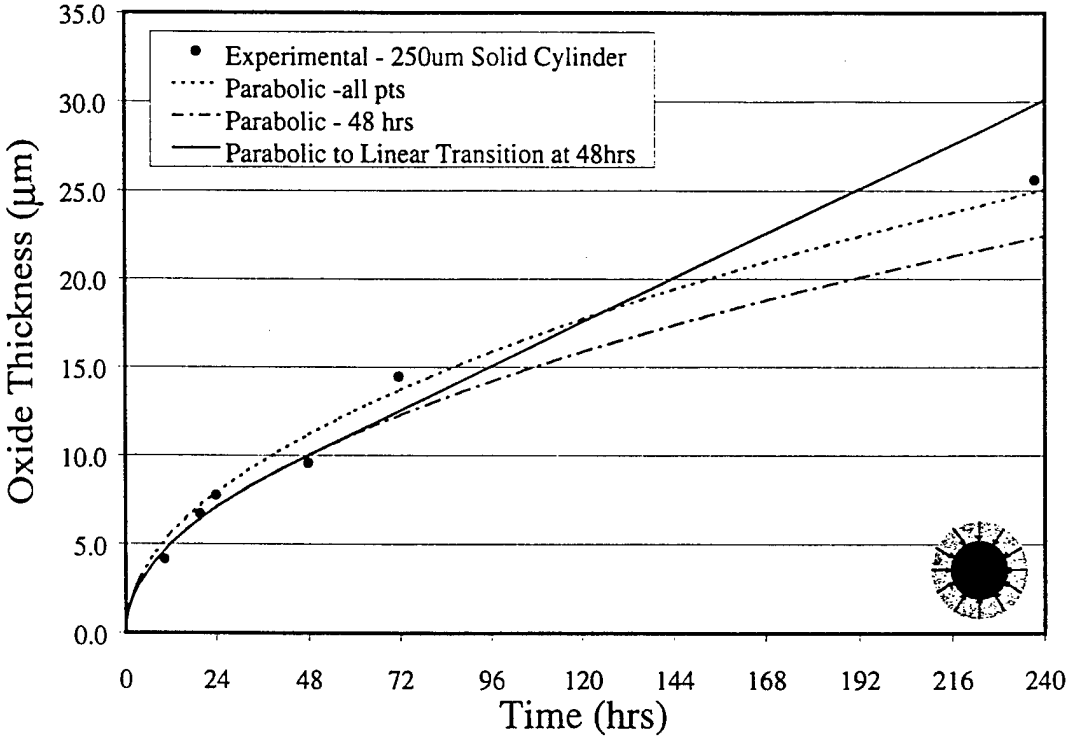

Fig. 11c.

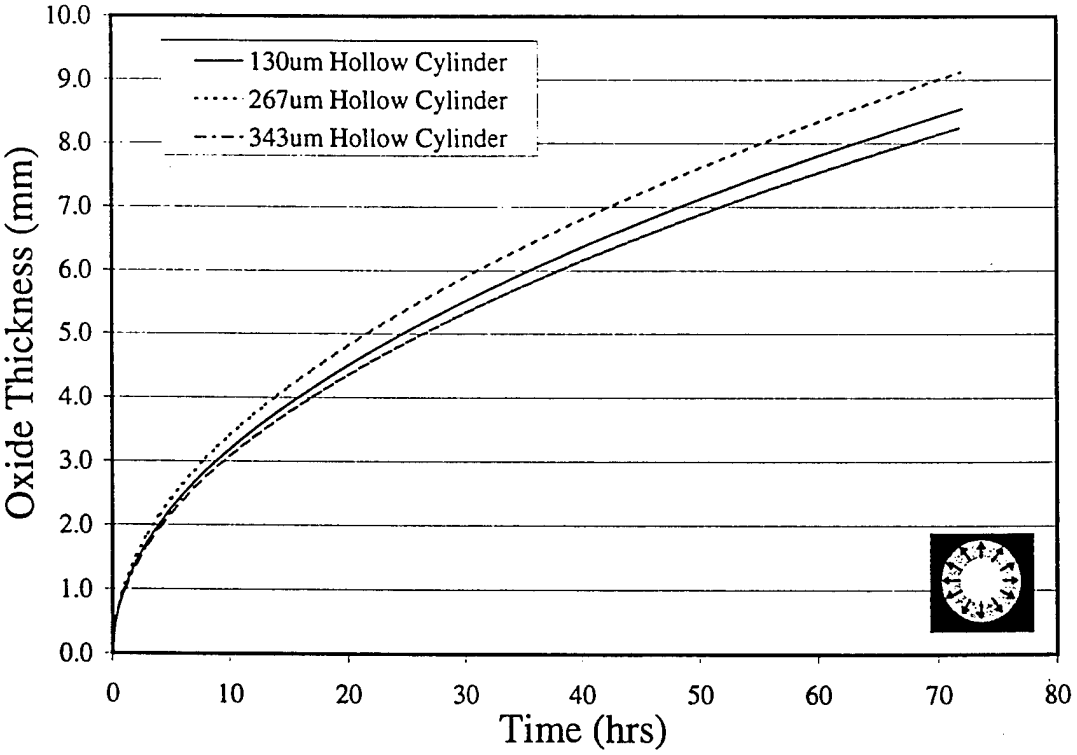

Fig. 12.

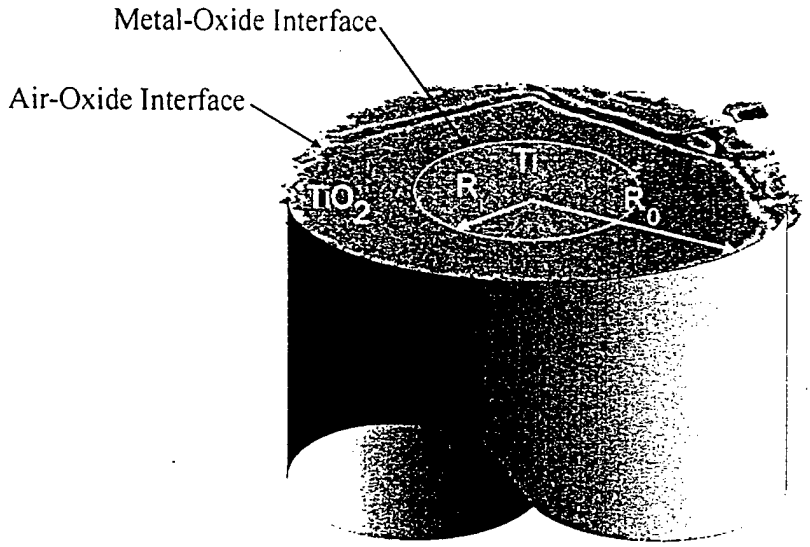

Fig. 13.

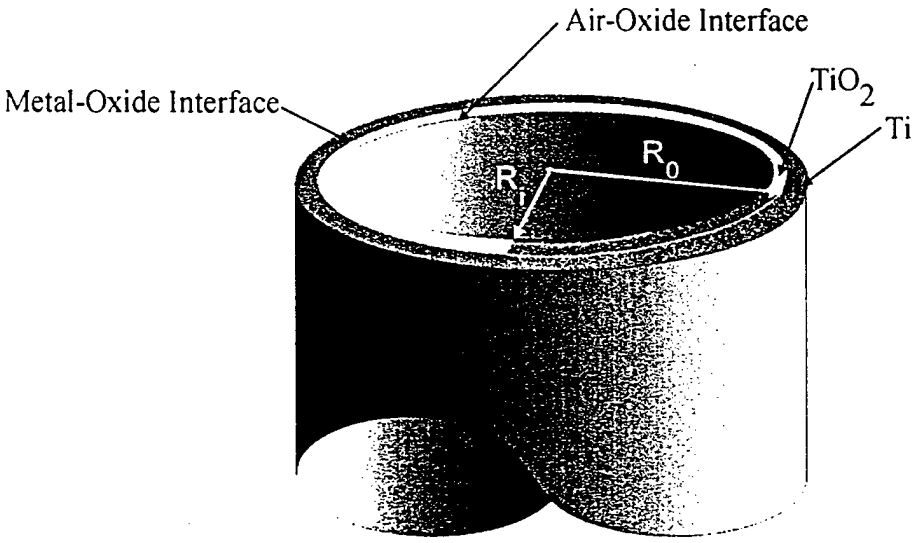

Fig. 14.

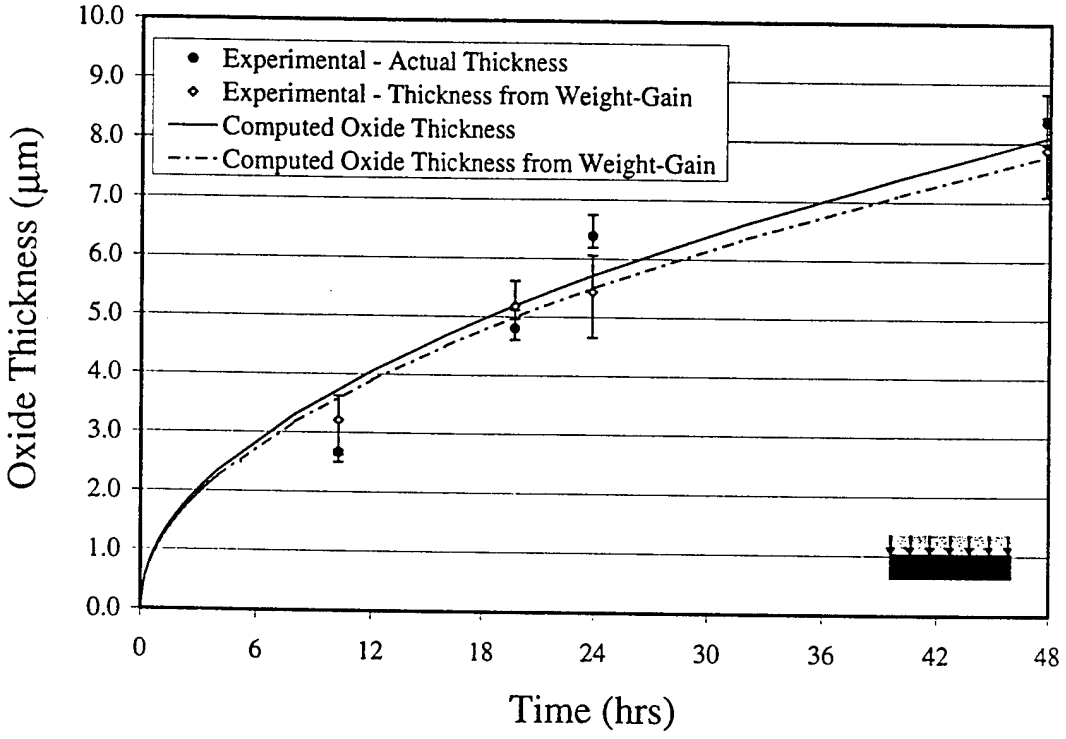
Experimental - Actual Thickness
Experimental - Thickness from Weight-Gain
Computed Oxide Thickness
Computed Oxide Thickness from Weight-Gain
Oxide Thickness (μm)
10.0
9.0
8.0
7.0
6.0
5.0
4.0
3.0
2.0
1.0
0.0
0
6
12
18
24
30
36
42
48
Time (hrs)

Fig. 15.

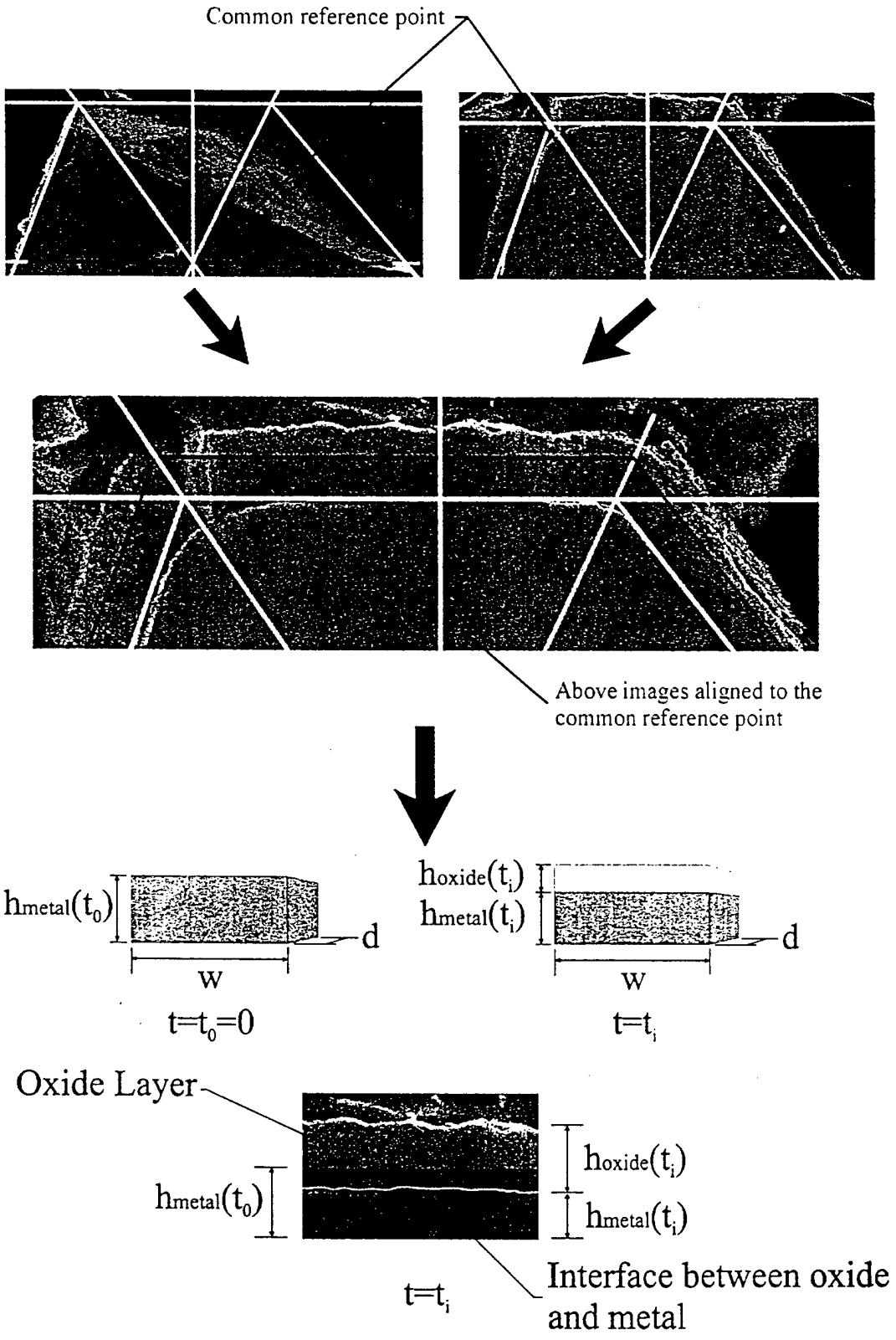
Common reference point
Above images aligned to the common reference point
$h_{metal}(t_0)$
d
w
$t=t_0=0$
$h_{oxide}(t_i)$
$h_{metal}(t_i)$
d
w
$t=t_i$
Oxide Layer
$h_{metal}(t_0)$
$h_{oxide}(t_i)$
$h_{metal}(t_i)$
$t=t_i$
Interface between oxide and metal

Fig. 16.

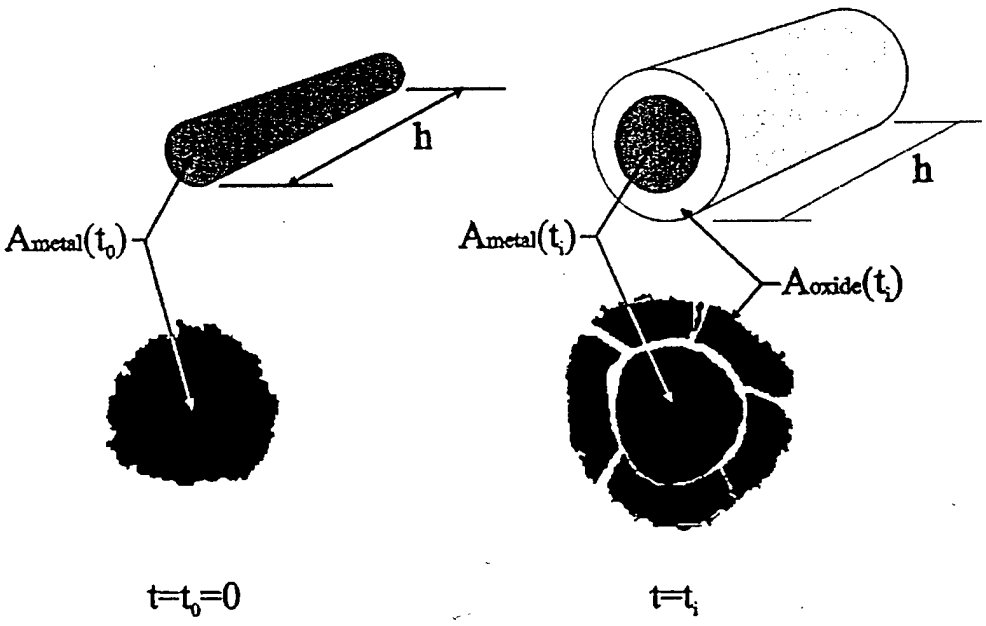

Fig. 17.

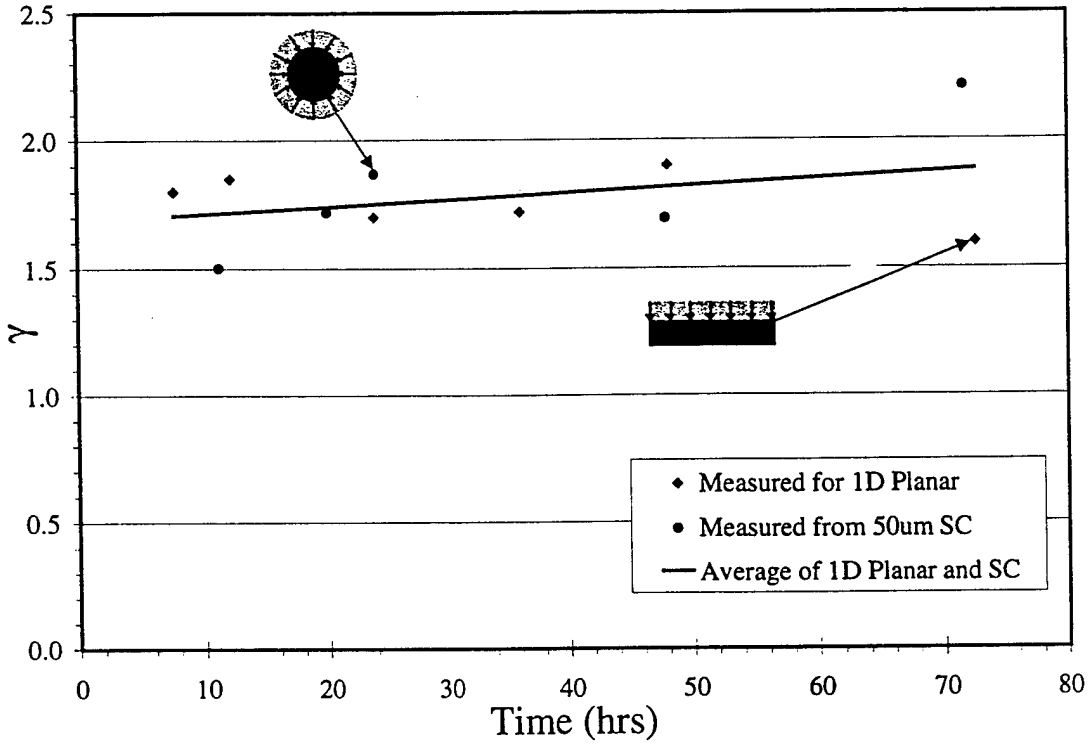
2.5
2.0
1.5
1.0
0.5
0.0
γ
0
10
20
30
40
50
60
70
80
Time (hrs)
Measured for 1D Planar
Measured from 50um SC
Average of 1D Planar and SC

Fig. 18.

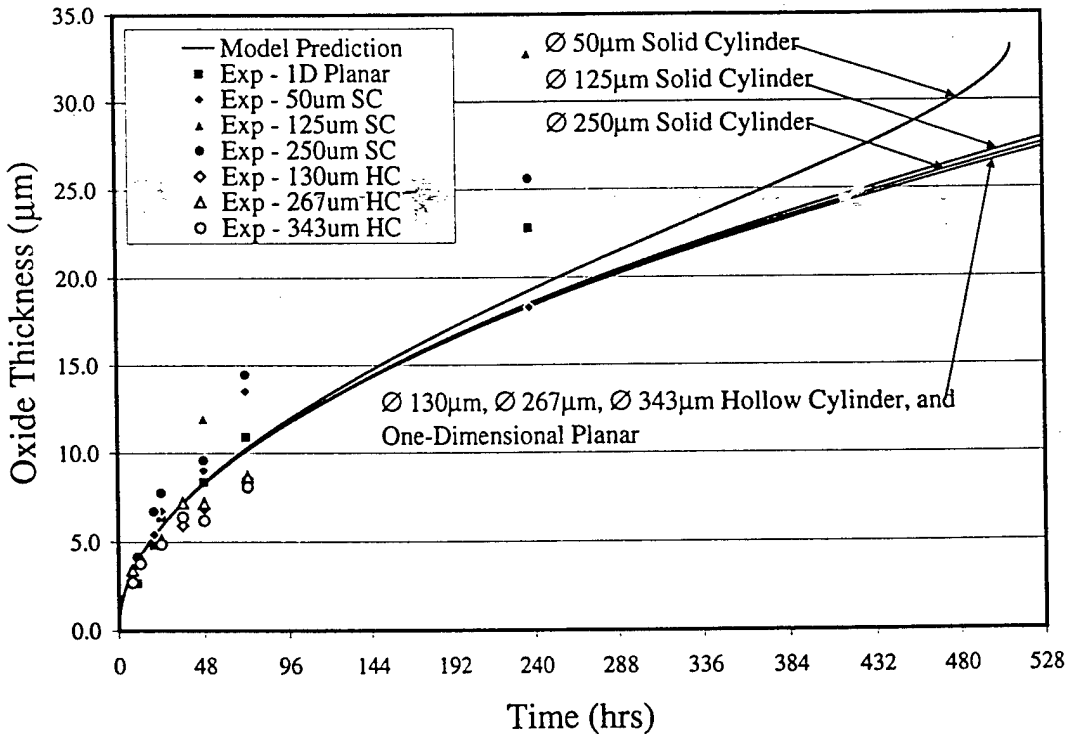
35.0
30.0
25.0
20.0
15.0
10.0
5.0
0.0
Oxide Thickness (μm)
0
48
96
144
192
240
288
336
384
432
480
528
Time (hrs)
Model Prediction
Exp - 1D Planar
Exp - 50um SC
Exp - 125um SC
Exp - 250um SC
Exp - 130um HC
Exp - 267um HC
Exp - 343um HC
Ø 50μm Solid Cylinder
Ø 125μm Solid Cylinder
Ø 250μm Solid Cylinder
Ø 130μm, Ø 267μm, Ø 343μm Hollow Cylinder, and
One-Dimensional Planar

Fig. 19.

PREDICTION OF DAMAGE EVOLUTION IN LAMINATED COMPOSITES SUBJECTED TO IMPACT LOADING

D.H. Allen
and
C. R. Searcy

Aerospace Engineering Department
Texas A&M University
College Station, TX 77843-3141

Abstract

A model for predicting crack growth in viscoelastic media is developed herein. The model proceeds from the assumption that it is appropriate to utilize a nonconvex cohesive zone model ahead of the crack tip. Due to the nonconvexity nature of the cohesive zone, crack propagation is accommodated naturally as a transition from contiguous material to traction free internal boundaries.

The cohesive zone model is developed by considering a representative volume element in a cohesive zone, and solving this micromechanical boundary value problem analytically. The solution to this problem is then homogenized to produce a traction-displacement that is both history dependent and a function of a damage parameter that is an internal state variable. The resulting model produces a critical energy rate that is both rate and history dependent. Example problems are presented to demonstrate the efficacy of the model.

Introduction

Fracture in elastic media has been via numerous experimental projects over the last thirty years to be accurately modelled by deploying the concept of a critical energy release, G_c, that is a material constant. When this material property is exceeded, a crack is predicted to grow [1]. This concept has been utilized to great advantage, at least in part due to the discovery that the available energy for crack growth, G, is a path independent quantity [2-3], that can be measured quite easily experimentally.

Unfortunately, for the case of inelastic media, the so-called Griffith criterion, discussed above, has some inherent shortcomings. Since the available energy is no longer path independent in these media, it is difficult to measure this quantity experimentally. Furthermore, the critical energy release rate is not necessarily a material constant [4]. This history dependence has been modelled in a number of ways, such as constructing ad hoc curve fits for G_c. One way that has attracted interest recently is to extend the ideas originally proposed by Dugdale [4] and Barenblatt [5] to incorporate a cohesive zone ahead of the tip of the crack. This is especially

attractive for the case of viscoelastic media, wherein complex damage zones such as crazes and/or hackles often develop ahead of the crack tip [6].

While the early cohesive zone models included on way of accounting for rate or history dependence [5,6], recent developments of cohesive zone models have been more useful towards this end. Needleman [8] and Tvergaard [9] developed models that are similar to plasticity models in that they are rate independent, but can account for history dependence due to cyclic loading. A similar, though much simpler model discussed by Costanzo and Allen [10], was able to yield analytic predictions in certain circumstances. Perhaps the most advanced cohesive zone models for polymers have been proposed by Knauss and coworkers [11-13], and Schapery [14-18]. The present authors have also recently developed certain aspects of a cohesive zone model for application to viscoelastic media [19-21]. In this work, a new cohesive zone model has been proposed [19], and the thermodynamics of crack propagation have been studied thoroughly [19]. Furthermore, the numerical integration of the cohesive zone model has been discussed [20], and the implementation to a finite element code has been documented [21]. In this paper, we discuss a micromechanical basis for the cohesive zone model.

Micromechanical Cohesive Zone Model

Cohesive zone models have found use when the planar dimension of the damaged zone ahead of a crack tip is very large compared to the out-of-plane dimension, as shown in Fig. 1. In this case, the region ahead of the crack tip is idealized as a plane of zero thickness (in the undeformed state) with a dissipative traction-displacement relation that is of the form

$$T_i(x_k,t) = T_i\{u_m(x_k,t),\alpha(x_k,t)\} \tag{1}$$

where T_i are the components of the traction vector, u_i are the components of the crack opening displacement vector, and α is an internal variable representing damage. Note that the braces signify history dependence, so that the current value of T_i is a functional of the entire history of the variables on the right hand side. Recent research has shown that this type of model leads quite naturally to a critical energy release rate that is both rate and history dependent [19].

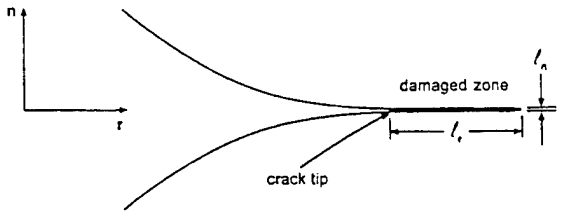

Figure 1: Characteristic Dimensions of the Damaged Zone

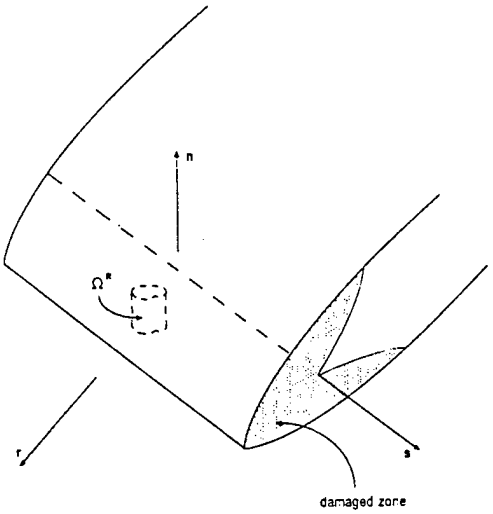

Figure 2: The Damaged Zone

Difficulties with cohesive zone models typically arise when attempts are made to determine the material properties necessary to describe equation (1). This is due to the fact that the cohesive zone usually occupies an extremely small region ahead of the crack tip, so that experimental measurements are difficult to make accurately. Therefore, new methods of developing cohesive zone models described by (1) are necessary in order to produce relations in which the material constants can be determined a priori and with physically reasonable insight.

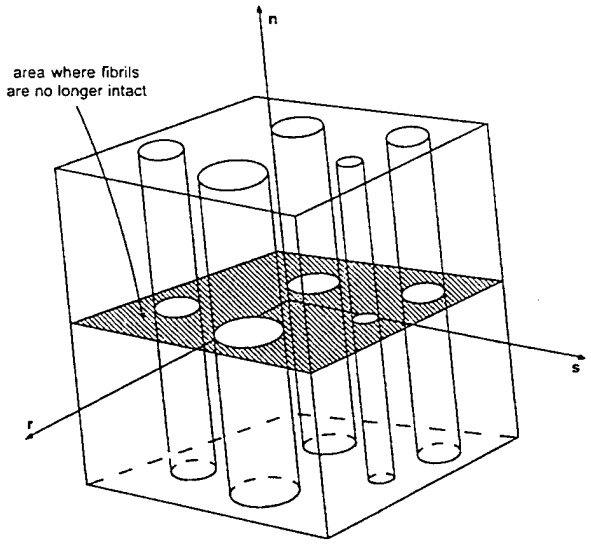

Figure 3: Idealization of the Representative Volume Element within the Damaged Zone.

We discuss here one such method in which a micromechanics problem is solved on a very small scale compared to the planar dimensions of the cohesive zone, as shown in
Fig. 2. In this case, we consider a representative volume in a craze zone, such that the representative volume element may be approximated by the boundary value problem shown in Fig. 3. In this case, each fibril in the craze zone is assumed to carry load uniaxially. The governing field equations for the boundary value problem are the conservation of linear momentum:

$$\sigma_{ji,j} = 0 \tag{2}$$

where σ_{ij} is the stress tensor, and body forces are neglected. Also, the strain-displacement equations

$$\varepsilon_{ij} = \tfrac{1}{2}\left(u_{i,j} + u_{j,i}\right) \tag{3}$$

where ε_{ij} is the strain tensor, and we have assumed small displacement gradients for simplicity, although large displacement gradients could be included in the model with little additional difficulty. Furthermore, the mechanical constitutive behavior of the fibrils is assumed to be linear viscoelastic, such that

$$\sigma_{ij} = \int_0^t E(t-\tau)\frac{\partial \varepsilon_{ij}}{\partial \tau}\, d\tau \tag{4}$$

where $E(t)$ is the relaxation modulus. Solution of the above boundary value problem is possible in closed form since the problem is statically determinate for the case of imposed boundary displacements [22]. The resulting homogenized traction-displacement relation is given by

$$T_i(t) = \frac{u_i(t)}{\delta_i \lambda(t)}\left[1-\alpha(t)\right]\left[\sigma_i^f + \int_0^t E(t-\tau)\frac{\partial \lambda}{\partial T}\, d\tau\right] \tag{5}$$

where α is a damage parameter that is equivalent to the cross-section of voided material divided by the total cross-sectional area, as shown in Fig. 5. We note here that the term homogenized simply implies that since the scale of the RVE is small compared to the actual cohesive zone, the mechanical constitution of the RVE can be approximated without significant loss of accuracy by relating the boundary average of the traction to the boundary average of the displacements in the RVE. This results in a "homogenized" material in which there are not internal boundaries (within the cohesive zone), and the dissipation due to microstructural damage evolution (such as fibril breakage) is reflected in the damage parameter, α. Since fibrils do have the propensity to break during loading, the damage does evolve, and the parameter must be modeled by an ancillary constitutive equation called an internal variable evolution law. We have considered

several forms of this law [19,20], but for the sake of simplicity, we mention only one phenomenological possibility here:

$$\dot{\alpha} = \alpha_1 \lambda^m \tag{6}$$

This evolution law allows for the growth of damage in the cohesive zone, such that when α attains the value of unity, the traction components all become zero Equation 5, with the result that the cohesive zone becomes a traction free surface, resulting in crack advance. Therefore, it is not necessary to track the energy release rate in order to model crack propagation. Rather, the nonconvexity of the cohesive zone model produces a natural instability that results in crack extension.

Example Problems

In order to demonstrate the efficacy of the cohesive zone model, we consider here an example problem. In this problem, we consider only a single point at fixed coordinate location in a cohesive zone ahead of a crack tip. The material point is subjected to monotonically increasing opening displacement (without shear displacement) at constant displacement rate. For convenience, the relaxation modulus of the fibrils is assumed to be modeled by a standard linear solid, such that

$$E(t) = E_\infty + E_1 e^{-\frac{E_1 t}{\eta_1}} \tag{7}$$

An input opening displacement is applied at constant rate, thus producing an opening

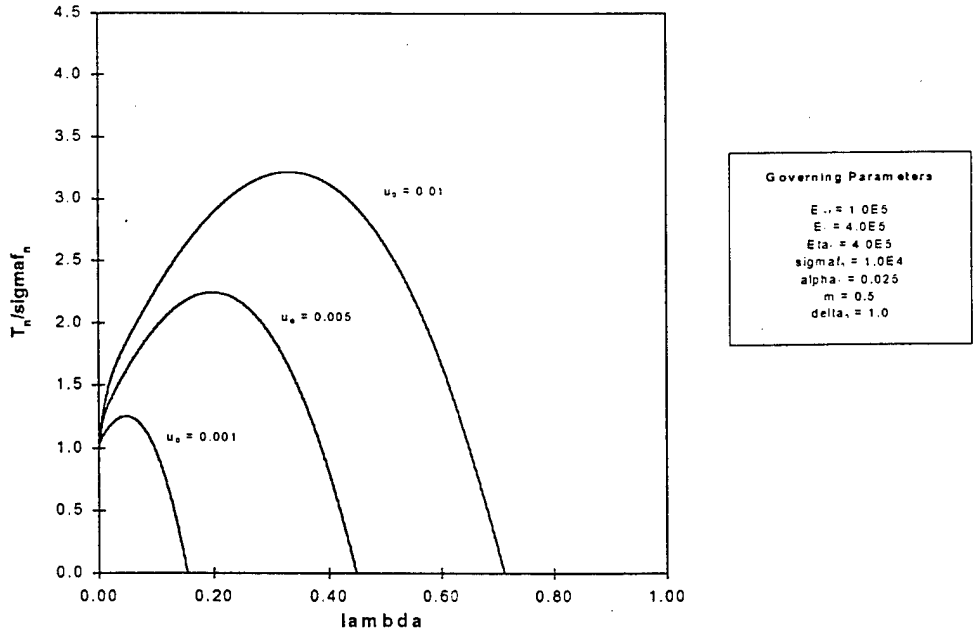

Figure 4: Closed Parametric Study on the Variation in the Traction-Displacement Relationship with Respect to the Viscous Damping Coefficient (η_1)

traction in response, as shown in Fig. 4. The figure shows three different curves, each with different values of the dashpot viscosity, thus indicating explicitly the rate dependence in the model for varying material properties. As shown in Fig. 5, there is also an effect on loading rate. Shown in this figure are predictions for three different displacement loading rates. Note that in all cases the opening traction eventually reaches a peak value and then decreases to zero, at which point the crack will advance.

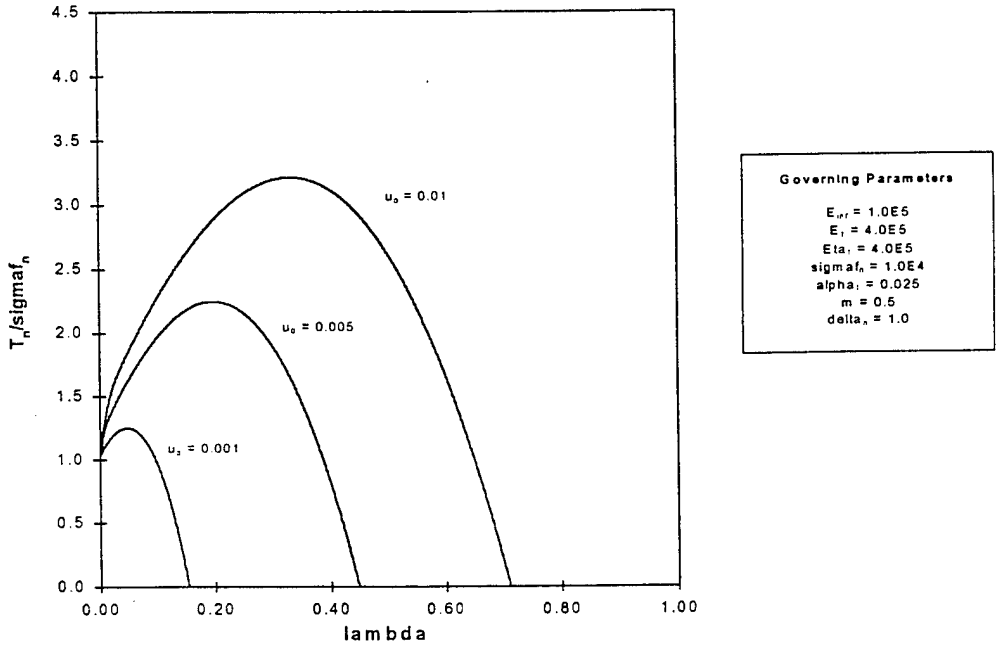

Figure 5: Closed Form Parametric on the Variation in the Traction-Displacement Relationship with Respect to the Displacement Rate (u_o)

Although not described in detail in this paper, it has been previously demonstrated that the area under the curve in Figs. 4 and 5 is related to the energy release rate for a cohesive zone ahead of a crack tip [19]. Similarly, it has also been shown that the critical energy release rate is not a constant for this material model [19]. Thus, it is apparent that both the available energy and the required energy for crack propagation are non-stationary material properties that are both rate and history dependent when the cohesive zone model discussed herein is utilized.

For further evaluation, the cohesive zone model has been implemented in an implicit finite element code and an example problem has been considered. A double cantilevered beam is subjected to monotonically increasing self-equilibrating loads of 10 lbf/s. It has been previously reported that the cohesive zone traction field does not undergo self-similar propagation [22]. Also worth noting is that the length of cohesive zone does not undergo self-similar propagation

as shown in Fig. 6. At 21.6 seconds, the crack tip has advanced from its previous position while the cohesive zone tip has not.

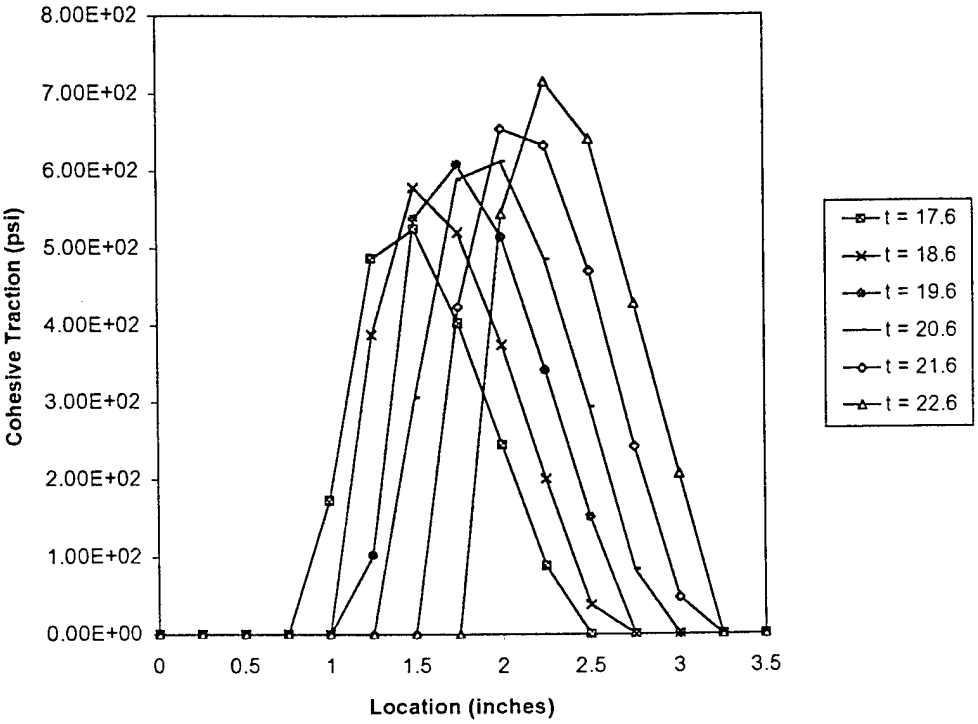

Figure 6: Predicted Tractions vs. Location at Selected Times.

Conclusion

A viscoelastic cohesive zone model has been proposed herein, and example results have indicated the explicit rate dependence in the model. Recently, this model has been utilized to predict crack extension in viscoelastic media [20]. Although not discussed in detail herein, it is possible to obtain the material constants for the cohesive zone model from macroscopic fracture toughness tests [22]. Although the model requires further study, results are at least in qualitative agreement with experimentally observed behavior of some polymeric materials.

Acknowledgment

The authors gratefully acknowledge the support provided this research by the U.S. Army Research Office under grant no. DAAG55-98-1-0119 and AFOSR under grant no. F-49620-97-0338.

REFERENCES

1. Griffith, A. A., The Phenomena of Rupture and Flow in Solids, Philosophical Transactions of the Royal Society of London, A221:163-197, 1920.
2. Rice, J. R., Mechanics of Crack Tip Deformation and Extension by Fatigue, in Fatigue Crack Propagation, Philadelphia: ASTM STP 415, pp. 247-309, 1967.
3. Gurtin, M.E., "On the Energy Release Rate in Quasi-Static Elastic Crack Propagation," Journal of Elasticity, Vol. 9, No. 2, pp. 187-195, 1979.
4. Nguyen, Q.S, "A Thermodynamic Description of the Running Crack Problem," Symposium, Dourdan, North Holland, pp. 315-330, 1980.
5. Dugdale, D. S., Yielding of Steel Sheets Containing Slits, Journal of the Mechanics and Physics of Solids, 8: 100-104, 1960.
6. Barenblatt, G. I., The Mathematical Theory of Equilibrium Cracks in Brittle Fracture, Advances in Applied Mechanics, 7: 55-129, 1962.
7. Kramer, E. J. and L. L. Berger, Fundamental Processes of Craze Growth and Fracture, in Advances in Polymer Science 91/92: Crazing in Polymers, Vol. 2, H.-H. Kausch, ed., Springer-Verlag , pp. 1-68, 1990.
8. Needleman, A., A Continuum Model for Void Nucleation by Inclusion Debonding, Journal of Applied Mechanics, 54: 525-531, 1987.
9. Tvergaard, V., 1990. Effect of Fibre Debonding in a Whisker-Reinforced Metal, Materials Science & Engineering A:Structural Materials: Properties, Microstructure, and Processing, A125(2): 203-213, 1990.
10. Costanzo, F. and D.H. Allen, "A Continuum Mechanics Approach to Some Problems in Subcritical Crack Propagation," International Journal of Fracture, 63: 27-57, 1995.
11. Ungsuwarungsri, T. and W. G. Knauss, A Nonlinear Analysis of an Equilibrium Craze: Part I - Problem Formulation and Solution, Journal of Applied Mechanics, 55: 44-51, 1988.
12. Ungsuwarungsri, T. and W. G. Knauss, A Nonlinear Analysis of an Equilibrium Craze: Part II - Simulations of Craze and Crack Growth, Journal of Applied Mechanics, 55: 52-58, 1988.
13. Knauss, W. G. and G. U. Losi, Crack Propagation in a Nonlinearly Viscoelastic Solid with Relevance to Adhesive Bond Failure, Journal of Applied Mechanics, Vol. 60, pp. 793-801, 1993.
14. Schapery, R. A., A Theory of Crack Initiation and Growth in Viscoelastic Media: Part I, International Journal of Fracture, 11(1):141-159, 1975.
15. Schapery, R. A., A Theory of Crack Initiation and Growth in Viscoelastic Media: Part II, International Journal of Fracture, 11(3):369-387, 1975.
16. Schapery, R. A., A Theory of Crack Initiation and Growth in Viscoelastic Media: Part III, International Journal of Fracture, 11(4):549-562, 1975.
17. Schapery, R.A., Correspondence Principles and a Generalized J-Integral for the Large Deformation and Fracture Analysis of Viscoelastic Media, International Journal of Fracture, 25, 195-223, 1984.
18. Schapery, R. A., Deformation and Fracture Characterization of Inelastic Composites Materials Using Potentials, Polymer Engineering and Science, 27, 63-76, 1987.

19. Yoon, C. and D. H. Allen, Damage Dependent Constitutive Behavior and Energy Release Rate for a Cohesive Zone in a Thermoviscoelastic Solid, to appear in the International Journal of Fracture.
20. Allen, D. H. and C. R. Searcy, Numerical Aspects of a Micromechanical Model of a Cohesive Zone, to appear in the Journal of Reinforced Plastics and Composites.
21. Foulk, J. W., D. H. Allen, and K.L.E. Helms, Formulation of a Three Dimensional Cohesive Zone Model for the Application to a Finite Element Algorithm, submitted to Computational Methods in Applied Mechanics and Engineering.
22. Allen, D.H. and C.R. Searcy, A Micromechanical Model for a Viscoelastic Cohesive Zone, submitted to the International Journal of Fracture.

Journal Articles

Allen, D.H., and Searcy, C.R., "Numerical Aspects of a Micromechanical Model of a Cohesive Zone," ***Journal of Reinforced Plastics and Composites,*** Vol. 19, No. 3, pp. 240-248, 2000.

The numerical aspects of a micromechanical model for a viscoelastic cohesive zone are discussed herein. The cohesive forces encountered in the region ahead of a crack tip are represented by a damage dependent traction-displacement law which is both history dependent as well as internal variable-type. An incrementalized form of this traction-displacement law has been integrated numerically, and an example problem has been solved to demonstrate the efficacy of the model.

Allen, D.H. and Searcy, C.R., "A Micromechanical Model for a Viscoelastic Cohesive Zone," to appear in ***International Journal of Fracture***, 2000.

A micromechanical model for a viscoelastic cohesive zone is formulated herein. Care has been taken in the construction of a physically-based continuum mechanics model of the damaged region ahead of the crack tip. The homogenization of the cohesive forces encountered in this region results in a damage dependent traction-displacement law which is both single integral and internal variable-type. An incrementalized form of this traction-displacement law has been integrated numerically and placed within an implicit finite element program designed to predict crack propagation in viscoelastic media. This research concludes with several example problems on the response of this model for various displacement boundary conditions.

Allen, D.H., and Searcy, C. R., "A Micromechanically-Based Model for Predicting Dynamic Damage Evolution in Ductile Polymers," submitted to ***Mechanics of Materials***, 2000.

A new micromechanically-based viscoelastic cohesive zone model is proposed that extends the features of a quasi-static model previously developed by the authors. A statistical distribution of fibril radii is assumed, and a critical fibril radius is introduced as a fracture criterion. Results are presented for various loading rates, and it is found that this dynamic damage model is both physically motivated and capable of modeling complex phenomena in cohesive zones.

MICROMECHANISM BASED MODELING OF METAL MATRIX COMPOSITES

David H. Allen
and
Dimitris C. Lagoudas

Center for Mechanics of Composites
Texas A&M University System
College Station, TX 77843-3141

AFOSR Grant No. F49620-97-1-0338
Final Progress Report

November 2000

ABSTRACT

The parent grant for this AASERT grant was funded by AFOSR for a period of three years beginning on June 15, 1994. The title of this research effort is "Micromechanism Based Modeling of Metal Matrix Composites (MMC) Subjected to Thermal Transients." The primary thrust of this research is to develop life prediction models for titanium matrix continuous fiber composites for applications at elevated temperatures in gas turbine blades and disks. Since these components are subjected to cyclic thermomechanical loading, major emphasis in the parent grant is placed on the spatial and time dependent effects caused by temperature. The research program focuses on the evolution of microstructural damage in the presence of matrix thermoviscoplasticity caused by post processing cooldown and subsequent thermomechanical loading. Both computational and analytic models are under development to account for these complicated and interacting phenomena. It is envisioned that if accurate models can be developed to predict life of MMC, then these models can be utilized to develop new composites which satisfy design constraints. The AASERT grant supplements the parent grant with emphasis on experimental efforts and computational implementations geared towards enhancing our understanding of MMCs. Recent research has demonstrated that environmental degradation in the form of oxidation has a substantial adverse impact on MMC life.

Research Thrusts

The objectives of the parent and AASERT grant are: **1) to develop a micromechanics and thermodynamics based model for predicting macroscopically averaged thermomechanical constitutive behavior of continuous fiber MMC; 2) to develop and test MMC experimentally to determine microscopic variables that are necessary to develop the micromechanics model mentioned in 1); and 3) to carry out a limited experimental program of model verification.** Although the methodology developed herein is applicable to generic MMC, two candidate materials are being considered in detail; Sigma/Ti-15-3 and SCS-6/Ti-β21S.

The modeling portion of the research program comprises approximately seventy percent of the overall effort. Motivated by experimental evidence, a wide variety of complex micromechanical features are being incorporated into the micromechanics model to accurately capture all energy storage and loss mechanisms that are significant precursors to macroscopic fracture. These features include: 1) matrix thermoviscoplasticity; 2) processing induced residual stresses; 3) interfacial and matrix microcracking; 4) oxidation phenomena, and 5) time dependent interphase reaction kinetics. Where possible, results are obtained analytically; however, the complexities noted above lead in most cases to solutions obtained computationally by the finite element method (FEM). All numerical algorithms are developed in-house by the investigators.

Our computational finite element model has now reached the stage where we have included the following: 1) three dimensional modeling capability; 2) the ability to predict damage evolution using fracture mechanics models; 3) the effects of oxidation in a surface layer embattlement and phase change; and 4) matrix thermoviscoplasticity. Our initial results with this model indicate that we can accurately predict fatigue behavior of both oxidized and unoxidized

composite MMC's, in both cases accounting for damage evolution. Our oxidation model, verified by experiments is capable of predicting oxidation zones in specimens with complex geometries.

Students Supported by the AASERT grant

Chad Searcy
John J. Mayes
Mark Phillips
David A. Miller
Jon Fleitman

Publications produced as a result of this project are attached.

Influence of Heat Treatment on the Mechanical Properties and Damage Development in a SiC/Ti-15-3 MMC

David A. Miller

Dimitris C. Lagoudas

Center for Mechanics of Composites,
Department of Aerospace Engineering,
Texas A&M University,
College Station, TX 77843-3141

Titanium alloys are commonly heat-treated to meet specific design requirements. In an effort to possibly create a better composite, the influence of heat treatments on the damage evolution and strength of a SiC/Ti-15-3 metal matrix composite (MMC) was studied. Heat treatments of 450°C and 700°C for 24 hours were performed on axial and transverse unidirectional specimens. These specimens, in addition to specimens in the as-received condition, were tested under nonproportional loading paths and then microstructurally analyzed to determine the induced damage. The axial composite with the 450°C heat treatment showed the highest elastic modulus and the lowest stiffness reduction than the other heat treatment conditions. The transverse composite in the as-received condition showed the highest room temperature elastic modulus and the lowest stiffness reduction compared with other heat treatment conditions. Typical damage modes of Ti MMC's, such as fiber/matrix debonding and matrix microcracking, were seen in all heat treatments. A micromechanics model based on the Mori-Tanaka averaging scheme was implemented to simulate the effects of microcracking induced damage on composite stiffness reduction.

1 Introduction

Designs for the next generation of supersonic and hypersonic aircraft as well as engine components will require advanced materials that can withstand elevated temperatures in structural applications. Metal matrix composites (MMC's) have recently undergone serious evaluation to satisfy this need because of their high strength, low weight, and elevated temperature capabilities. Titanium has been the primary matrix material considered because of its formability, high strength-to-weight ratio, and high melting temperature (1668°C). Titanium also has the advantage that its microstructure can be altered by alloying with metals which will stabilize the α or β phase to satisfy many different design requirements.

Structural titanium MMC's are often reinforced with continuous silicon carbide (SiC) fibers fabricated through a chemical vapor deposition process. To date, the results for the SiC/Ti systems have shown severe limitations. The composite shows improved performance in the fiber direction compared with monolithic titanium, but the transverse fiber direction properties are considerably less. Johnson (1992) has shown in an SCS-6/Ti-15-3 MMC composite with off axis plies that fiber-matrix separation leads to a knee in the stress/strain curve well below the matrix yield level. This damage was confirmed by a reduction in the unloading modulus and edge replicas. Combined loading paths have been studied by Lissenden et al. (1995), in SiC/Ti tubes. Results have shown that fiber/matrix interfacial debonding was observed in the stress-strain response and verified through microstructural evaluations.

Mujumdar and Newaz (1992a, b, 1993) have performed room temperature experimental studies of the SCS-6/Ti-15-3 composite identifying the inelastic deformation mechanisms of plasticity and damage. Lagoudas et al. (1995) studied the effect of surface damage on oxidized SiC/Ti-15-3 MMC laminates under tensile loading, and an effective stiffness reduction due to the development of cracks on the surface of the composite was evaluated. Newaz et al. (1992) investigated the thermal cycling response of quasi-isotropic SiC/Ti-15-3 MMC's. Johnson et al. (1990) performed room temperature tests to characterize a SiC/Ti-15-3 MMC in both the as-received condition and aged at 482°C for 16 hr. This heat treatment was shown to increase the elastic modulus, the ultimate strength and the yield stress of the matrix.

Several different temperatures have been utilized for heat treatments of MMC's in previous works, (Johnson, et al., 1990; Lerch et al., 1990a) although rigorous comparisons were not made among different heat treatments. In fact, the motivation behind the heat treatments was not discussed, other than to stabilize the microstructure. Wolfenden et al. (1996) utilized nondestructive techniques to investigate the effect of heat treatments on the elastic modulus, damping and microhardness for SiC/Ti-15-3. Lerch and Saltsman (1991), advanced Johnson's room temperature results with a study of the SCS-6/Ti-15-3 MMC at 427°C. Specimens were tested as-received and with a heat treatment of 700°C for 24 hrs. However, the effect of heat treatment and resulting microstructures on the damage development of MMC's has not been addressed.

The objective for this work is to study possible improvements on a SiC/Ti-15-3 MMC through different heat treatments and to experimentally characterize the deformation and damage mechanisms associated with each. The effects of heat treatment on the thermomechanical response and damage development in unidirectional specimens, loaded axially and transverse to the fibers, are discussed in the second section. The third section utilizes an averaging micromechanics technique for the correlation of crack density as a damage parameter with stiffness reduction and compares model predictions with experimental results.

2 Experimental Results on Thermomechanical Response of SiC/Ti-15-3 With Different Heat Treatments

2.1 Material Description and Specimen Preparation. All tests in this research were performed on a composite material manufactured by DWA Specialty Metals using the foil-fiber-foil technique. The composite is a 4-ply unidirectional SiC/Ti 15-3 MMC with a 32% fiber volume fraction. The matrix is reinforced

Contributed by the Materials Division for publication in the JOURNAL OF ENGINEERING MATERIALS AND TECHNOLOGY. Manuscript received by the Materials Division August 5, 1997; revised manuscript received May 3, 1999. Associate Technical Editor: S. A. Meguid.

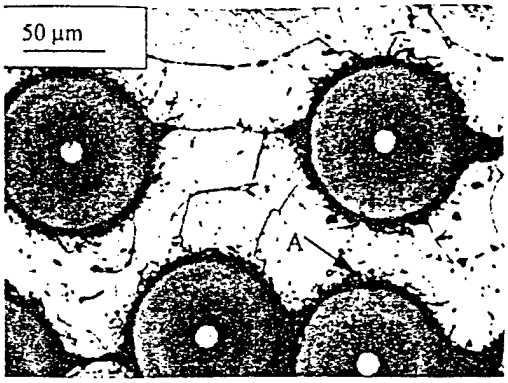

Fig. 1 Microphotograph of a tested as-received specimen polished and etched to reveal the microstructure

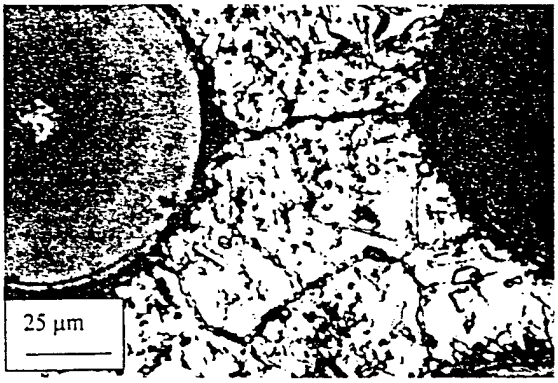

Fig. 3 Microphotograph of a tested 700°C/24 hour heat treatment specimen polished and etched to reveal the microstructure

by SiC fibers manufactured by British Petroleum. The average fiber diameter was 100 μm and has a structured carbon-titanium diboride coating (Allen et al., 1994). The alloy utilized in this composite is a metastable β-phase alloy commonly referred to as Ti 15-3, and has an actual weight percent of 15% V, 3% Al, 3% Cr, 3% Sn and the balance Ti.

The composite was tested in the as-received condition and with heat treatments of 450°C for 24 hours and 700°C for 24 hours. Heat treatments were performed in a vacuum to prevent oxidation from degrading the material. The as-received material, see Fig. 1, contains large α-phase needles, labeled as A. The α-particles are seen primarily along the fiber interface creating a β-depleted zone around the fiber area. Results from an energy dispersive spectroscopy (EDS) line scan show a high carbon concentration in the α rich region surrounding the fiber, possibly due to the coating. Carbon is an α-stabilizer for titanium, thus explaining the α rich region surrounding the fiber. The α rich region surrounding the fiber seen in this composite has not been observed in other Ti-15-3 systems (e.g., in the work of Lerch and Saltsman, 1991, where the SCS-6/Ti-15-3 MMC has been studied). Since the fiber coatings differ for the Sigma fiber and the SCS-6 fiber, the possibility of different fiber/matrix interfaces exist.

The 450°C heat treatment produces a small fine α-particle precipitant with virtually no congregation along the grain boundary, as seen in Fig. 2. The distinct fiber matrix interface region remains, but the precipitant accumulation around the fiber has disappeared. The aging heat caused the precipitant to distribute throughout the grain structure. The grains remain the same size, but are not as apparent as before the redistribution of the α-phase. It has been shown (Lerch et al., 1990a) that this heat treatment produces the highest room temperature modulus for the matrix material. This is to be expected since the HCP α-phase has a higher stiffness than the BCC β-phase. However, the increase in α-phase also decreases the number of active slip planes thus reducing the ductility of the material.

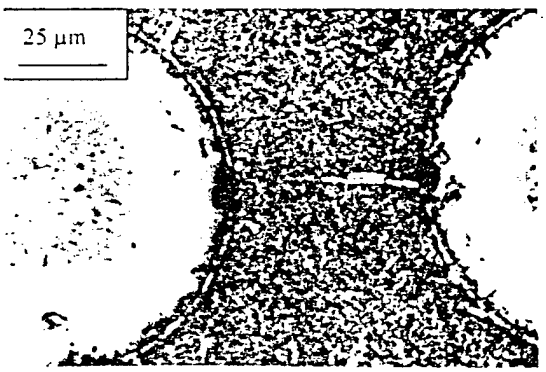

Fig. 2 Microphotograph of a tested 450°C/24 hour heat treatment specimen polished and etched to reveal the microstructure

The 700°C heat treatment, Fig. 3, results in large α-phase needles dispersed throughout the β-phase grains, while the grain size remains unchanged. The β-depleted region around the fibers is still present, as well as the grain boundary phases. It has been shown that this heat treatment slightly reduces the stiffness of the titanium from the as-received condition (Lerch et al., 1990a).

2.2 Thermomechanical Testing Description. All tests were performed on an MTS servo-hydraulic load frame under load control at a rate of 10.4 MPa/sec. Elevated temperature tests were performed using a three-zone clamshell resistance furnace. Strain measurements for all tests were made with a one-inch gage high temperature extensometer.

In order to study the evolution of inelastic deformation throughout the entire loading path, cyclic tension tests with an increasing stress amplitude were performed at room temperature and at 427°C (800°F). Measurement of the unloading elastic modulus for each cycle quantified the damage imparted into the specimen at the applied stress level. Cyclic loading paths were used to study the development of inelastic deformation in the composite and monitor the degradation of the initial elastic modulus. The loading path consisted of unloading to 10% of the maximum applied stress in each cycle with the maximum stress incrementally increasing in each successive cycle to a value approaching the failure stress of the composite.

A total of six unidirectional composite specimens loaded in the fiber direction (axial specimens) were investigated in this study allowing for one cyclic test for each heat treatment and testing temperature. Also investigated were nine specimens loaded transverse to the fiber direction (transverse specimens). The transverse tests consisted of one monotonic test to failure for each heat treatment at room temperature and one cyclic test for each heat treatment and testing temperature. Due to the small number of specimens tested, this study only qualitatively addresses the influence of heat treatment on the material parameters (e.g., elastic modulus) of the composite. Since limited material did not allow for multiple tests of the same heat treatment, possible variations of the material parameters due to material heterogeneity cannot be addressed in this study. However, all specimens were taken from the same composite plate, thus, the manufacturing process was identical for each specimen. Although the present experiments cannot identify material parameters without a large margin of error, the degradation of material properties reported here should be indicative of damage induced changes in similarly produced Ti-15-3 systems.

Microstructural evaluations were performed after each test to determine the state of damage in the composite. The specimens were carefully sectioned, polished and etched for a detailed microstructural evaluation with light microscopy and scanning electron microscopy.

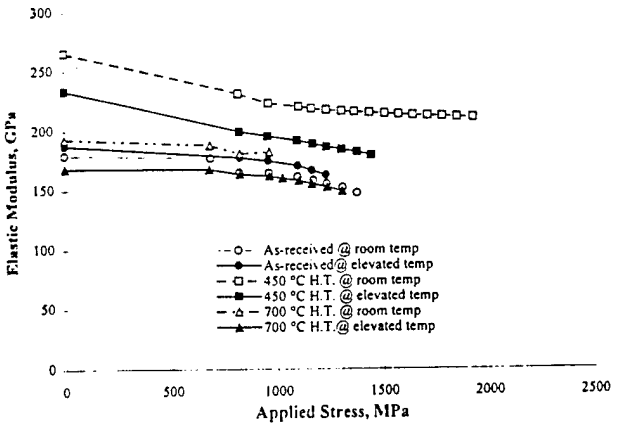

Fig. 4 Unloading axial elastic modulus versus applied stress for axial specimens

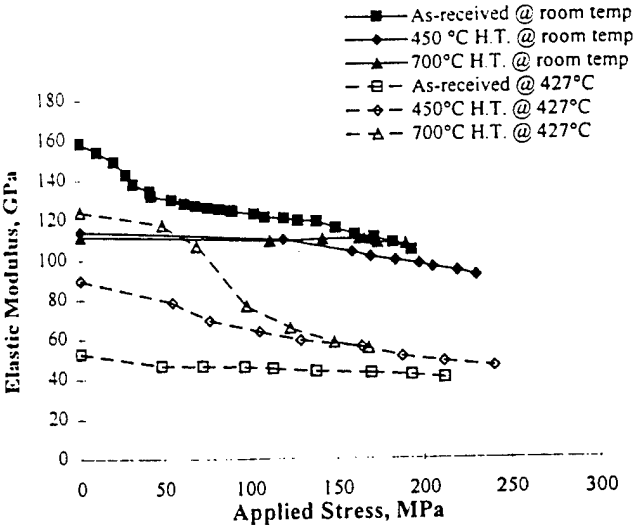

Fig. 5 Unloading transverse elastic modulus versus applied stress for transverse specimens

2.3 Axial Tension Tests. Three cyclic tests, one for each heat treatment, were conducted at room temperature and at 427°C for axial specimens. For brevity, only the results of the unloading elastic modulus as a function of the applied stress are shown in Fig. 4. As seen in Fig. 4, the 450°C specimen has the highest elastic unloading modulus for both room temperature and elevated temperature tests. This was expected since the 450°C heat treatment creates the highest room temperature modulus and yield point in the matrix due to the high concentration of HCP α-phase present throughout the matrix. The 700°C specimen tested at elevated temperature has the lowest initial elastic modulus of the three treatments, although the as-received specimens have similar values. These specimens have similar microstructures with the primary difference being the size of the precipitant as seen in Figs. 1 and 3.

A reduction in elastic modulus is seen throughout the entire test for each specimen as the applied stress increases, indicating that damage is present in all specimens. However, the 450°C specimen tested at room temperature settles to a constant unloading modulus above 1500 MPa. The inelastic deformation in the axial direction has been shown to be primarily dominated by matrix plasticity, rather than damage (Majumdar and Newaz, 1992a), although the results seen in Fig. 4 show that damage is present. Microstructural evaluation of the specimens reveal both fiber cracks and matrix cracks in room and elevated temperature tests, however, a uniform spacing of cracks was not found. Matrix cracks were seen to travel across fibers, without causing fiber failure, although, on failed specimens the fiber/matrix interface was debonded. From the catastrophic failure seen and heard when the composite failed, it can be assumed that the fibers fail almost simultaneously. Regardless of the heat treatment and testing temperature, all specimens failed in the range of the fiber strain limit of 0.9–1.0%.

2.4 Transverse Tension Tests. Three cyclic tests, one for each heat treatment condition, were conducted at room temperature and at 427°C. Also, a monotonic tension test to failure was performed at room temperature for each heat treatment to identify the regions of inelastic deformation to be studied in the cyclic tests. For brevity, only the results of the unloading elastic modulus are presented in Fig. 5. The as-received specimen tested at room temperature and the 700°C specimens tested at both room and elevated temperature showed inelastic deformation with no permanent strain, thus, the inelastic deformation is attributed only to damage. The 450°C heat treatment specimen tested at room temperature and the as-received specimen tested at elevated temperature showed inelastic deformation with a permanent strain. However, these tests both contained a knee, or stiffening, in the unloading curve, most likely due to the closing of the cracks along the debonded fiber/matrix interface. For both of these tests, the composite would unload to the origin without showing a permanent offset if the knee were not present. The 450°C heat treatment tested at elevated temperature showed inelastic deformation with a permanent strain, however, the knee is not observed in the unloading cycles. This implies that the permanent strain for this specimen is due to matrix plasticity, in contrast to all other transverse tests mentioned here.

The as-received specimen at room temperature, as seen in Fig. 5, showed the highest initial elastic modulus, but damage reduced the modulus as higher load levels were reached. The 700°C specimen had the highest elevated temperature modulus, but also showed the greatest loss of stiffness, while the as-received specimen at elevated temperature and the 700°C specimen at room temperature showed a slow rate of damage growth with the applied load. This point could be explained by the accumulation of microcracks reaching a saturation point at which the modulus no longer decreases. The 700°C and 450°C specimens tested at elevated temperature and the as-received and 450°C specimen tested at room temperature show a continuous drop in the unloading modulus, while the remaining tests settle to a nearly constant value.

The initial elastic modulus for the transverse tensile tests closely match published results for similar systems, however, the inelastic deformation described above occurs at stress levels well below the elastic limit seen in similar systems (about 275 MPa for room temperature SCS-6/Ti-15-3, Mujumdar and Newaz, 1992a; Lerch and Saltsman, 1991). The inelastic deformation is facilitated by the manufacturing flaws seen in the material, resulting in failure for as received, 450°C and 700°C specimens at 242 MPa, 274 MPa and 244 MPa respectively at room temperature. Observations of such a low failure stress similar to those presented here have not been reported in literature, but microstructural evaluations suggest a

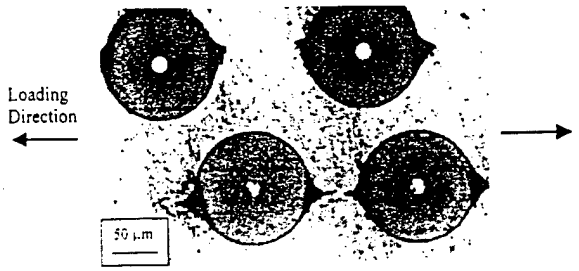

Fig. 6 Example of representative tested unetched transverse specimens showing cracks emanating from manufacturing flaw and propagating toward fiber

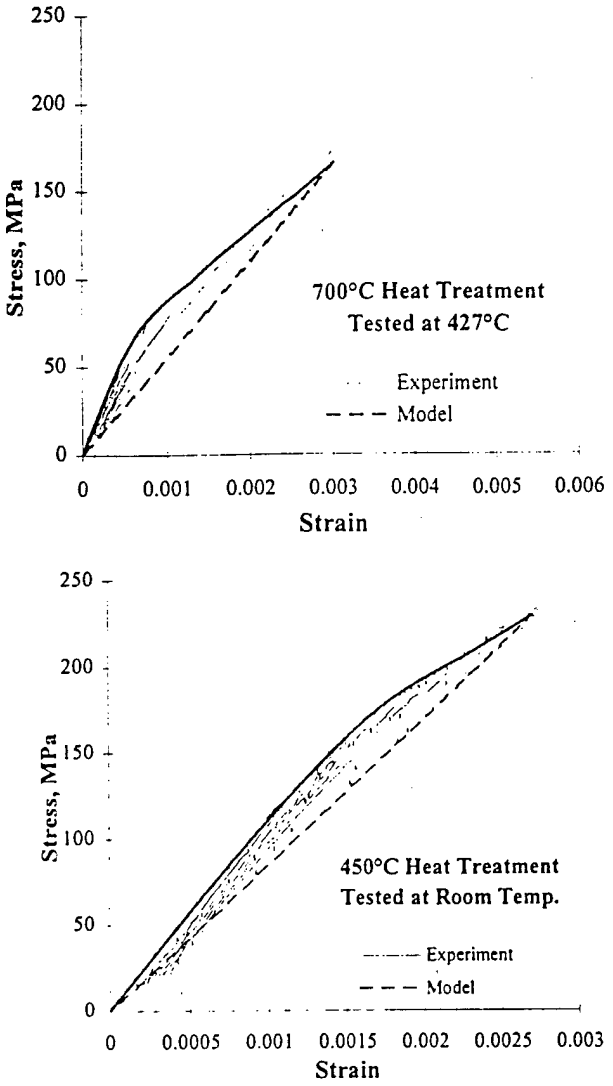

Fig. 7 A comparison between the simulated stress/strain response and experimental measurements for (*a*) 700°C specimen tested at elevated temperature and (*b*) 450°C specimen tested at room temperature

correlation between the low failure stress and the pre-existing manufacturing defects in the specimens tested in this work.

Microstructural evaluation shows that damage for all of the specimens primarily occurs in the form of matrix cracking emanating from the fiber/matrix interface in the direction of the loading. Figs. 1, 2, 3, and 6 show examples of crack development in the transverse specimens. Figure 6 shows crack initiation from manufacturing flaws, while Figs. 1, 2, and 3 show the crack development along grain boundaries revealed through etching. Grain boundaries are prone to crack development in these specimens due to the brittle α-phase accumulation. From the etched microstructures seen in Figs. 1, 2, and 3 the highest level of α-phase grain boundary accumulation is seen in the 700°C heat treatment specimens and the lowest accumulation is seen in the 450°C heat treatment specimens. The premature failure of the specimens and lack of large permanent deformation, leads to the conclusion that crack development along grain boundaries, initiated by pre-existing manufacturing flaws, led to damage development and ultimate failure of the specimens at stress levels well below the composite elastic limit.

3 Thermomechanical Modeling of Damage in SiC/Ti-15-3 MMC

3.1 Model Development. In this section an attempt will be made to correlate the experimental observations with theoretical modeling. The actual deformation mechanisms are complex and involve damage evolving during the loading. An approximate averaging micromechanics method will be used to model the influence of the loading direction and material properties on the mechanical response of the composite. The model will be based on the extension of the Mori-Tanaka micromechanics averaging method (Mori and Tanaka, 1973) to include damage effects.

Averaging methods have been developed which model damage in fibrous composites. In the present study, an attempt will be made to incorporate evolving damage in an incremental formulation. For the present implementation of the incremental formulation, the increment of total strain, $\Delta\bar{\epsilon}^t$, for each increment of applied overall stress, $\Delta\bar{\sigma}$, is expressed as the sum of the elastic increment, and strain increment due to damage, i.e.,

$$\Delta\bar{\epsilon}^t = [\mathbf{M}^d|_{\bar{\sigma}+\Delta\bar{\sigma}} - \mathbf{M}^d|_{\bar{\sigma}}]\bar{\sigma} + \mathbf{M}^d|_{\bar{\sigma}+\Delta\bar{\sigma}}\Delta\bar{\sigma}, \quad (1)$$

where the first term calculates the strain increment introduced by damage through the change in the elastic damage compliance $\mathbf{M}^d$, and the second term is the elastic increment using the current value of the compliance.

The Mori-Tanaka method (Weng, 1984; Benveniste, 1987) utilizes the Eshelby equivalence tensor, $\mathbf{S}$, to calculate the elastic stress concentration factor, $\mathbf{B}_\alpha^\epsilon$, which relates the overall applied stress, $\bar{\sigma}$, to the stress in the α phase by

$$\sigma_\alpha = \mathbf{B}_\alpha^\epsilon\bar{\sigma}, \quad \alpha = f, m \quad (2)$$

where α indicates the fiber or matrix phase. For a two-phase composite, a computationally convenient stress concentration factor based on the Mori-Tanaka approximation is given by (Gavazzi and Lagoudas, 1990)

$$\mathbf{B}_f^\epsilon = [\mathbf{I} + c_m\mathbf{L}_m^\epsilon(\mathbf{I} - \mathbf{S})(\mathbf{M}_m^\epsilon - \mathbf{M}_m^\epsilon)]^{-1} \quad (3)$$

where $\mathbf{L}_\alpha^\epsilon$ and $\mathbf{M}_\alpha^\epsilon$ are the elastic stiffness and compliance tensors respectively, c_α is the volume fraction for each phase and $\mathbf{I}$ is identity matrix. The effective elastic compliance for the MMC can then be found using the following relation (Hill, 1965),

$$\mathbf{M}^\epsilon = \mathbf{M}_m + c_f(\mathbf{M}_f - \mathbf{M}_m)\mathbf{B}_f^\epsilon. \quad (4)$$

Substituting the elastic modulus for each heat treatment into the above equations yields an evaluation of effective elastic compliance for each heat treatment of the composite.

As the loading is increased, matrix cracks develop in the uni-

Table 1 Material properties for each heat treatment and testing temperature utilized in modeling (Lerch et al., 1990a; Johnson et al., 1990; Wolfenden et al., 1996)

	Matrix Properties						Fiber Properties
	Room temperature			Elevated temperature, 427°C			Room temperature and elevated temperature
	As-Rcvd	450°C	700°C	As-Rcvd	450°C	700°C	
E, GPa	92.4	104.8	90.0	78.0	83.0	77.5	395.1
ν	.32	.32	.32	.32	.32	.32	.19

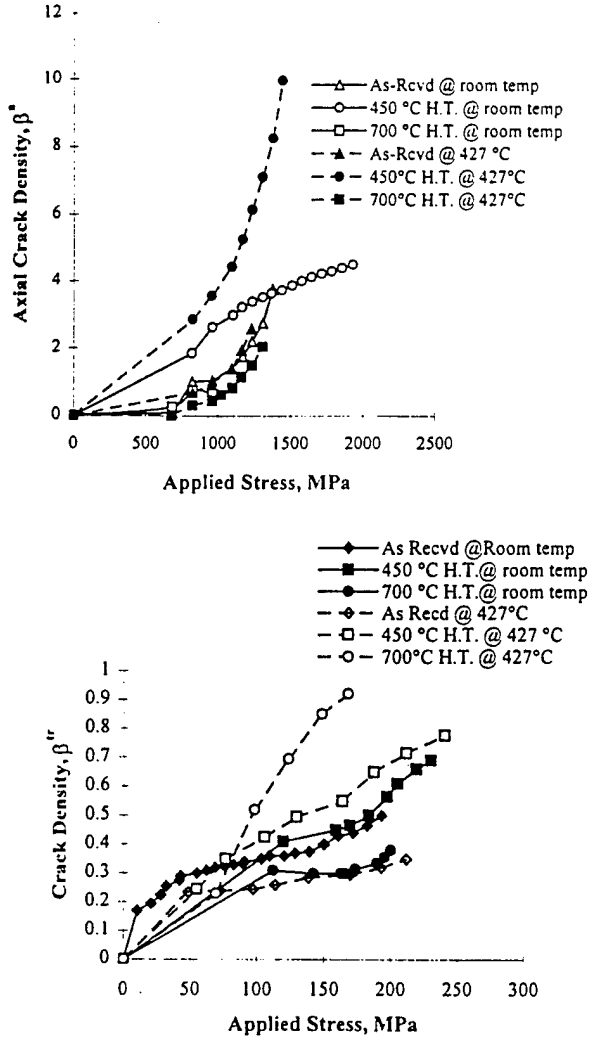

Fig. 8 Prediction of crack density as a function of applied stress for (*a*) axial crack density, β^a and (*b*) transverse crack density, β^{tr}

directional composite laminate and the above evaluation of the elastic compliance must be modified to account for the developing damage. The effect of cracks on the overall compliance of the composite is modeled using the methods derived by Laws and Dvorak (1987), and Dvorak et al. (1985) which relate the composite compliance to the density of cracks in the composite. Motivated by experimental observations, two different types of cracks are modeled, slit-cracks in the transverse specimens and penny-shaped matrix cracks in axial specimens.

The transverse crack density, β^{tr}, a function of the overall applied stress, is defined as the number of cracks of width, a, in a square cross-section of material with sides of length a. The damaged composite compliance, $\mathbf{M}^d$, is calculated as a function of the crack density β^{tr}. The Mori-Tanaka method is used to first generate the undamaged effective composite compliance, which is then revised as a function of the crack density (Dvorak et al., 1985).

In the axial specimens, cracks are modeled as a collection of penny-shaped matrix cracks transverse to the fibers. The crack density, β^a, is a function of applied load and is defined as the average number of cracks of specific diameter, d, in a cube with sides of length, d. The effective compliance of the composite is calculated in two steps. First, the matrix is regarded as a volume of homogeneous material with similar cracks of density β^a, for which an effective compliance, $\mathbf{M}_m^d$, is calculated as a function of the crack density (Dvorak et al., 1985). The second step utilizes the Mori-Tanaka method to generate an effective compliance of the damaged composite, $\mathbf{M}^d$, using the properties of the fiber and the damaged matrix, $\mathbf{M}_m^d$.

3.2 Implementation and Comparison With Experiments. Implementation of the averaging micromechanics approach to predict the mechanical response for damage requires knowledge of the evolution of the crack density, β, as a function of applied load. A damage growth model relating the crack density to the applied load is not utilized in this paper due to the inherent complexities those models contain. In the absence of a damage growth criterion, an experimental measurement will be utilized to determine the contribution of damage to the total inelastic deformation during a given loading path. Specifically, the damage will be determined from the experimentally measured components of the elastic unloading stiffness, $\mathbf{L}^d(3, 3)$, shown in Fig. 4 and $\mathbf{L}^d(2, 2)$ shown in Fig. 5, where $\mathbf{L}^d = [\mathbf{M}^d]^{-1}$.

Using the experimental data from Figs. 4 and 5, the overall stress vs. strain response can be simulated accounting for damage evolution utilizing the method described above. Simulations were made for all specimens, however, for brevity only two transverse specimens are presented. A comparison between the simulated stress/strain response and experimental measurements are shown in Fig. 7 for the 700°C specimen tested at elevated temperature and the 450°C specimen tested at room temperature. In the simulation of the 700°C specimen at elevated temperature, Fig. 7(*a*), the inelastic deformation is only due to damage, as evidenced by the lack of permanent deformation. For the 450°C specimen tested at room temperature, the simulation shows that the knee in the unloading curve is the cause of the permanent deformation, suggested by the simulation matching the initial unloading modulus above the knee and fully unloading with no permanent deformation, Fig. 7(*b*).

A prediction of crack density as a function of applied load can be determined by solving for the transverse crack density, β^{tr}, and the axial crack density, β^a, that yields the experimentally measured component of the unloading elastic stiffness. Since uniaxial stress states are investigated, only the components of compliance in the loading direction will be calculated. The model prediction of the crack density as a function of the applied stress is shown in Fig. 8 using the material properties listed in Table 1. To verify the model predictions for the resulting crack density as a function of applied load, post-test microstructural evaluations were made. The average crack densities measured from the specimens are compared to the predicted crack densities at the maximum applied stress shown in Fig. 8. Table 2 contains the measured and predicted values of the crack densities for each heat treatment and test temperature for the transverse composite.

Table 2 Comparison of experimental and predicted crack densities, β^{tr}, after final loading for transverse specimens

	Room temperature			Elevated temperature, 427°C		
	As-Rcvd	450°C	700°C	As-Rcvd	450°C	700°C
Experiment	.33	.35	.22	.23	.39	.28
Model Prediction	.50	.69	.38	.35	.76	.92

In transverse specimens, the experimental crack density was measured from a representative microphotograph of each sample, and calculated as the number of cracks of average measured crack width, a, divided by the number of squares with sides of length, a, in a square area encompassing the entire cross-section of the specimen. The crack width was taken to be the extent of the matrix crack often developing adjacent to a fiber, and perpendicular to the loading direction, as seen in Fig. 6. Note that the matrix cracks, which propagate along the grain boundary in the direction of the load, are not considered in the measured transverse crack density. The predicted crack densities for the transverse specimens, shown in Table 2, are higher than the experimentally measured values especially for the elevated temperature tests. The pre-existing manufacturing defects in the composite may cause a larger experimentally measured stiffness reduction, thus leading to an overprediction of the crack density. In addition, matrix cracks bridging the fibers in the loading direction, not accounted in the measured crack densities, may play a role in the higher stiffness reduction leading to an overprediction of crack density. When the transverse matrix crack is coupled with the cracks developing along grain boundaries, the result is a higher stiffness reduction for the elevated temperature tests. Caution should be finally drawn to the fact that the model assumes non-intersecting matrix slit cracks, while the observed damage indicates crack coalescence in many of the examined specimens.

4 Conclusions

A SiC/Ti-15-3 MMC was studied to determine the effects of different heat treatments on the damage evolution at both room temperature and at 427°C. The thermomechanical study revealed that the heat treatments could affect the overall composite compliance and damage accumulation. Mechanical tests show that the 450°C heat treatment creates a microstructure with a consistently high elastic modulus and high damage tolerance for all loading conditions and temperatures.

Microstructural evaluation identified the primary damage modes for both the transverse and axial specimens. The axial specimens showed evidence of cracks developing perpendicular to the loading direction starting from the fiber/matrix interface. The transverse specimens showed cracks emanating from areas of poor consolidation resulting in cracks propagating in the loading direction along grain boundaries. A model based on the Mori-Tanaka method was developed and implemented which incorporates damage in an incremental formulation. The developed method successfully simulates the stress vs. strain response of the composite accounting for damage. A prediction of the crack density was made as a function of overall applied load. It was shown that the predicted crack density at the final load level overpredicts the crack densities measured from a post-test microstructural analysis for the transverse specimens, most likely due to the pre-existing damage along the fiber/matrix interface.

5 Acknowledgments

The authors acknowledge the support of AFOSR grant No. F49620-94-1-0341.

References

Allen, D. H., Eggleston, M. R., and Hurtado, L. D., 1994, "Recent Research on Damage Development in SiC/Ti Continuous Fiber Metal Matrix Composites," *Fracture of Composites*, E. A. Armanios, ed., *Key Engineering Materials* series, Trans Tech Publications.

Benveniste, Y., 1987, "A New Approach to the Application of the Mori-Tanaka's Theory in Composite Material," *Mech. Materials*, Vol. 6, pp. 147–157.

Dvorak, G. J., Laws, N., and Hejazi, M., 1985, "Analysis of Progressive Matrix Cracking in Composite Laminates I. Thermoelastic Properties of a Ply with Cracks," *J. Composite Mat.*, Vol. 19, pp. 216–234.

Gavazzi, A. C., and Lagoudas, D. C., 1990, "Incremental Elastoplastic Behavior of Metal Matrix Composites Based on Averaging Schemes," *Proceedings IUTAM Symposium on Inelastic Deformation of Composite Materials*, G. J. Dvorak, ed., Springer-Verlag, pp. 465–485.

Hill, R., 1965, "Theory of Mechanical Properties of Fibre-Strengthened Materials: III. Self-Consistent Model," *J. Mechanics and Physics of Solids*, Vol. 13, pp. 189–198.

Johnson, W. S., 1992, NASA Technical Memorandum 107597, Lewis Research Center.

Johnson, W. S., S. J. Lubowinski, and A. L. Highsmith, 1990, "Mechanical Characterization of Unnotched SCS-6/Ti-15-3 Metal Matrix Composites at Room Temperature," *Thermal and Mechanical Behavior of Metal Matrix and Ceramic Matrix Composites*, ASTM STP 1080, J. M. Kennedy et al., eds., ASTM, Philadelphia, PA, pp. 193–218.

Lagoudas, D. C., X. Ma, D. A. Miller, and D. H. Allen, 1995, "Modeling of Oxidation in Metal Matrix Composites," *Int. J. Engng. Sci.*, Vol. 33, No. 15, pp. 2327–2343.

Laws, N., and Dvorak, G. J., 1987, "The Effect of Fiber Breaks and Aligned Penny-Shaped Cracks on the Stiffness and Energy Release Rates in Uni-directional Composites," *Int. J. Solids and Structures*, Vol. 23, No. 9, pp. 1269–1283.

Lerch, B. A., Gabb, T. P., and MacKay, R. A., 1990a, "Heat Treatment Study of the SiC/Ti-15-3 Composite System," NASA TP 2970.

Lerch, B. A., and Saltsman, J. F., 1991, "Tensile Deformation Damage in SiC Reinforced Ti-15V-3Cr-3Al-3Sn," NASA Technical Memorandum 103620, Lewis Research Center.

Lissenden, Herakovich, C. T., and Pindera, M. J., 1995, "Response of SiC/Ti under Combined Loading part I: Theory and Experiment for Imperfect Bonding," *Journal of Composite Materials*, Vol. 29, No. 2, pp. 130–155.

Majumdar, B. S., and G. M. Newaz, 1992a, 1992b, 1993, NASA Contractor Report 189095, 189096, 191181, Lewis Research Center.

Mori, T., and K. Tanaka, 1973, "Average Stress in Matrix and Average Elastic Energy of Materials with Misfitting Inclusions," *Acta Metallurgica*, Vol. 21, pp. 571–574.

Newaz, G. M., B. S. Majumdar, and F. W. Brust, 1992, "Thermal Cycling Response of Quasi-Isotropic Metal Matrix Composites," ASME JOURNAL OF ENGINEERING MATERIALS AND TECHNOLOGY, Vol. 114, pp. 156–161.

Okada, M., and Banergee, D., 1984, "Tensile Properties of Ti-15V-3Al-3Cr-3Sn Alloy," *Titanium Science and Technology: Proceedings of the Fifth International Conference on Titanium*, Munich, Germany, Luetjering ed., Deutsch Gesellschaft fur Metallkunde, Pub., pp. 1835–1842.

Sun, C. T., J. L. Chen, G. T. Sha, and W. E. Koop, 1990, "Mechanical Characterization of SCS-6/Ti-6-4 Metal Matrix Composite," *J. Composite Mat.*, Vol. 24, pp. 1029–1059.

Weng, G. J., 1984, "Some Elastic Properties of Reinforced Solids, with Special Reference to Isotropic ones Containing Spherical Inclusions," *Int. J. Ingrg. Sci.*, Vol. 22, pp. 845–856.

Wolfenden, A., K. D. Hall, and B. A. Lerch, 1996, "The effect of heat treatment on Young's modulus, damping, and microhardness of SiC/Ti-15-3," *J. of Materials Science*, Vol. 31, pp. 1489–1493.